

UNIVERSITY OF OKLAHOMA

GRADUATE COLLEGE

BOLOMETRIC LUMINOSITIES OF PECULIAR TYPE II-P
SUPERNOVAE

A DISSERTATION

SUBMITTED TO THE GRADUATE FACULTY

in partial fulfillment of the requirements for the

Degree of

DOCTOR OF PHILOSOPHY

By

JEREMY A. LUSK
Norman, Oklahoma
2018

BOLOMETRIC LUMINOSITIES OF PECULIAR TYPE II-P
SUPERNOVAE

A DISSERTATION APPROVED FOR THE
HOMER L. DODGE DEPARTMENT OF PHYSICS AND
ASTRONOMY

BY

Dr. Edward Baron, Chair

Dr. Trina Hope

Dr. Chung Kao

Dr. Karen Leighly

Dr. John Wisniewski

To Lauren

Acknowledgements

To Lauren: I owe the greatest debt of gratitude to you. Your love, support, and encouragement know no bounds – from the 775 miles that separated us for three long, lonely years of graduate school to the handful of inches between us as I write these words from the passenger seat while you drive us to Norman to deposit this dissertation. Thank you for always believing in me.

To Teddy: watching you grow and learn and change over the last three years has been the most wondrous experience of my life. If this dissertation hadn't taken so long to complete, I would never have gotten to hear you cheer, "You can do it, Daddy!" I wouldn't have it any other way.

To Eddie: thank you for trusting me, for guiding me, and for always having my back. I will aspire to show my students the patience and dedication you have shown me through the years. I could not have asked for a better mentor and collaborator.

To Debra: thank you for getting me into this mess! You showed me how to be a scientist, and without your mentorship I wouldn't have gone to graduate school. You taught me that "beseechin' is fine, but showin' the hell up is better!" and that advice kept me going when times were tough.

To Terry: thank you for sharing your passion for physics. You always challenged me to do better, and you set me on a course to do what I do today.

To Mom, Dad, Jennifer, Ann, Rick, Joe, and Lisa: thank you for all the things – both great and small – that each one of you did to support me, Lauren, and Teddy over the years. Thank you for all the visits, the meals, the babysitting, the words of wisdom, the pep-talks, the care packages, the parenting advice, the stories, and the encouragement. Your love and support kept us connected to family when we might otherwise have felt adrift and alone.

To the friends I made along the way: thank you for making graduate school fun. I hope that I helped you as much as you helped me, because the board games, star parties, trivia nights, study sessions, long digressions, and celebrations sustained me over the years.

Contents

List of Tables	x
List of Figures	xv
Abstract	xvi
1 Bolometric Luminosity Calculation Techniques	1
1.1 Overview of Techniques	2
1.2 Conversion of observed magnitudes to monochromatic fluxes	4
1.3 Direct integration techniques	6
1.3.1 Quasi-bolometric flux (F_{qbol})	6
1.3.2 Augmenting F_{qbol} with unobserved flux (F_{aug})	7
1.4 Bolometric correction techniques	11
2 Sample of Peculiar Type II P Supernovae	16
2.1 SN 1998A	16
2.2 SN 2000cb	20
2.3 SN 2006V	21
2.4 SN 2006au	25
2.5 SN 2009E	29
3 SuperBoL: Supernova Bolometric Lightcurves	35
3.1 Introduction	35
3.2 Core Utilities	36
3.2.1 mag2flux module	37
3.2.2 photometry module	38
3.2.3 blackbody module	40
3.3 Implementation	41
3.3.1 Quasi-bolometric technique in SuperBoL	42
3.3.2 Augmented bolometric technique in SuperBoL	42
3.3.3 Bolometric correction in SuperBoL	44
3.3.4 Propagation of uncertainties in SuperBoL	45
3.4 Testing and Validation of SuperBoL	46
3.4.1 Unit Testing	46
3.4.2 Validation using blackbody models	47
3.4.3 Validation using white dwarf models	48
3.4.4 Reproducing SN 1987A lightcurve from Bersten and Hamuy (2009)	49
3.4.5 Reproducing SN 2000cb lightcurve from Hamuy (2001)	55
4 Bolometric Luminosities of Peculiar Type II P Supernovae	58
4.1 Supernova Parameters	58
4.2 Lightcurves	58
4.2.1 SN 1998A	60

4.2.2	SN 2000cb	62
4.2.3	SNe 2006V and 2006au	65
4.2.4	SN 2009E	72
4.3	Nickel Mass Estimates	75
4.4	Peak Luminosities	79
4.5	Nickel - Luminosity Relation	81
5	Comparison with PHOENIX models	85
5.1	Initial Proof-of-concept	86
5.2	Early phase synthetic spectra	89
5.2.1	SN 2000cb, JD 2451662.9	89
5.2.2	SN 2000cb, JD 2451663.9	93
5.2.3	SN 2000cb, JD 2451664.9	95
5.2.4	SN 2006au, JD 2453808.9	97
5.3	Plateau phase synthetic spectra	99
5.3.1	SN 2006au, JD 2453850.9	100
5.3.2	SN 2000cb, JD 2451722.8	102
5.4	Analysis of bolometric luminosity techniques	105
5.4.1	Early phase luminosities	105
5.4.2	Plateau phase luminosities	114
5.4.3	Enhanced Ca II emission in plateau-phase models of SN 2000cb .	118
5.5	Limited bandpasses and blackbody fits	121
5.5.1	SN 2000cb, JD 2451663.9	125
5.5.2	SN 2006au, JD 2453808.9	132
5.5.3	SN 2006au, JD 2453850.9	137
6	Summary	147
6.1	Future Work	153
6.2	Acknowledgments	156
	Bibliography	158
	Appendices	166
A	Hydrodynamic Models of Type II Supernovae	166
A.1	The Sedov-Taylor-von Neumann Blast Wave Solution	166
A.1.1	Governing Equations	169
A.1.2	Scale Invariants	170
A.1.3	Shock Conditions	171
A.1.4	Shock Radius and Velocity	173
A.1.5	Ordinary Differential Equations	174
A.1.6	Boundary Conditions	175
A.1.7	Energy Integral	176
A.1.8	Phase Plane Formalism	178
A.1.9	Singular Point	180
A.1.10	Singular Case Solution	182
A.1.11	Determining ξ_1	184
A.2	Broken Power-Law Ejecta	186
A.2.1	Propagation through the atmosphere	187

A.2.2	Rarefaction wave	188
A.2.3	Final ejecta structure	192

List of Tables

4.1	Adopted SN parameters from the literature	59
4.2	Bolometric Lightcurves of SN 1998A	62
4.3	Bolometric Lightcurves of SN 2000cb	63
4.3	Bolometric Lightcurves of SN 2000cb	64
4.3	Bolometric Lightcurves of SN 2000cb	65
4.4	Bolometric Lightcurves of SN 2006V	68
4.4	Bolometric Lightcurves of SN 2006V	69
4.5	Bolometric Lightcurves of SN 2006au	69
4.5	Bolometric Lightcurves of SN 2006au	71
4.5	Bolometric Lightcurves of SN 2006au	72
4.6	Bolometric Lightcurves of SN 2009E	74
4.6	Bolometric Lightcurves of SN 2009E	75
4.7	Ejected ^{56}Ni masses	78
4.8	Peak observed SN luminosities	81
5.1	Bolometric Luminosity with Sparse Photometry	87
5.2	Synthetic photometry of PHOENIX spectra similar to SN 2000cb 7 days post-explosion, assuming a distance of 30 Mpc	91
5.3	Comparison of SuperBoL bolometric luminosities from PHOENIX synthetic photometry, assuming a distance of 30.0 ± 0 Mpc and photometric uncertainties of 0.015 mag	92
5.4	Synthetic photometry of PHOENIX spectra similar to SN 2000cb 8 days post-explosion, assuming a distance of 30 Mpc	94
5.5	Comparison of SuperBoL bolometric luminosities from PHOENIX synthetic photometry, assuming a distance of 30.0 ± 0 Mpc and photometric uncertainties of 0.015 mag	94
5.6	Synthetic photometry of PHOENIX spectra similar to SN 2000cb 9 days post-explosion, assuming a distance of 30 Mpc	96
5.7	Comparison of SuperBoL bolometric luminosities from PHOENIX synthetic photometry, assuming a distance of 30.0 ± 0 Mpc and photometric uncertainties of 0.015 mag	96
5.8	Synthetic photometry of PHOENIX spectra similar to SN 2006au 15 days post-explosion, assuming a distance of 46 Mpc	99
5.9	Comparison of SuperBoL bolometric luminosities from PHOENIX synthetic photometry in Table 5.8, with photometric uncertainties of 0.015 mag	99
5.10	Synthetic photometry of PHOENIX spectra similar to SN 2006au 57 days post-explosion, assuming a distance of 46 Mpc	103

5.11	Comparison of SuperBoL bolometric luminosities from PHOENIX synthetic photometry in Table 5.10, with photometric uncertainties of 0.015 mag	103
5.12	Synthetic photometry of PHOENIX spectra similar to SN 2000cb 67 days post-explosion, assuming a distance of 30 Mpc	104
5.13	Comparison of SuperBoL bolometric luminosities from PHOENIX synthetic photometry, assuming a distance of 30.0 ± 0 Mpc and photometric uncertainties of 0.015 mag	106
5.14	Comparison of the luminosities derived from bolometric correction techniques using different color combinations, based on the synthetic magnitudes of two PHOENIX models similar to SN 2000cb 8 days post-explosion	109
5.15	Comparison of the luminosities derived from bolometric correction techniques using different color combinations, based on the synthetic magnitudes of two PHOENIX models similar to SN 2006au 57 days post-explosion. The $V - I$ colors fall outside the valid range of the polynomials published in Bersten and Hamuy (2009).	116
5.16	Comparison of SuperBoL bolometric luminosities from subsets of the PHOENIX synthetic photometry listed in Table 5.4.	127
5.16	Comparison of SuperBoL bolometric luminosities from subsets of the PHOENIX synthetic photometry listed in Table 5.4.	128
5.17	Comparison of SuperBoL bolometric luminosities from subsets of the PHOENIX synthetic photometry listed in Table 5.8, assuming a distance of 30.0 ± 0 Mpc and photometric uncertainties of 0.015 mag	133
5.18	Comparison of SuperBoL bolometric luminosities from subsets of the PHOENIX synthetic photometry listed in Table 5.10, assuming a distance of 30.0 ± 0 Mpc and photometric uncertainties of 0.015 mag	138
5.19	Comparison of SuperBoL bolometric luminosities from subsets of the PHOENIX synthetic photometry listed in Table 5.10, assuming a distance of 46.0 ± 0 Mpc and photometric uncertainties of 0.015 mag	143

List of Figures

2.1	Photometric lightcurves of SN 1998A, offset to match the peak magnitudes of the corresponding photometry of SN 1987A. The overall evolution of SN 1998A is very similar to that of SN 1987A. Photometry of SN 1998A from Pastorello et al. (2005), and photometry of SN 1987A from Hamuy and Suntzeff (1990) (solid lines.) . . .	18
2.2	Bolometric lightcurve of SN 1998A from Pastorello et al. (2005) calculated using the quasi-bolometric technique with BVRI photometry.	19
2.3	Photometric lightcurves of SN 2000cb, offset to match the peak magnitudes of the corresponding photometry of SN 1987A. Photometry of SN 2000cb from Hamuy (2001) and Kleiser et al. (2011), and photometry of SN 1987A from Hamuy and Suntzeff (1990) (solid lines.)	22
2.4	Bolometric lightcurve of SN 2000cb from Hamuy (2001) calculated using a bolometric correction technique with polynomial coefficients published in Hamuy (2001, Table 5.1).	23
2.5	Photometric lightcurves of SN 2006V, offset to match the peak magnitudes of the corresponding photometry of SN 1987A. Photometry of SN 2006V from Taddia et al. (2012), with stars designating photometric points transformed from the CSP natural system to the BVRI system. Photometry of SN 1987A from Hamuy and Suntzeff (1990) (solid lines.)	26
2.6	Bolometric lightcurve of SN 2006V from Taddia et al. (2012) calculated using an augmented bolometric technique.	27
2.7	Photometric lightcurves of SN 2006au, offset to match the peak magnitudes of the corresponding photometry of SN 1987A. Photometry of SN 2006au from Taddia et al. (2012), with stars designating photometric points transformed from the CSP natural system to the BVRI system. Photometry of SN 1987A from Hamuy and Suntzeff (1990) (solid lines.)	30
2.8	Bolometric lightcurve of SN 2006au from Taddia et al. (2012) calculated using an augmented bolometric technique.	31
2.9	Photometric lightcurves of SN 2009E, offset to match the peak magnitudes of the corresponding photometry of SN 1987A. Photometry of SN 2009E from Pastorello et al. (2012), and photometry of SN 1987A from Hamuy and Suntzeff (1990) (solid lines.) . . .	33
2.10	Bolometric lightcurve of SN 2009E from Pastorello et al. (2012) calculated using a quasi-bolometric technique augmented by assuming an identical color evolution to that of SN 1987A.	34

3.1	Ratio of SuperBoL -derived luminosity to blackbody model luminosity over a temperature range typical in the observed evolution of Type II-P supernovae.	49
3.2	Ratio of SuperBoL -derived temperatures and angular radii to those of the blackbody models underlying the synthetic photometry used to validate the code.	50
3.3	Ratio of SuperBoL -derived luminosity to white dwarf model luminosity over a temperature range typical in the observed evolution of Type II-P supernovae.	51
3.4	Bolometric lightcurves of SN 1987A. The previously published lightcurve is that of Bersten and Hamuy, 2009. The error-bars include the uncertainty in the distance to SN 1987A.	52
3.5	Direct integration lightcurve of SN 1987A. Note that on nights with only UBVRI photometry, the luminosity is systematically lower during the plateau phase.	54
3.6	Reproducing the bolometric lightcurve of SN 2000cb published by Hamuy (2001) using the bolometric correction technique from the same source. The distance error has been suppressed for clarity, and because both lightcurves assume the same distance.	57
4.1	Bolometric lightcurves of SN 1998A. The previously published lightcurve is that of Pastorello et al., 2005, described in section 2.1	61
4.2	Bolometric lightcurves of SN 2000cb. The previously published lightcurve is that of Hamuy, 2001, described in section 2.2	66
4.3	Bolometric lightcurves of SN 2006V. The previously published lightcurve is that of Taddia et al., 2012, described in section 2.3 .	70
4.4	Bolometric lightcurves of SN 2006au. The previously published lightcurve is that of Taddia et al., 2012, described in section 2.4 .	73
4.5	Bolometric lightcurves of SN 2009E. The previously published lightcurve is that of Pastorello et al., 2012, described in section 2.5	76
4.6	Comparison of ejected ^{56}Ni masses generated by SuperBoL and those previously published in the literature.	80
4.7	Relation between the ejected nickel mass and the bolometric luminosity of the supernova measured at $t_0 + 50\text{d}$. SN 2009E is excluded from this comparison, because no photometry is available around $t_0 + 50\text{d}$	82
4.8	Relation between the ejected nickel mass and the bolometric luminosity of the supernova measured at peak brightness. The data from Pejcha and Prieto (2015) are still measured at $t_0 + 50\text{d}$. . .	83
5.1	PHOENIX spectra similar to that of SN 2000cb 7 days post-explosion, normalized to match the observed spectrum at $\lambda = 5500\text{\AA}$	91
5.2	PHOENIX spectra similar to that of SN 2000cb 8 days post-explosion, normalized to match the observed spectrum at $\lambda = 5500\text{\AA}$	93

5.3	PHOENIX spectra similar to that of SN 2000cb 9 days post-explosion, normalized to match the observed spectrum at $\lambda = 5500\text{\AA}$	95
5.4	PHOENIX spectra similar to that of SN 2006au 15 days post-explosion, normalized to match the observed spectrum at $\lambda = 6000\text{\AA}$	97
5.5	PHOENIX spectra similar to that of SN 2006au 57 days post-explosion, normalized to match the observed spectrum at $\lambda = 6260\text{\AA}$	102
5.6	PHOENIX spectra similar to that of SN 2000cb 67 days post-explosion, normalized to match the observed spectrum at $\lambda = 6800\text{\AA}$	105
5.7	Comparison of SuperBoL -derived luminosities of PHOENIX model synthetic photometry with the luminosity of the PHOENIX model, for models similar to SN 2000cb 7 days post-explosion	107
5.8	Comparison of SuperBoL -derived luminosities of PHOENIX model synthetic photometry with the luminosity of the PHOENIX model, for models similar to SN 2000cb 8 days post-explosion.	108
5.9	Comparison between the spectrum of the $4.00 \times 10^{41} \text{ erg s}^{-1}$ PHOENIX model with the SuperBoL -SED derived from its synthetic photometry and the blackbody fit to the fluxes of the full SED. Since the <i>U</i> -band flux is lower than the blackbody fit, the linear UV correction is used.	108
5.10	Comparison between the spectrum of the $4.50 \times 10^{41} \text{ erg s}^{-1}$ PHOENIX model with the SuperBoL -SED derived from its synthetic photometry and the blackbody fit to the fluxes of the full SED. Since the <i>U</i> -band flux is lower than the blackbody fit, the linear UV correction is used.	110
5.11	Comparison of SuperBoL -derived luminosities of PHOENIX model synthetic photometry with the luminosity of the PHOENIX model, for models similar to SN 2000cb 9 days post-explosion	111
5.12	Comparison of SuperBoL -derived luminosities of PHOENIX model synthetic photometry with the luminosity of the PHOENIX model, for models similar to SN 2006au 15 days post-explosion	112
5.13	Comparison between the spectrum of the $5.00 \times 10^{41} \text{ erg s}^{-1}$ PHOENIX model with the SuperBoL -SED derived from its synthetic photometry and the blackbody fit to the fluxes of the full SED. Since the <i>U</i> -band flux is lower than the blackbody fit, the linear UV correction is used.	113
5.14	Comparison of SuperBoL -derived luminosities of PHOENIX model synthetic photometry with the luminosity of the PHOENIX model, for models similar to SN 2006au 57 days post-explosion	115
5.15	Comparison between the spectrum of the $14.0 \times 10^{41} \text{ erg s}^{-1}$ PHOENIX model with the SuperBoL -SED derived from its synthetic photometry and the blackbody fit to the fluxes of the full SED. Since the <i>U</i> -band flux is lower than the blackbody fit, the linear UV correction is used.	115

5.16	Comparison of SuperBoL -derived luminosities of PHOENIX model synthetic photometry with the luminosity of the PHOENIX model, for models similar to SN 2000cb 67 days post-explosion	119
5.17	Comparison between the spectrum of the 10.0×10^{41} erg s ⁻¹ PHOENIX model with the SuperBoL -SED derived from its synthetic photometry and the blackbody fit to the fluxes of the full SED. Since the <i>U</i> -band flux is lower than the blackbody fit, the linear UV correction is used.	120
5.18	Comparison between the observed spectrum of SN 2000cb, the SED computed from contemporaneous photometry, the PHOENIX model fit to the observed spectrum with a luminosity of 10.0×10^{41} erg s ⁻¹ , and the SuperBoL SED computed from synthetic photometry of the model spectrum. The slope of the observed SED from the <i>V</i> - to <i>I</i> -bands seems to indicate that the strong Ca II emission in the model was much weaker in the spectrum of SN 2000cb. . . .	122
5.19	Comparison of bolometric luminosities using different subsets of the available synthetic photometry, normalized to the true luminosities of the PHOENIX models similar to SN 2000cb 8 days post-explosion. Data from Table 5.16. Each subset of the synthetic photometry is displaced horizontally for clarity.	129
5.20	Comparison between the spectrum of the 4.00×10^{41} erg s ⁻¹ PHOENIX model with the SuperBoL -SED derived from <i>UBVRI</i> (top), <i>BVRI</i> (middle), and <i>BVI</i> (bottom) subsets of its synthetic photometry. Also shown are the blackbody fits to the fluxes of the full SED and to the <i>VRI</i> portion of the SED.	130
5.21	Comparison of bolometric luminosities using different subsets of the available synthetic photometry, normalized to the true luminosities of the PHOENIX models similar to SN 2006au 15 days post-explosion. Data from Table 5.17 Each subset of the synthetic photometry is displaced horizontally for clarity.	134
5.22	Comparison between the spectrum of the 5.00×10^{41} erg s ⁻¹ PHOENIX model with the SuperBoL -SED derived from <i>UBVRI</i> (top), <i>BVRI</i> (middle), and <i>BVI</i> (bottom) subsets of its synthetic photometry. Also shown are the blackbody fits to the fluxes of the full SED and to the <i>VRI</i> portion of the SED.	136
5.23	Comparison of bolometric luminosities using different subsets of the available synthetic photometry, normalized to the true luminosities of the PHOENIX models similar to SN 2006au 57 days post-explosion. Data from Table 5.18. Each subset of the synthetic photometry is displaced horizontally for clarity.	137
5.24	Comparison between the spectrum of the 14.00×10^{41} erg s ⁻¹ PHOENIX model with the SuperBoL -SED derived from <i>UBVRI</i> (top), <i>BVRI</i> (middle), and <i>BVI</i> (bottom) subsets of its synthetic photometry. Also shown are the blackbody fits to the fluxes of the full SED and to the <i>VRI</i> portion of the SED.	141

5.25	Comparison between the spectrum of the $14.00 \times 10^{41} \text{ erg s}^{-1}$ PHOENIX model with the SuperBoL-SED derived from <i>UBVRI</i> (top) and <i>BVRI</i> (bottom) subsets of its synthetic photometry. Also shown are the blackbody fits to the fluxes of the full SED and to the <i>RI</i> portion of the SED.	142
5.26	Comparison of bolometric luminosities using blackbody fits to the <i>VRI</i> and <i>RI</i> portions of the SED, for different subsets of the available synthetic photometry, normalized to the true luminosities of the PHOENIX models similar to SN 2006au 57 days post-explosion. Data from Table 5.18. Each subset of the synthetic photometry is displaced horizontally for clarity.	144
5.27	Comparison between the spectrum of the $15.00 \times 10^{41} \text{ erg}^{-1}$ PHOENIX model with the SuperBoL-SED derived from <i>UBVRI</i> (top) and <i>BVRI</i> (bottom) subsets of its synthetic photometry. Also shown are the blackbody fits to the fluxes of the <i>VRI</i> and the <i>RI</i> portion of the SED.	146
6.1	Flow chart demonstrating the application of different bolometric luminosity calculation techniques. Which technique most closely re-produces the true bolometric luminosity of a PHOENIX model depends on the available bands, as shown by the results in chapter 5.154	

Abstract

In this work, I analyze the bolometric luminosities of several peculiar Type II-P supernovae which are thought to originate from the same class of blue supergiant progenitor stars as the famous SN 1987A. This analysis is performed with the new open-source code **SuperBoL** (Supernova Bolometric Lightcurves.) I wrote **SuperBoL** to implement several different bolometric luminosity calculation techniques commonly used in the literature. I then use **SuperBoL** to estimate the bolometric luminosities of the five peculiar Type II-P supernovae in this study: SN 1998A, SN 2000cb, SN 2006V, SN 2006au, and SN 2009E, using photometry, extinction, and distance values from the literature. The results show that the quasi-bolometric technique typically produces bolometric luminosities about half as bright as the other techniques, dependent in large part on the wavelength range of the available photometric bands. The augmented bolometric technique produces luminosities which are systematically higher than those from the bolometric correction technique for all but SN 2000cb, where they largely agree. One parameter of the supernova which can be measured directly from the bolometric lightcurve is the mass of ejected ^{56}Ni , the radioactive decay of which powers the lightcurve after the plateau-phase. These masses vary by a factor of about 3, depending on which lightcurve is used to obtain them. In order to understand why the different bolometric luminosity calculation techniques produce such different values, I use

the advanced general-purpose radiative transfer code **PHOENIX** to produce a grid of 26 synthetic supernova spectra of different known luminosities, constructed to closely match observed spectra of both SN 2000cb and SN 2006au. Taking the synthetic photometry of these **PHOENIX** models and running them through **SuperBoL** produces 156 different comparisons between known and calculated bolometric luminosities. These results show that in most cases, the quasi-bolometric technique under-estimates the bolometric luminosity of the models by about 50%. With IR photometry in the J and H bands, this can be improved to an under-estimation of only 10% - 15%. The augmented bolometric method performs much better, in some circumstances re-producing the bolometric luminosity of the model within 1%. I find that the accuracy of the augmented bolometric technique depends sensitively on the wavelength range of the available photometry and the photometric bands used when fitting a blackbody curve to the spectral energy distribution derived from the photometry. The best results are obtained when the fit is restricted to fluxes at wavelengths longer than the peak of the SED, only. The bolometric correction method implemented in **SuperBoL** performs quite well across the range of **PHOENIX** models, producing bolometric luminosities which typically fall within 3% – 7% of the model luminosity. However, because the bolometric correction technique depends only on the photometric colors of the supernovae, it will produce erroneous results if those colors stray outside the range typical of the template supernovae used to construct the polynomial relations between the colors and bolometric corrections.

Chapter 1

Bolometric Luminosity Calculation Techniques

The bolometric luminosity of a supernova is the total radiant luminosity, typically measured in erg s^{-1} . The variation of this luminosity with time after explosion is the lightcurve, and is an important characteristic in the study of transient objects such as supernovae. Supernovae are, to first order, classified by their spectra, further classification involves the shapes of their lightcurves (Filippenko, 1997). The shapes of lightcurves also reveal important information about a supernova. Hydrodynamic models of expanding supernova ejecta output bolometric lightcurves which can be compared with those of observed supernovae (for a recent example, see Piro and Morozova, 2014; Morozova et al., 2015). From these comparisons, the model is used to estimate the mass and structure of the progenitor, the total energy of the explosion, and the amount of radioactive ^{56}Ni synthesized in the supernova.

Determining the properties of a supernova progenitor by matching its observed bolometric lightcurve to one calculated by a hydrodynamic model is predicated on the ability to accurately determine the bolometric lightcurve of a supernova. For well-observed supernovae with robust distance determinations like SN 1987A, the bolometric luminosity can be determined by integrating the copious photometry directly (see Suntzeff and Bouchet, 1990, and references therein). For less well-

observed supernovae, corrections must be made to the available photometry to account for unobserved radiation from the object. We seek to analyze these different methods by using a set of supernovae thought to originate from blue supergiant (BSG) progenitors, like the aforementioned SN 1987A. All of the supernovae have bolometric luminosities published previously in the literature. We will produce bolometric light curves for each of these supernovae using a variety of techniques from the literature, and characterize any variability that might arise from the use of these different methods.

1.1 Overview of Techniques

The techniques for calculating a bolometric lightcurve from observed photometric magnitudes can be classified into two broad categories: direct integration and bolometric correction.

Direct integration uses only the observed photometry, converting broad-band filter magnitudes to monochromatic fluxes at wavelengths representative of the filters. These fluxes are then integrated, typically using the trapezoidal method, to generate a value often referred to as the *quasi-bolometric flux*. This quasi-bolometric flux represents only the observed portion of the total spectral energy distribution of the supernova, and does not include flux which falls blueward or redward of the observable range of the telescope. Examples of quasi-bolometric luminosity calculation techniques from the literature are given in subsection 1.3.1. The quasi-bolometric flux is typically augmented by UV and IR corrections — estimates of the missing flux blueward and redward of the observed flux. Usually,

these corrections are made by fitting a blackbody to the observed flux, and integrating that blackbody function from the reddest observed wavelength to infinity, and from the bluest observed wavelength to zero. Because the SED of supernovae are known to depart significantly from that of a blackbody due to line blanketing in the UV, there are a variety of ways that UV corrections have been handled in the literature, the most prevalent of which are detailed in subsection 1.3.2

Bolometric correction methods use the bolometric lightcurves of well-observed supernovae (usually calculated using the direct integration technique as mentioned above) to find correlations between an observable quantity such as color and the bolometric correction $BC = m_{bol} - (V - A_V)$. With this, magnitudes in a filter band can be converted to bolometric magnitudes, and then into bolometric luminosities. By finding polynomials which describe the relationship between color and bolometric correction, the bolometric luminosity of a less well-observed supernova can be calculated simply by making color observations and a distance estimate. This assumes, of course, that the same relationship found between the color and bolometric correction of the template supernova exists for the less well-observed supernova. It is therefore important to use several different well-observed supernovae to establish the polynomials used to transform color into a bolometric correction. section 1.4 gives an overview of the bolometric correction technique, and provides references to several different implementations of the technique, using different samples of well-observed template supernovae or atmospheric models.

1.2 Conversion of observed magnitudes to monochromatic fluxes

The calculation of a bolometric luminosity from observational photometric data begins with the conversion from magnitude to monochromatic flux. The standard relationship between magnitudes and fluxes for two observed objects is

$$m_1 - m_2 = -2.5 \log_{10} \left(\frac{f_1}{f_2} \right). \quad (1.1)$$

Many photometric systems are characterized by the “flux at zero magnitude” in each passband — the monochromatic flux at the effective wavelength of the filter that corresponds to a magnitude of zero. Values of the flux corresponding to zero magnitude for the UBVRIJHKL Cousins-Glass-Johnson system are reported in Bessell et al. (1998) (their Table A2). In the case that the flux at zero magnitude is available from the literature, the equation to transform from apparent magnitude to flux incident at the top of Earth’s atmosphere is straightforward:

$$f(\lambda_{\text{eff}}) = f_0(\lambda_{\text{eff}}) 10^{-0.4(m-0)} \quad (1.2)$$

Some photometric systems, such as the natural system developed for the Carnegie Supernova Project (CSP) (see Stritzinger et al., 2011, and references within) report zero-points in addition to or instead of $f_0(\lambda_{\text{eff}})$. The zero-point of filter X is defined in relation to the observed magnitude of a standard star m_{std}

through filter X and the mean flux of the star across the filter bandpass \bar{f}_X . The mean flux of the star across the filter bandpass is defined as

$$\bar{f}_X = \frac{\int_{\lambda_a}^{\lambda_b} f_{\text{std}}(\lambda) S_X(\lambda) d\lambda}{\int_{\lambda_a}^{\lambda_b} S_X(\lambda) d\lambda}, \quad (1.3)$$

where $f_{\text{std}}(\lambda)$ is the spectral energy distribution (SED) of the standard star (incident at the top of Earth's atmosphere) in units of $\text{erg s}^{-1} \text{ cm}^{-2} \text{ \AA}^{-1}$, $S_X(\lambda)$ is the response function of the bandpass X , λ_a and λ_b are the bounds of the filter response function. The zero point is defined by

$$m_{\text{std}} = -2.5 \log_{10}(\bar{f}_X) + \text{ZP}_X. \quad (1.4)$$

Using this zero point, the equation to transform from apparent magnitude to mean flux incident at the top of Earth's atmosphere is

$$\bar{f}_X = 10^{-0.4(m - \text{ZP}_X)}. \quad (1.5)$$

Complications to this procedure arise when examining photometry from different photometric systems. CCD detectors integrate photon counts rather than energy fluxes. As a result, the zeropoints reported for some photometric systems assume fluxes and bandpasses in photon units, rather than units of energy (for details, see Bessell et al. (1998), Appendix E and Hamuy et al. (2001), Appendix B). It should also be noted that the zeropoints of photometric systems such as the CSP natural system are calculated using the integrated flux within the bandpass

(F_X , in photons $\text{cm}^{-2} \text{s}^{-1}$) rather than the mean flux over the bandpass (\bar{f}_X , in photons $\text{cm}^{-2} \text{s}^{-1} \text{\AA}^{-1}$). The two are related by

$$\bar{f}_X = \frac{F_X}{\int_{\lambda_a}^{\lambda_b} S_X(\lambda) d\lambda}. \quad (1.6)$$

For standard photometric systems, transmission functions are available in on-line databases such as the Asiago Database on Photometric Systems (ADPS¹) (Moro and Munari, 2000; Fiorucci and Munari, 2003).

1.3 Direct integration techniques

The fluxes obtained by converting the observed broad-band photometry can be used to directly estimate the bolometric luminosity of a supernova. This is accomplished by integrating between the observed monochromatic fluxes. Corrections to this integrated flux can be made for un-observed flux that falls outside the wavelength range covered by the filters used in the photometric observations.

1.3.1 Quasi-bolometric flux (F_{qbol})

In order to integrate the fluxes over wavelength, each flux must be assigned to a particular wavelength within the bandpass of the filter used to obtain the magnitude measurement. Many authors use the effective wavelength λ_{eff} of the filter band as the wavelength of the monochromatic flux λ_X for filter X (see, for example, Hamuy et al., 1988; Stritzinger et al., 2002; Pastorello et al., 2005;

¹<http://ulisse.pd.astro.it/Astro/ADPS/>

Folatelli et al., 2006; Bersten and Hamuy, 2009).

With the fluxes assigned to wavelengths, different integration techniques can be used to determine a “quasi-bolometric” flux F_{qbol} . Many authors use trapezoidal integration, which integrates the observed fluxes in each filter band X , using linear interpolation between the observations (see, for example, Hamuy et al., 1988; Clocchiatti et al., 1996; Elmhamdi et al., 2003)

$$F_{\text{qbol}} = \frac{1}{2} \sum_{X=1}^N (\lambda_{X+1} - \lambda_X) (\bar{f}_{X+1} + \bar{f}_X) \quad (1.7)$$

From this quasi-bolometric flux, the quasi-bolometric luminosity is determined using the usual relation

$$L_{\text{qbol}} = 4\pi D^2 F_{\text{qbol}} \quad (1.8)$$

where D is the distance to the supernova.

Taddia et al. (2012) use a different scheme to determine the quasi-bolometric flux. First, a cubic spline curve is fit to the observed epochs, and that curve is then integrated from the shortest to longest value of λ_X .

1.3.2 Augmenting F_{qbol} with unobserved flux (F_{aug})

Because the bolometric luminosity of a supernova includes luminosity at wavelengths which fall outside the range of ground-based broad-band photometry, estimates must be made of the missing flux blueward of the shortest wavelength filter and redward of the longest wavelength filter used on a particular observation.

There are different methods used throughout the literature to estimate this

missing flux. Hamuy et al. (1988) estimate the missing flux from SN 1987A in the IR by assuming that the flux from the M band to infinity is equal to the flux observed between the L and M bands, an assumption based on the behavior of a blackbody of temperature 5000 K. Because the observations of SN 1987A extend so far into the IR, the missing flux in the IR using this estimation is below 1% of the total flux at all observed epochs.

Unlike SN 1987A, most supernovae lack extensive, frequent IR observations over the course of their photometric evolution. For these supernovae, a different approach must be used. Patat et al. (2001) assume a constant IR correction of 35% in their analysis of SN 1998bw, the value being taken from the IR contribution of the last available set of JHK observations. Elmhamdi et al. (2003) similarly use a constant correction of 0.19 dex to scale up the radioactive tail of SN 1999em, provided by integrating the latest observed J, H, and K fluxes. Schmidt et al. (1993) used the ratio $L_{\text{VRI}}/L_{\text{bol}}$ of SN 1987A to correct the VRI-derived luminosity of SN 1990E, assuming

$$L(\text{SN}) = L_{\text{qbol}}(\text{SN}) \times \frac{L_{\text{bol}}(1987\text{A})}{L_{\text{qbol}}(1987\text{A})}. \quad (1.9)$$

This approximate bolometric correction factor is valid only if both objects undergo identical evolution in color (Pastorello et al., 2012). This assumption is reasonable enough to provide an estimate of the bolometric luminosity, and was also used by Clocchiatti et al. (1996) in the study of SN 1992H and more recently by Pastorello et al. (2012) in the study of SN 2009E.

Most recent papers correct for missing flux in the IR by fitting a blackbody SED to the reddest observed fluxes (typically near-IR filters,) and integrating the blackbody flux redward of the longest effective wavelength to $\lambda = \infty$ (Folatelli et al., 2006; Bersten and Hamuy, 2009; Lyman et al., 2014).

The techniques used to correct for missing flux in the UV depend on the age of the supernova and the details of the SED. The primary cause of this diversity stems from the fact that in the UV, supernovae depart rapidly from the idealized blackbody SED as they expand and cool. The departure is most pronounced during the plateau and radioactive decline phases of a Type II supernova lightcurve, and is due to the formation of a dense forest of absorption lines in the UV from iron-peak elements in the ejecta (see, for example, Baron et al., 1996)

Early in the visible evolution of a supernova, the effective temperature is on the order of $T_{\text{eff}} \sim 1 \times 10^4$ K and lacks strong features, closely approximating the spectrum of a high-temperature blackbody (Filippenko, 1997). The peak of the emission is then ~ 2900 Å, inaccessible to ground-based telescopes as the theoretical UV cutoff for most observatories lies at $\lambda = 3000$ Å (see, for example, Nitschelm, 1988). The primary source of UV absorption around $\lambda = 3000$ Å is gaseous ozone (O_3) in Earth’s stratosphere. At early times, therefore, the UV correction factor will be significant.

Bersten and Hamuy (2009) found that for a sample of three well-observed supernovae (which included SN 1987A) the missing flux in the UV at early times was as high as 50% of the total observed flux. Using supernova atmosphere models, they found even higher UV corrections of up to 80% when $B - V \lesssim 0.2$.

Space-based UV photometry of supernovae is available from orbital instruments such as the *Swift* UV-Optical Telescope (UVOT) (see Roming et al., 2005). Because *Swift* UVOT observations reach farther into the UV than ground-based observations, the need to correct for unobserved UV light will decrease. In a study of *Swift* photometry of 50 core-collapse supernovae, Pritchard et al. (2014) find that UV corrections drop to $\sim 10\% - 30\%$ at early times.

The methods used to calculate the UV correction fall largely into two categories: black-body extrapolation and linear extrapolation. As mentioned above, at early times the spectrum of a supernova is largely similar to that of a high-temperature blackbody. To correct for the large amount of flux emitted in the UV at these times, many past studies have fit a blackbody curve to the monochromatic fluxes derived from broad-band photometry, and integrated under the blackbody curve from $\lambda = 0$ to a wavelength near the shortest observed filter. Bersten and Hamuy (2009) use the effective wavelength of the U filter as the end-point of the integration, while Lyman et al. (2014) use the blue edge of the of the U band.

As the supernova cools and expands, atmosphere models diverge from a simple Planck function in the UV. Dense forests of absorption lines from iron-peak elements cause short-wavelength U and B filter observations to drop below the magnitudes expected from a blackbody curve of the same effective temperature. To correct for unobserved UV flux in these epochs, it is common to augment the observed fluxes with a linear extrapolation from a characteristic wavelength where the flux is assumed to drop to zero ($\lambda = 2000 \text{ \AA}$ in Bersten and Hamuy (2009) and Lyman et al. (2014), and $\lambda = 3000 \text{ \AA}$ in Folatelli et al. (2006)) to the effective

wavelength of the shortest observed filter.

1.4 Bolometric correction techniques

The techniques used to calculate the bolometric luminosity in section 1.3 work best for supernovae observed over their entire evolution with frequent observations in multiple bandpasses covering the widest possible wavelength range. Due to the realities of observing transient objects, there are very few supernovae which match those criteria. We therefore expect that supernovae with less frequent observations using limited filtersets will have larger uncertainties in the bolometric luminosities derived using direct integration techniques.

However, it is possible to leverage the plentiful observations of supernovae like SN 1999em and SN 1987A to help determine the bolometric luminosity of a less well-observed supernova. This can be accomplished by first determining the bolometric luminosities of the well-observed “template” supernovae and then computing bolometric correction factors, typically the difference between the apparent bolometric magnitude and the apparent V-band magnitude:

$$BC = m_{\text{bol}} - (V - A_{V, \text{ total}}), \quad (1.10)$$

where

$$A_{V, \text{ total}} = A_{V, \text{ gal}} + A_{V, \text{ host}}. \quad (1.11)$$

As shown by Hamuy (2001), the values of the bolometric correction for template supernovae SN 1999em and SN 1987A correlate strongly with the intrinsic BVI

colors of the supernovae (Figure 5.3 in Hamuy, 2001). The correlation can be quantified by a polynomial fit of the form

$$BC(\text{color}) = \sum_{i=0}^n c_i(\text{color})^i \quad (1.12)$$

where n , the order of the fit, varies with the chosen color. Later work by Bersten and Hamuy (2009) refined the polynomial fits by adding data from the well-observed template supernova SN 2003hn (coefficients c_i given in their Table 1.) Additional work by Lyman et al. (2014) using a sample of 21 well-observed template supernovae from the literature produced a third set of second-order polynomial coefficients and expanded the range of valid color combinations to include those from the set *BgVriI* (their Tables 1, 2, and 3.)

Pejcha and Prieto (2015) developed a theoretical model of supernova lightcurve evolution and performed a large-scale least-squares fit using data from 26 supernovae. With their results, they calculate bolometric corrections using a broader range of filters than previous studies, and produce a fourth set of fifth-order polynomial coefficients (their Table 8.)

With the polynomial coefficients c_i from one of the above datasets, it is possible to calculate the bolometric correction to convert the photometry of a less well-observed supernova to a bolometric magnitude using only two-filter colors of the supernova. The key assumption in this technique is that the correlation between observed color and bolometric correction derived from the template supernovae also applies to less well-observed supernovae. As mentioned in section 1.1, super-

novae with unusual color evolution, or which belong to a sub-type not included in the sample of template supernovae used to calculate the polynomial coefficients of a given technique, may not be well-suited for analysis using that technique. Because SN 1987A is used as a template in the two bolometric correction techniques that are implemented later in this work, the sample of SN 1987A-like supernovae presented in chapter 2 should be excellent candidates for analysis. Direct integration techniques like those described in section 1.3, which do not rely on prior assumptions about the color evolution of template supernovae, might be better suited to calculating the bolometric luminosities of other sub-types of supernovae.

Once the technique has been applied to the observed photometry of a supernova to produce bolometric corrections, the resulting bolometric magnitudes can be converted into bolometric luminosities after choosing an appropriate bolometric magnitude zeropoint.

The choice of zeropoint differs from one technique to the next. Hamuy (2001) uses a zeropoint of -8.14 , chosen so that the bolometric magnitude of Vega would be zero. Later, Bersten and Hamuy (2009) used a zeropoint of -11.64^2 , again in order to make the bolometric magnitude of Vega equal zero. This large difference in zeropoint stems from the method used to define the bolometric magnitude in the two techniques.

In defining the bolometric magnitude of a well-observed template supernova, Hamuy (2001) fits a blackbody function to the reddening-corrected $BVIJHK$

²ZP = -11.64 in Bersten and Hamuy (2009), but appears with the wrong sign in their Equation 4.

magnitudes. This blackbody fit is parameterized by a temperature T and angular radius $\theta = R/D$, and the bolometric flux of the blackbody is (by the Stefan-Boltzmann law) $F_{\text{bol}} = \sigma\theta^2 T^4$. The bolometric luminosity of this blackbody fit is then defined by

$$m_{\text{bol}} = -2.5 \log_{10}(4\pi F_{\text{bol}}) - 8.14, \quad (1.13)$$

while Bersten and Hamuy (2009) use

$$m_{\text{bol}} = -2.5 \log_{10}(F_{\text{bol}}) - 11.64. \quad (1.14)$$

The presence of 4π in the argument to the logarithm in Equation 1.13 means that the zeropoints are not given in the same bolometric magnitude system. Extracting the factor of 4π from the logarithm and combining it with the zeropoint in Equation 1.13 gives an “effective zeropoint” of $\text{ZP}_{\text{eff}} \approx -10.89$, in much better agreement with the zeropoint of Bersten and Hamuy (2009).

Once the bolometric correction has been found using the coefficients and polynomial relation in Equation 1.12, it can be combined with the observed V -band magnitude, total V -band extinction $A_{V, \text{total}}$, bolometric magnitude zeropoint ZP , and distance to the supernova D to give the bolometric luminosity (Equation 1.15.)

$$\log_{10}(L_{\text{bol}}) = -0.4[BC(\text{color}) + V - A_{V, \text{total}} - \text{ZP}] + \log_{10}(4\pi D^2) \quad (1.15)$$

In Lyman et al. (2014), the bolometric magnitude scale is anchored using the solar values of absolute bolometric magnitude and bolometric luminosity:

$$M_{\text{bol}} = M_{\odot, \text{bol}} - 2.5 \log_{10} \left(\frac{L_{\text{bol}}}{L_{\odot, \text{bol}}} \right). \quad (1.16)$$

Pejcha and Prieto (2015) adopt a zeropoint based on the luminosity corresponding to zero absolute magnitude of $L_{\text{bol}, 0} = 3.055 \times 10^{35} \text{ erg s}^{-1}$. This was chosen based on the extant recommendation of the International Astronomical Union (Anderson, 1999). However, this value was not officially adopted by the IAU General Assembly, and only used sporadically in the literature. In 2015, IAU 2015 Resolution B2 adopted a slightly different bolometric magnitude zeropoint corresponding to $L_{\text{bol}, 0} = 3.0128 \times 10^{35} \text{ erg s}^{-1}$ (Mamajek et al., 2015).

With the ability to calculate a quasi-bolometric luminosity L_{qbol} , a multitude of techniques for correcting that luminosity for unobserved UV and IR light to calculate the direct integration luminosity L_{D} and multiple sets of coefficients for determining the luminosity from bolometric corrections L_{BC} , we now turn our attention to the sample of SN 1987A-like supernovae sometimes referred to as “peculiar” Type II-P.

Chapter 2

Sample of Peculiar Type II P Supernovae

The supernovae used in this sample were selected by their common origin with SN 1987A — all are thought to originate from compact blue supergiant progenitors. Our sample includes SN 1998A, SN 2000cb, SN 2006V, SN 2006au, and SN 2009E. These are the best observed of this class of supernovae (except, of course, for SN 1987A.) In the sections to follow, we will use the techniques discussed above to determine the bolometric lightcurves of these supernovae, and compare them with those previously published in the literature.

2.1 SN 1998A

SN 1998A was discovered on 1998 January 6.77 UT by Williams et al. (1998) as part of the automated supernova search by the Perth Astronomy Research group. Follow-up observations determined the location to be $\alpha = 11^{\text{h}}09^{\text{m}}50^{\text{s}}.33$, $\delta = -23^{\circ}43'43''.1$ (J2000). Preliminary photometric data from the Perth Astronomy Research Group was published by Woodings et al. (1998). A more detailed analysis of the object was published by Pastorello et al. (2005), including spectroscopy, atmospheric models, and a pseudo-bolometric light curve.

The distance, extinction, and explosion date for SN 1998A are taken from Pastorello et al. (2005) and are compiled in Table 4.1. The distance modulus of

$\mu = 32.41$ to the supernova was taken from the recession velocity of the host galaxy IC 2627 found in LEDA¹ (Makarov et al., 2014), assuming $H_0 = 65 \text{ km s}^{-1} \text{ Mpc}^{-1}$. This corresponds to a distance of $D_{98A} = 30 \pm 7 \text{ Mpc}$. Foreground extinction of $A_{B, \text{gal}} = 0.52$ from Schlegel et al. (1998) is the only significant source of extinction along the line-of-sight to the supernova. No host galaxy extinction is assumed, evidenced by the lack of narrow Na I D absorption in the spectrum of the supernova (Leonard and Filippenko, 2001). The explosion date is taken to be $\text{JD } 245080 \pm 4$ from Woodings et al. (1998) from shifting the shape of the light curve to match that of SN 1987A.

Figure 2.1 shows the photometry of SN 1998A, with magnitudes in each band offset to most closely match those of SN 1987A. The photometric data shown is from Pastorello et al. (2005) and the light curves of SN 1987A are from the first 813 days of $\text{UBV(RI)}_{\text{KC}}$ photoelectric observations obtained using the 0.41 and 1.0 m telescopes at Cerro Tololo Inter-American Observatory, first published in Hamuy and Suntzeff (1990). The overall photometric evolution of SN 1998A is very similar to that of SN 1987A, as noted by Pastorello et al. (2005).

The bolometric lightcurve presented in Pastorello et al. (2005) is a pseudo-bolometric lightcurve using BVRI photometry. No corrections were made for unobserved flux in the UV or IR. Figure 2.2 shows the bolometric lightcurve of SN 1998A, as calculated by Pastorello et al. (2005). The bolometric luminosity is calculated using the values for foreground extinction, distance, and explosion date reported above.

¹<http://leda.univ-lyon1.fr>

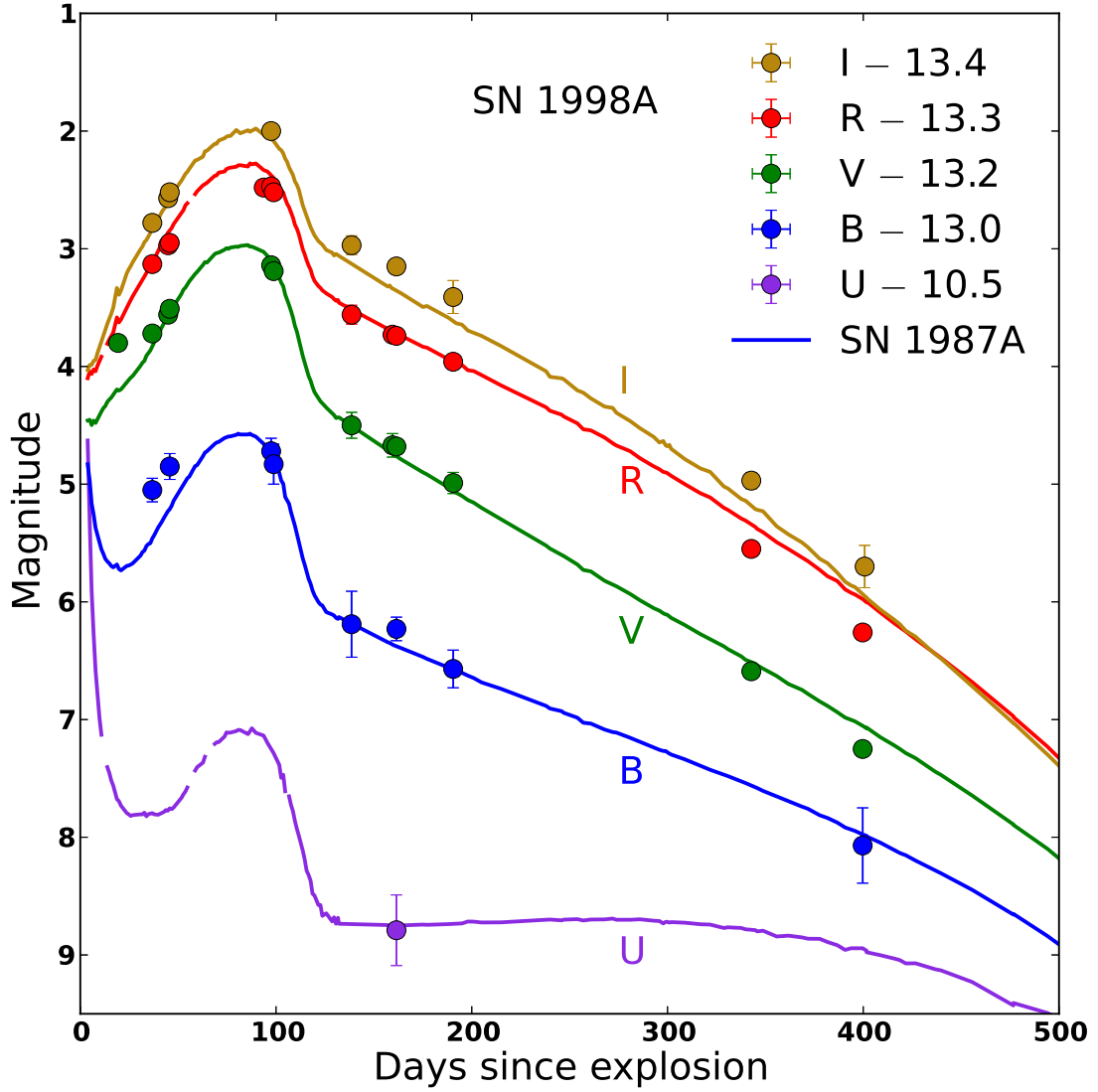


Figure 2.1 Photometric lightcurves of SN 1998A, offset to match the peak magnitudes of the corresponding photometry of SN 1987A. The overall evolution of SN 1998A is very similar to that of SN 1987A. Photometry of SN 1998A from Pastorello et al. (2005), and photometry of SN 1987A from Hamuy and Suntzeff (1990) (solid lines.)

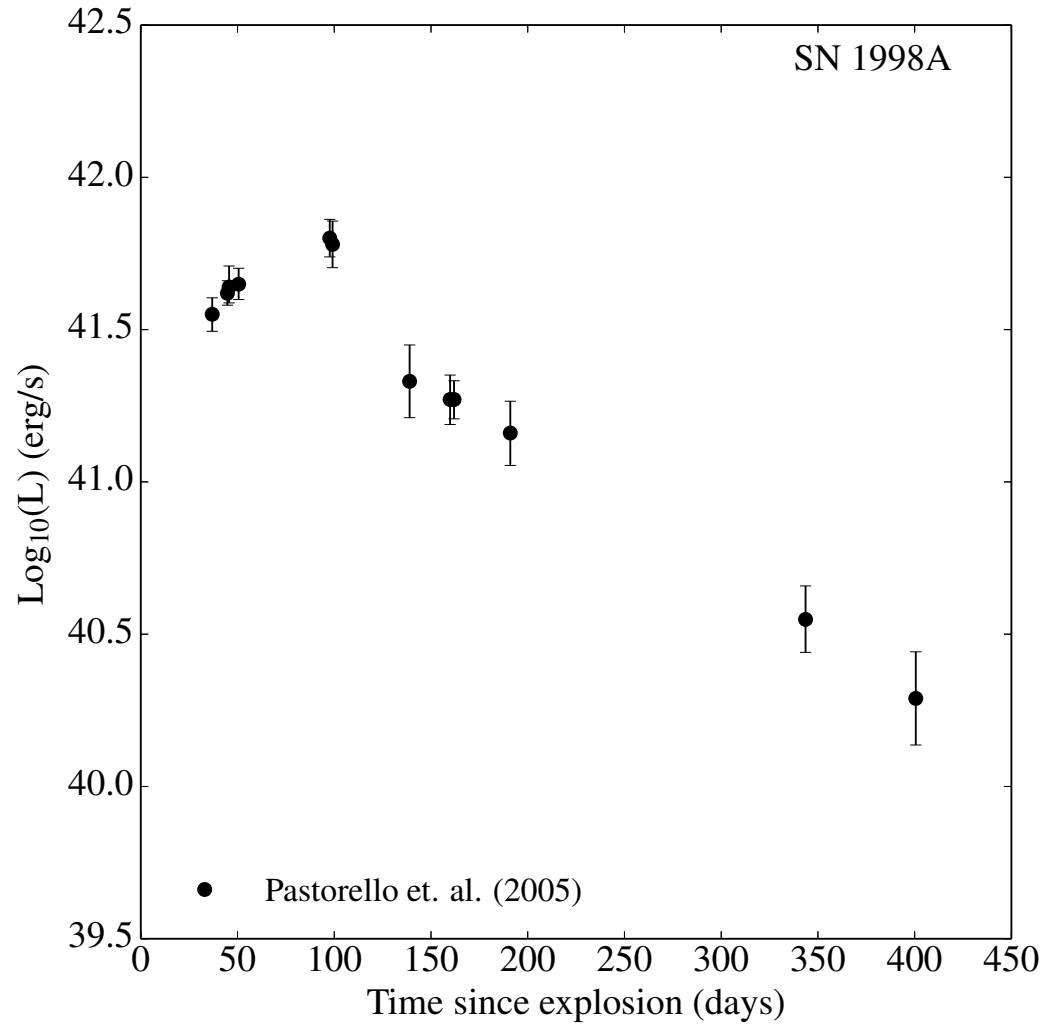


Figure 2.2 Bolometric lightcurve of SN 1998A from Pastorello et al. (2005) calculated using the quasi-bolometric technique with BVRI photometry.

2.2 SN 2000cb

SN 2000cb was discovered on 2000 April 27.4 UT by Papenkova and Li (2000) as part of the Lick Observatory Supernova Search. The supernova was located at $\alpha = 16^{\text{h}}01^{\text{m}}32^{\text{s}}.15$, $\delta = +1^{\circ}42'23''.0$ (J2000) in the spiral galaxy IC 1158. Photometry of the object has been published by Hamuy (2001) and Kleiser et al. (2011).

The supernova parameters given by Kleiser et al. (2011), are shown in Table 4.1. The distance $D_{00cb} = 30 \pm 7$ Mpc is taken from the SFI++ dataset of Tully-Fisher distances published by Springob et al. (2009). This distance is slightly lower than the range of $\sim 31 - 37$ Mpc given by the various expanding photosphere method analyses in Hamuy (2001). The host galaxy reddening of the supernova is minimal — as in the case of SN 1998A the supernova spectrum shows no evidence of narrow Na I D absorption. We adopt the Galactic extinction used in Kleiser et al. (2011) of $E(B - V)_{\text{gal}} = 0.114$ mag from Schlegel et al. (1998) with the Cardelli et al. (1989) slope of $R_V = 3.1$ to give $A_{V, \text{gal}} = 0.373$. The explosion date of $\text{JD } 2451656 \pm 4$ is calculated by Kleiser et al. (2011) using a cubic spline extrapolation of their first five unfiltered observations of SN 2000cb. Hamuy (2001) arrives at a similar value of $t_0 = 2451653.8$ using an average of six expanding photosphere method solutions.

The combined photometric data from Hamuy (2001) and Kleiser et al. (2011) are compared to the lightcurves of SN 1987A in Figure 2.3, with magnitudes in each band offset to most closely match those of SN 1987A. While the I and

R-band photometry share a similar evolution to the corresponding bands of SN 1987A photometry, the *V*- and *B*-bands indicate that at early times, the two shorter-wavelength bands evolve to peak brightness much more rapidly than those of SN 1987A, and from 30 days after explosion more closely resemble the slowly-evolving plateau shapes associated with more typical Type II P SNe such as SN 1999em (Kleiser et al., 2011).

Published bolometric lightcurves of SN 2000cb appear in both Hamuy (2001) and Kleiser et al. (2011). The lightcurve published by Hamuy (2001) is found using a bolometric correction technique very similar to the more recent one published by Bersten and Hamuy (2009). The lightcurve published by Kleiser et al. (2011) is calculated by fitting a blackbody spectrum to the observed optical photometry of SN 2000cb, leaving the luminosity, radius, and temperature as free parameters.

Figure 2.4 shows the bolometric lightcurve of SN 2000cb, as calculated by Hamuy (2001). The polynomial coefficients necessary to transform from the $B - V$ and $V - I$ colors into bolometric correction factors are given in Hamuy (2001, Table 5.1).

2.3 SN 2006V

SN 2006V was discovered by Chen et al. (2006) on 2006 February 4.67 UT as part of the Taiwan Supernova Survey. The supernova was located at $\alpha = 11^{\text{h}}31^{\text{m}}30^{\text{s}}.01$, $\delta = -2^{\circ}17'52''.2$ (J2000) in the spiral galaxy UGC 6510. Photometry of the object was published by Taddia et al. (2012) as part of the Carnegie Supernova Project.

We adopt basic supernova parameters first published in the analysis of

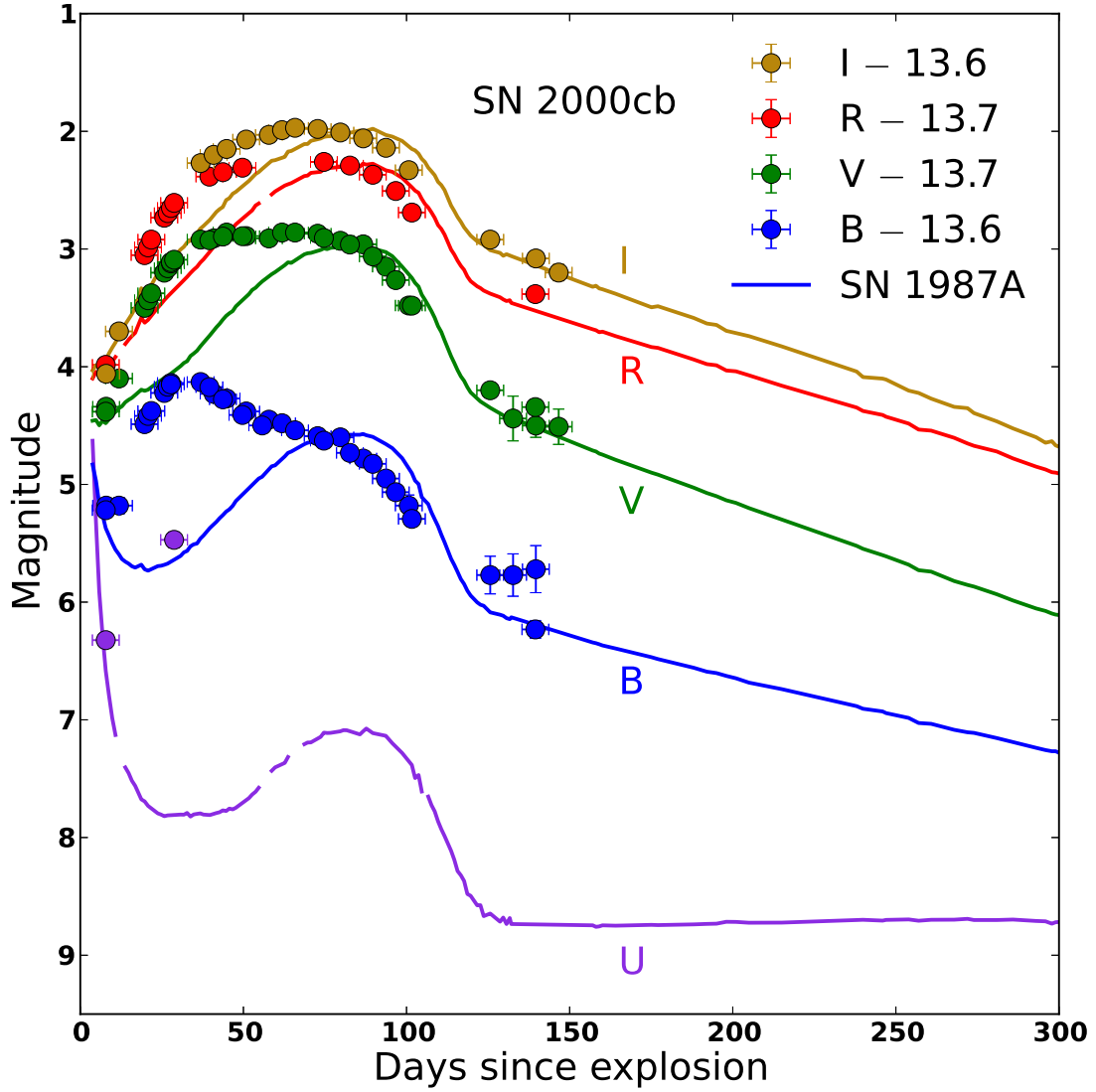


Figure 2.3 Photometric lightcurves of SN 2000cb, offset to match the peak magnitudes of the corresponding photometry of SN 1987A. Photometry of SN 2000cb from Hamuy (2001) and Kleiser et al. (2011), and photometry of SN 1987A from Hamuy and Suntzeff (1990) (solid lines.)

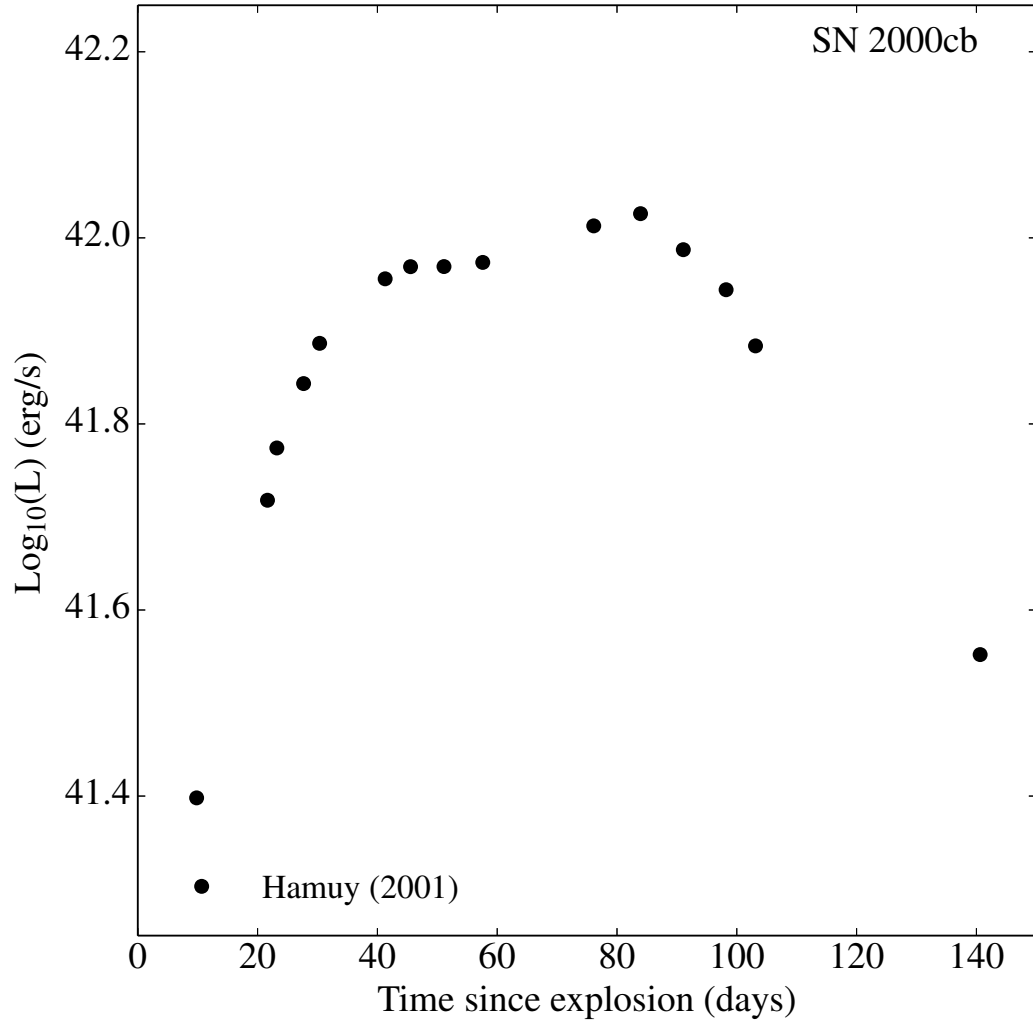


Figure 2.4 Bolometric lightcurve of SN 2000cb from Hamuy (2001) calculated using a bolometric correction technique with polynomial coefficients published in Hamuy (2001, Table 5.1).

SN 2006V undertaken by Taddia et al. (2012): Using a Hubble constant of $H_0 = 73.8 \pm 2.4 \text{ km s}^{-1} \text{ Mpc}^{-1}$ (Riess et al., 2011) and the measured redshift of the supernova of $z = 0.0157 \pm 0.0013$, the distance is calculated to be $72.7 \pm 5 \text{ Mpc}$. The lack of Na I D absorption in the spectra of SN 2006V lead Taddia et al. (2012) to rule out significant host galaxy extinction, and use the NED² value of $E(B - V)_{\text{gal}} = 0.029$ from Schlegel et al. (1998) with the Cardelli et al. (1989) slope of $R_v = 3.1$ to give $A_{V, \text{gal}} = 0.09$. Taddia et al. (2012) use EPM analysis (outlined in their section 5.1) to constrain the explosion epoch of SN 2006V to JD 2453748 ± 4 .

The photometric data from Taddia et al. (2012) are shown in comparison to the lightcurves of SN 1987A in Figure 2.3, with offsets applied to the magnitudes in each band in order to match those of SN 1987A as closely as possible. Because the photometry of SN 2006V was taken using a photometric system specific to the Carnegie Supernova Project, *i* and *r*-band observations of SN 2006V are transformed into *I* and *R*-bands using transformation equations derived by Robert Lupton (2005)³. These transformations are not exact, as they apply to the SDSS photometric system defined in Fukugita et al. (1996) rather than the CSP natural system. As noted in Taddia et al. (2012), the differences between the two systems are insignificant for the rough comparisons made in this analysis, and would only become important for precision cosmology measurements.

The agreement between the photometric evolution of SN 2006V and SN 1987A

²<https://ned.ipac.caltech.edu/>

³<http://www.sdss3.org/dr10/algorithms/sdssUBVRITransform.php#Lupton2005>

is excellent: SN 2006V exhibits an almost identical dome-like lightcurve to that of SN 1987A, with very similar rise times. The transition to the radioactive tail also occurs at an almost identical epoch in the two objects.

The bolometric lightcurve of SN 2006V has been published previously in Taddia et al. (2012) (their Figure 14). As mentioned in subsection 1.3.1, this bolometric luminosity was calculated using a modified direct integration technique, where observed magnitudes were first converted to fluxes, and then a cubic spline function was fit to the flux points. This cubic polynomial was then integrated over wavelength, with corrections made for IR flux by integrating a Rayleigh-Jeans tail redward of the H band and Wien tail blueward of the u band.

Figure 2.6 shows the bolometric luminosity of SN 2006V, as calculated in Taddia et al. (2012) using the values of extinction, distance, and explosion time mentioned above.

2.4 SN 2006au

SN 2006au was discovered on 2006 March 7.2 by Trondal et al. (2006) as part of the Tenagra Observatory Supernova Search. The supernova was located at $\alpha = 17^{\text{h}}57^{\text{m}}13^{\text{s}}.56$, $\delta = +12^{\circ}11'03''.2$ (J2000) in the spiral galaxy UGC 11057. Photometry of the supernova was first published in Taddia et al. (2012), along with the data from SN 2006V.

The distance, reddening, and explosion date are taken from Taddia et al. (2012). Using the same techniques as described in section 2.3 the distance to SN 2006au was found to be 46.2 ± 3.2 Mpc. Taddia et al. (2012) find clear Na I

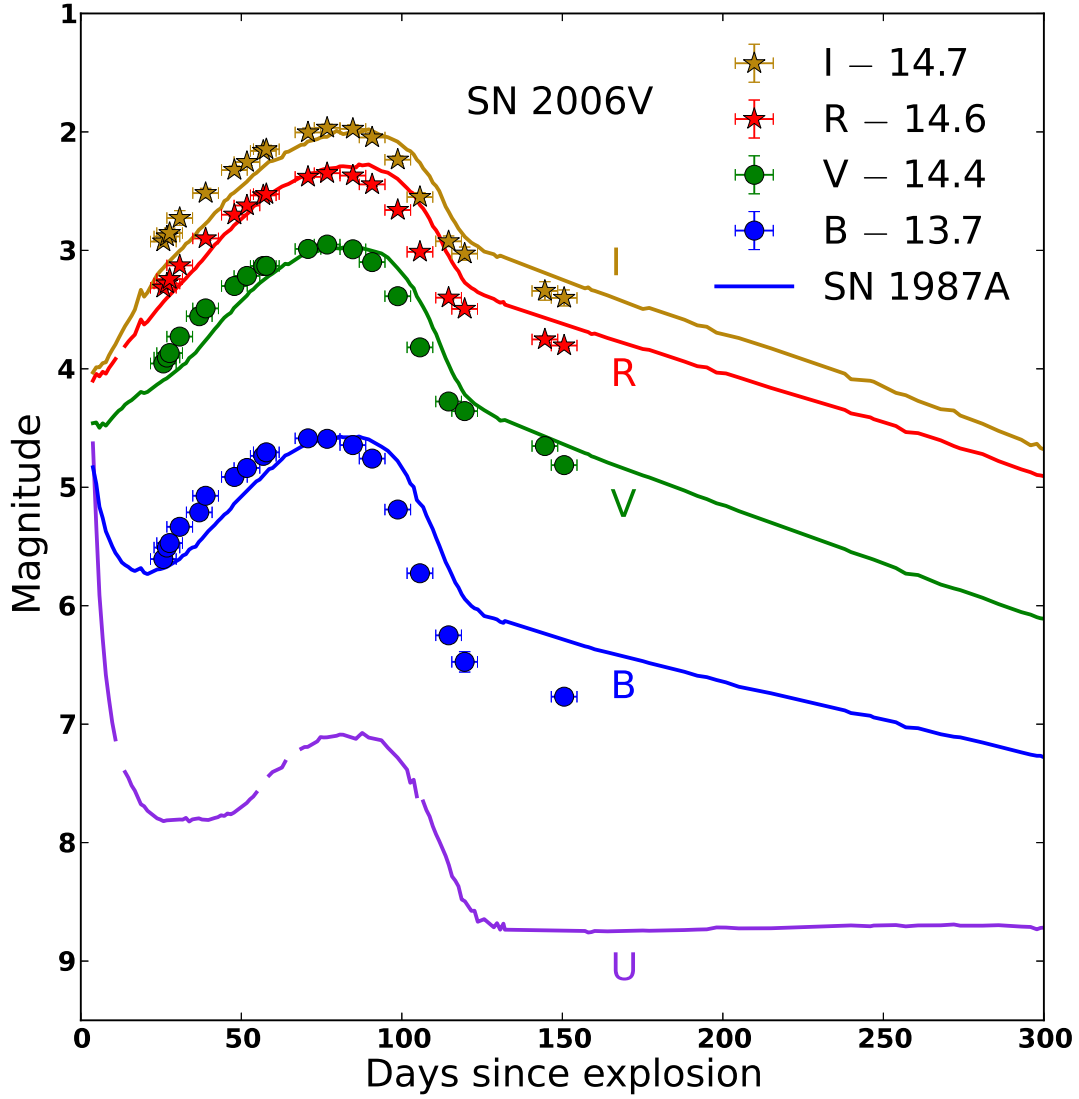


Figure 2.5 Photometric lightcurves of SN 2006V, offset to match the peak magnitudes of the corresponding photometry of SN 1987A. Photometry of SN 2006V from Taddia et al. (2012), with stars designating photometric points transformed from the CSP natural system to the BVRI system. Photometry of SN 1987A from Hamuy and Suntzeff (1990) (solid lines.)

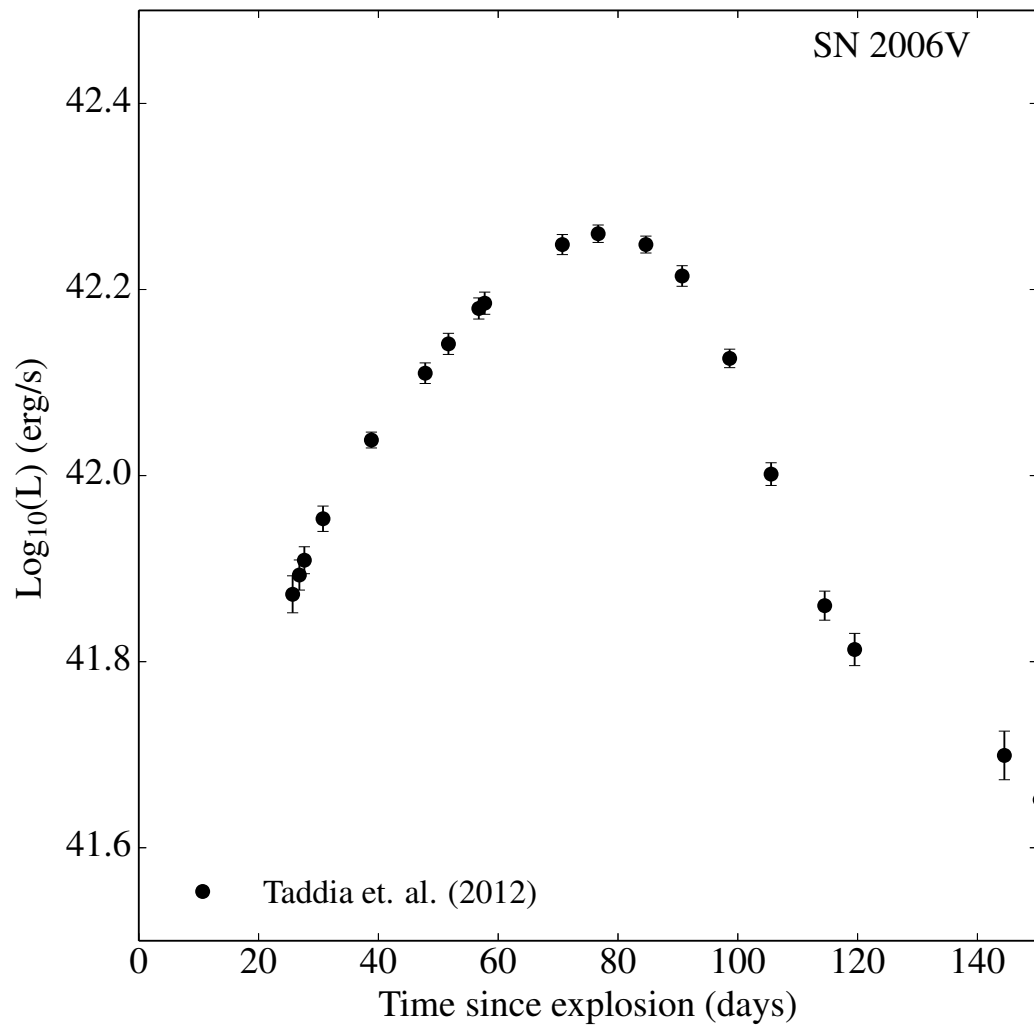


Figure 2.6 Bolometric lightcurve of SN 2006V from Taddia et al. (2012) calculated using an augmented bolometric technique.

D absorption lines in the spectrum of SN 2006au with an equivalent width of $0.88 \pm 0.11 \text{ \AA}$, and a corresponding host galaxy color excess of $E(B - V)_{\text{host}} = 0.141$ using the correlation between Na I D equivalent width and host galaxy reddening published in Turatto et al. (2003). Combining this value with the Schlegel et al. (1998) value of galactic color excess $E(B - V)_{\text{gal}} = 0.172$ gives $A_{V, \text{TOT}} = 0.97$. Using EPM estimates, Taddia et al. (2012) constrain the explosion date to $\text{JD } 2453794 \pm 9$.

The photometric comparison between SN 2006au and SN 1987A is shown in Figure 2.7. Because SN 2006au was observed using the same CSP natural photometric system described in section 2.3, the transformations to I and R -band photometry were accomplished in the same way as for SN 2006V.

The photometric evolution of SN 2006au differs from that of SN 1987A at early times. Taddia et al. (2012) suggests that the initial decrease in brightness evident in the B , r , and i bands might be evidence of the photospheric cooling that follows the break-out of the shock at the surface of the progenitor. Similar evolution can be seen in the B and U lightcurves of SN 1987A.

The other significant difference between the photometric evolution of SN 2006au and SN 1987A occurs during the transition to the radioactive tail. SN 2006au shows a much steeper drop from peak luminosity, and while the photometric observations of SN 2006au do not continue beyond the transition to the radioactive tail, the last few observed magnitudes are much dimmer than the corresponding SN 1987A lightcurves. This suggests that the mass of ^{56}Ni ejected by SN 2006au might have been significantly lower than that of the other supernovae in this

sample.

Figure 2.8 shows the bolometric lightcurve of SN 2006au. The bolometric lightcurve of SN 2006au was calculated in the same way as that of SN 2006V, using the extinction, distance, and explosion date discussed above.

2.5 SN 2009E

SN 2009E was discovered on 2009 January 3.06 UT by Boles, 2009 in the spiral galaxy NGC 4141, at location $\alpha = 03^{\text{h}}54^{\text{m}}22^{\text{s}}.83$ and $\delta = -19^{\circ}10'54''.2$. Prosperi and Hurst, 2009 noted that observations of the supernova on 2009 March 8.05 UT show that it has brightened by a full magnitude over the course of a month. Follow-up spectroscopy on 2009 March 24.88 UT by Navasardyan et al. (2009) revealed SN 2009E to be a type II supernova with strong barium features analogous to SN 1987A.

Photometry of the object was first published by Pastorello et al. (2012). For the first three months of observation, the object was monitored largely by amateur astronomers (for details on the reduction and calibration of unfiltered amateur images, see Pastorello et al., 2012). The observational parameters of the supernova are given in Table 4.1. The explosion date of SN 2012E was found to be $\text{JD } 2454832.5^{+2}_{-5}$ by comparing the early photometric evolution to that of SN 1987A. The distance to the host galaxy was calculated to be 29.97 ± 2.10 Mpc using the redshift and a Hubble constant of $H_0 = 72 \pm 5 \text{ km s}^{-1} \text{ Mpc}^{-1}$. The galactic extinction from Schlegel et al. (1998) in the direction of SN 2009E is $E(B - V)_{\text{gal}} = 0.02$. Evidence of faint Na I D absorption in the spectrum suggests

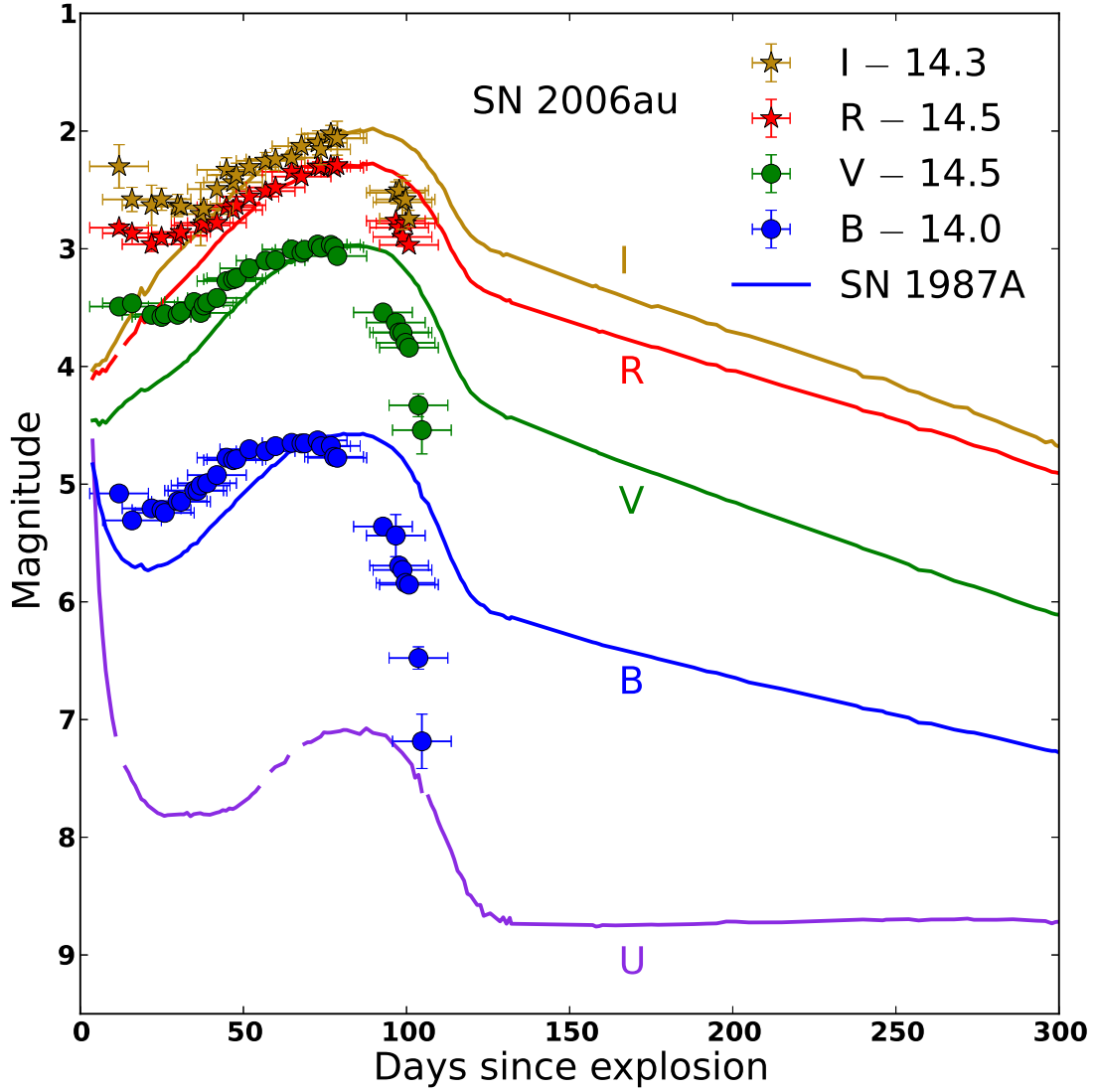


Figure 2.7 Photometric lightcurves of SN 2006au, offset to match the peak magnitudes of the corresponding photometry of SN 1987A. Photometry of SN 2006au from Taddia et al. (2012), with stars designating photometric points transformed from the CSP natural system to the BVRI system. Photometry of SN 1987A from Hamuy and Suntzeff (1990) (solid lines.)

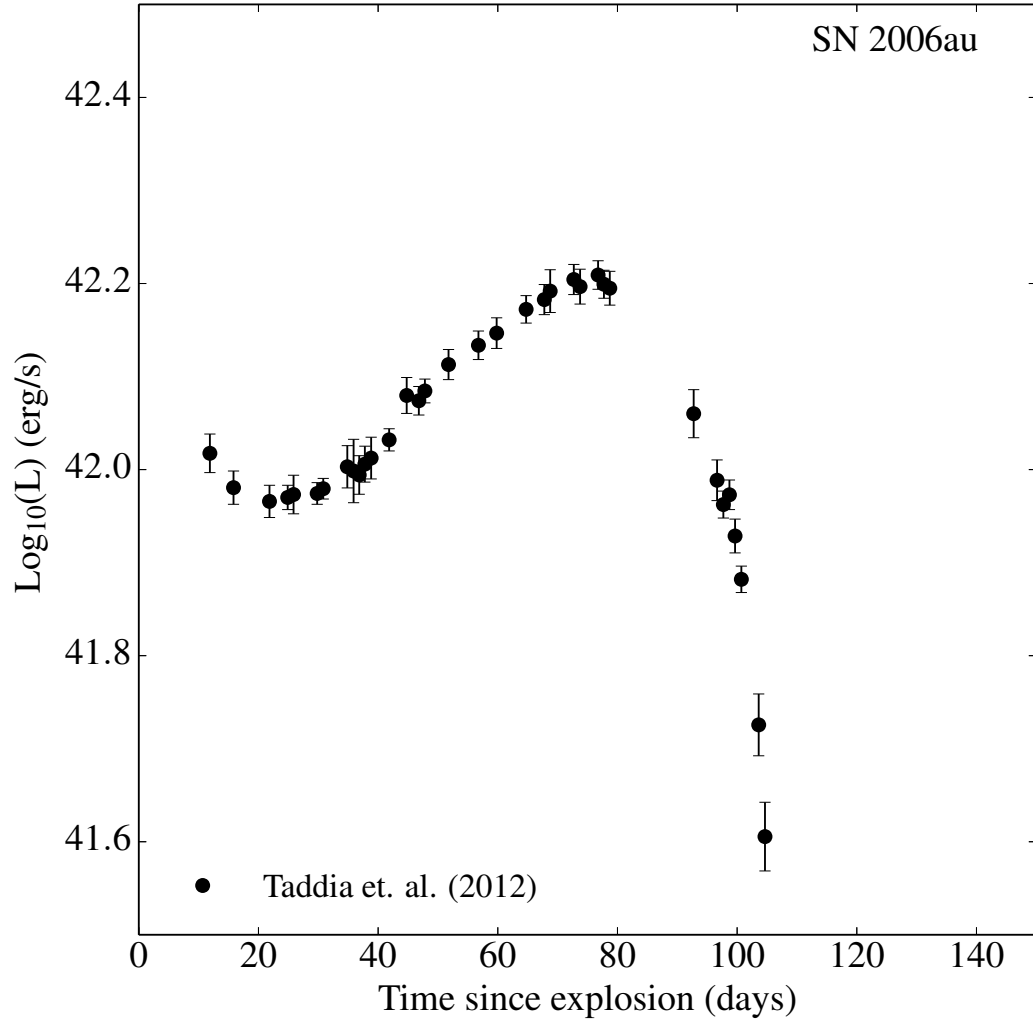


Figure 2.8 Bolometric lightcurve of SN 2006au from Taddia et al. (2012) calculated using an augmented bolometric technique.

a host galaxy extinction of $E(B - V)_{\text{host}} = 0.02$ using the relation of Turatto et al. (2003), for a total extinction of $E(B - V)_{\text{tot}} = 0.04$. With the Cardelli et al. (1989) slope of $R_V = 3.1$, the value of $A_{V, \text{TOT}} = 0.124$.

The photometric evolution of SN 2009E is compared with the lightcurves of SN 1987A in Figure 2.9. The overall evolution of SN 2009E is an excellent match to that of SN 1987A, much like SN 1998A and SN 2006V. The extensive late-time observations of SN 1998A on the radioactive tail show a declining lightcurve with the signature slope of ^{56}Ni decay.

The bolometric lightcurve of SN 2009E was first reported in Pastorello et al. (2012). The quasi-bolometric lightcurve was found by converting the observed photometry to monochromatic flux, then integrating over wavelength. Corrections for unobserved flux were made by assuming the color evolution was identical to SN 1987A, and scaling the quasi-bolometric flux of SN 2009E by the ratio of the bolometric to quasi-bolometric flux of SN 1987A (see Equation 1.9)

Figure 2.10 shows the bolometric lightcurve of SN 2009E calculated by Pastorello et al. (2012). The gap in multi-band observations during the rising phase of the lightcurve is evident, but the plateau, transition to the radioactive tail, and the radioactive tail itself are well-sampled.

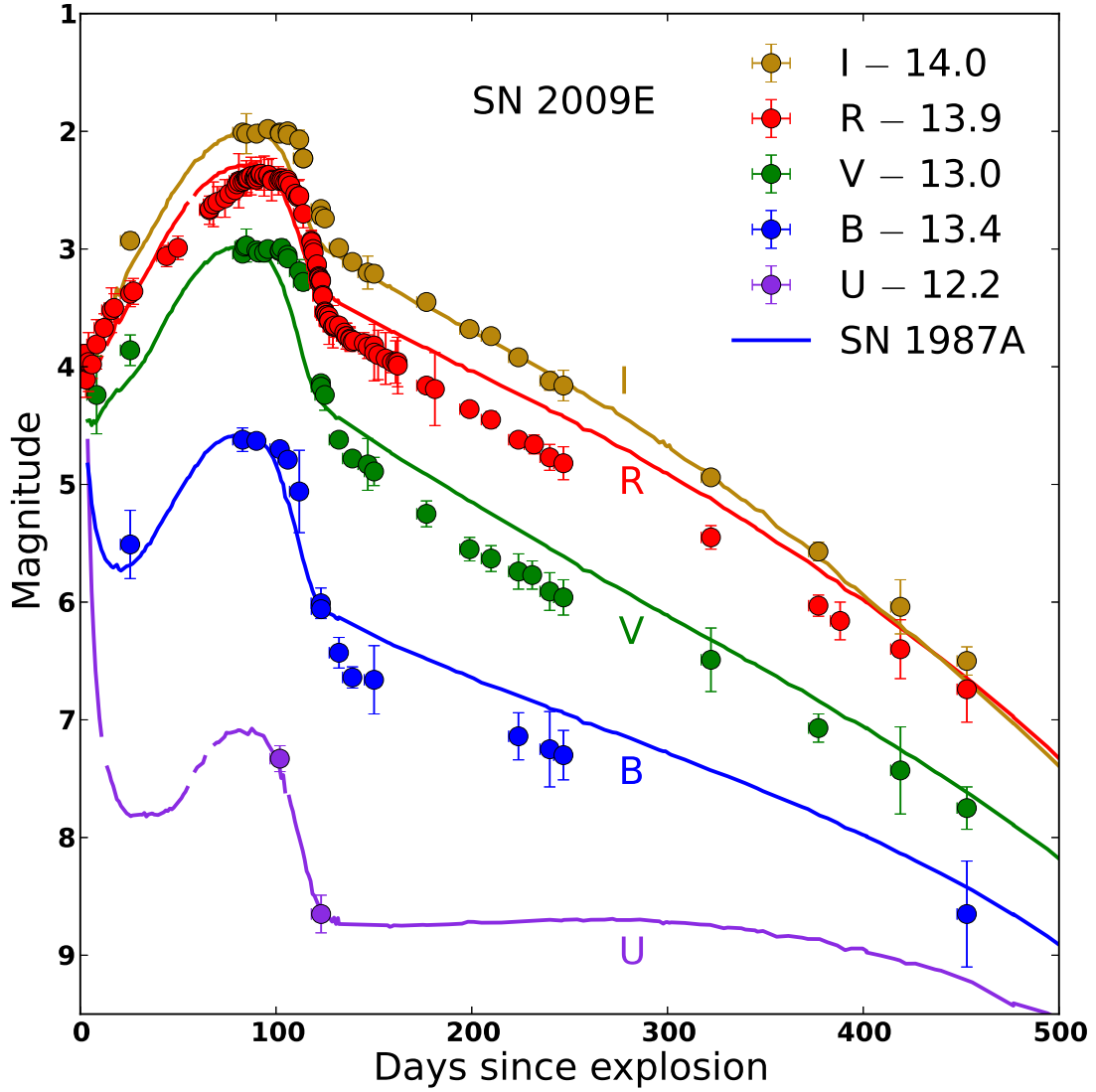


Figure 2.9 Photometric lightcurves of SN 2009E, offset to match the peak magnitudes of the corresponding photometry of SN 1987A. Photometry of SN 2009E from Pastorello et al. (2012), and photometry of SN 1987A from Hamuy and Suntzeff (1990) (solid lines.)

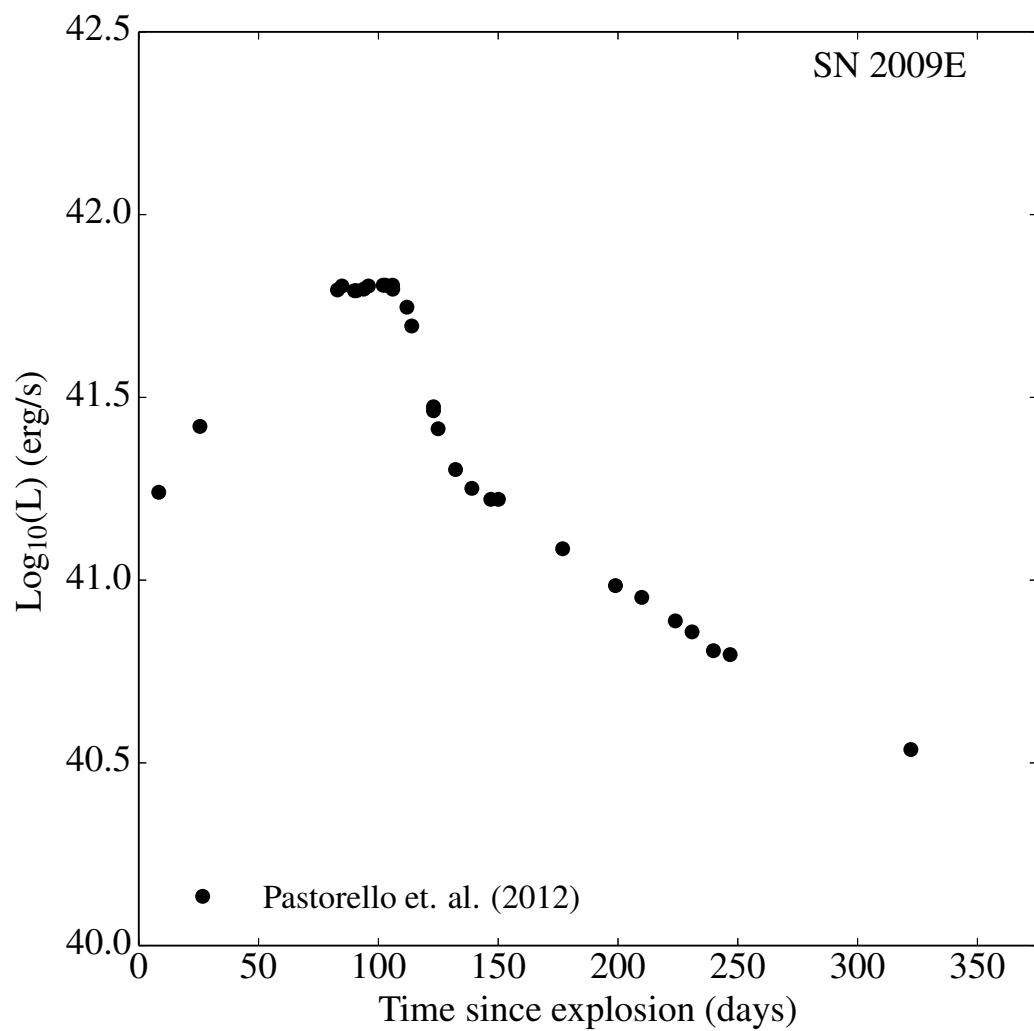


Figure 2.10 Bolometric lightcurve of SN 2009E from Pastorello et al. (2012) calculated using a quasi-bolometric technique augmented by assuming an identical color evolution to that of SN 1987A.

Chapter 3

SuperBoL: Supernova Bolometric Lightcurves

3.1 Introduction

SuperBoL (Supernova Bolometric Lightcurves) is a program written to help researchers calculate the bolometric lightcurves of supernovae using a variety of techniques from the literature. It is written in the `Python`¹ programming language – a high-level, general purpose programming language that allows SuperBoL a high degree of modularity and extensibility. `Python` is especially useful in the field of astronomy thanks to the many freely-available packages which add functionality for scientific computing (`SciPy`², `NumPy`³) and astronomy (`Astropy`⁴, and affiliated packages.)

SuperBoL implements three primary techniques for calculating the bolometric luminosity of a supernova: the *quasi-bolometric* technique, described in subsection 1.3.1 the *augmented bolometric* technique, described in subsection 1.3.2 and the *bolometric correction* technique, described in section 1.4. These techniques were chosen because variations of these techniques are the most widely used in the literature.

¹<https://www.python.org>

²<https://www.scipy.org>

³<https://www.numpy.org>

⁴<https://www.astropy.org>

In the sections to follow, the core utilities of **SuperBoL** will be described, including the external **Python** packages utilized for certain operations like extinction correction and integration. In chapter 1, the different techniques for calculating bolometric luminosities were described from a theoretical standpoint. In section 3.3, the details of how those techniques are implemented in **SuperBoL** will be described. Finally, in section 3.4, the process used to test that the code within **SuperBoL** is functioning as expected will be described, along with several validation tests, in which **SuperBoL** is used to estimate the luminosity of an object where the luminosity is known (blackbody fluxes, white dwarf models, and the supernova SN 1987A)

The **SuperBoL** code is open-source and available on GitHub⁵. This repository includes the photometry of the supernovae studied in this paper, making it possible to re-produce the results detailed in chapter 4. Contributions, corrections, and feature requests from the community are welcomed through GitHub.

3.2 Core Utilities

In order to take advantage of the modular nature of **SuperBoL**, a number of functions and utilities common to the various bolometric luminosity calculation techniques can be separated into their own **Python** modules within **SuperBoL**. In addition, there are several tasks that can be performed using external packages such as **SciPy**, **NumPy**, and **Astropy**. In the following sections, the core utilities and external libraries used by **SuperBoL** are described.

⁵<https://github.com/JALusk/SuperBoL>

3.2.1 mag2flux module

In the `mag2flux` module, several important `Python` classes are implemented that are used throughout the code. Together, these classes are responsible for holding the observed photometric data and converting an observed magnitude into a monochromatic flux at the effective wavelength of the photometric band used for the observations.

Because the main purpose of `SuperBoL` is to generate bolometric luminosities from observed photometry, the `ObservedMagnitude` class exists to encapsulate the data associated with a single photometric observation of a supernova. The class has attributes to store the magnitude, uncertainty, and time of the observation (in JD,) as well as the photometric band used in the observation. The `band` attribute of the `ObservedMagnitude` class holds another custom class, the `Band`. A `Band` is another data container that holds information about a photometric band. Its attributes include the name of the band, the effective wavelength of the band, and the flux conversion factor. This flux conversion factor is equivalent to the flux at zero magnitude f_0 , and is used by the `ObservedMagnitude` class to convert an observed magnitude to a monochromatic flux f using Equation 3.1

$$f = f_0 \times 10^{-0.4m} \quad (3.1)$$

The data for the bands used in `SuperBoL` is stored in a JSON file, to make it easier for future users to add more photometric bands to the program.

Once an `ObservedMagnitude` has been converted to flux, the resulting object is

a `MonochromaticFlux`. This class forms the building block of the spectral energy distribution which is used in the quasi-bolometric and augmented bolometric techniques. The `ObservedMagnitude` contains attributes to hold the flux, uncertainty, wavelength, and time (in JD) of the converted photometric magnitude.

3.2.2 photometry module

The `photometry` module contains functions which are responsible for processing a long list of `ObservedMagnitude` objects into smaller lists of `ObservedMagnitude` objects which have been grouped in time, had repeated observations averaged together, and optionally had missing observations filled in by interpolation.

The first task which must be performed by the `photometry` module is grouping observations in time. In a typical published table of photometric observations (see, e.g. Taddia et al., 2012, Table 3) the magnitudes observed in each photometric band are grouped by time. However, photometric observations are not made simultaneously, and sometimes when the photometry is made available in digital form, each photometric magnitude in each band is stamped with the unique JD of the observation. This means that bands observed on the same night have different JD values. This issue is made more complicated when attempting to combine together photometry from different telescopes at different observatories. Because of the physical separation in the observing sites, the observations of the same object on the same “night” can be spread out over many hours.

The default behavior of `SuperBoL` is to group together `ObservedMagnitude` objects by applying the `math.floor()` function to their `time` attributes. However,

to allow for flexibility in future versions of the code, the `group_magnitudes()` function which performs this operation is written in such a way that the user can choose to supply a different “key function” than `math.floor()`. Any `ObservedMagnitude` objects for which the supplied `keyfunc()` returns the same value will be grouped together by the code.

Now grouped in time, the next operation performed is combining repeated observations together. Since the Δt used in the default grouping is one day, it is possible that the same photometric band could be observed multiple times in the same grouping. Any repeated observations are combined together using a weighted average (Equation 3.2,) where the uncertainties in the photometric observations δm_i are used to calculate weights $w_i = 1/(\delta m_i)^2$ used in the weighed average of the repeated observations \bar{m} :

$$\bar{m} = \frac{\sum w_i m_i}{\sum w_i}. \quad (3.2)$$

The result of this processing is a “list of lists” where each inner list is a referred to as “multi-band photometry” because it contains contemporaneous `ObservedMagnitude` objects, perhaps resulting from averaging together multiple observations using the same photometric band.

In newer versions of `SuperBoL`, it is possible to take this list of lists and use it to interpolate for missing observations. Rather than grouping observations in time, it is necessary to group the observations by band, and then test to see if there are missing observations in each group. The current behavior of `SuperBoL` is to

only fill in missing magnitudes if the gap between the previous and next observed magnitude in the same band is less than or equal to 2 days. This criteria is quite restrictive, but can be changed by the user if required. The interpolation itself is performed using the `interp1d()` function from the `scipy.interpolate` module. In future versions of **SuperBoL**, it will be possible to use different interpolation schemes (for example, using a low-order polynomial as mentioned in Folatelli et al. (2006).)

After being processed by the `photometry` module, the `ObservedMagnitude` objects which were grouped together in time can be converted to `MonochromaticFlux` objects to form an SED.

3.2.3 blackbody module

The `blackbody` module handles the fitting of a blackbody flux to the SED constructed using the `photometry` module. This is accomplished using a custom `BlackbodyFit` object. This is one example from **SuperBoL** where the object-oriented nature of `Python` becomes quite useful. When fitting a blackbody function to a set of fluxes, it is necessary to pass the individual wavelengths and flux values of the SED, along with the uncertainties in those flux values. Once those have been fed into the fitting function (in this case the `curve_fit` function from the `scipy.optimize` module) the results are the best-fit values temperature, angular radius, and a covariance matrix. However, the utility of those values lies in constructing a blackbody curve that can be integrated. In another programming paradigm, those values might then need to be passed back to a blackbody flux

function for plotting or to a numerical integration scheme which approximates the integral of the Planck function.

With `Python` objects, it is possible to store the data associated with the fit along with the fitting function and the blackbody flux in one object - the `BlackbodyFit`. This object has attributes to store the temperature, angular radius, their associated uncertainties, and the SED being fit. Once initialized, the SED is input to the `fit_to_SED()` method, which uses the `curve_fit()` function from `scipy.optimize` to set the values for temperature, angular radius and their associated uncertainties as attributes of the `BlackbodyFit` object. Once set, the `Python` “magic method” `__call__()` makes the object act like a function - when given a wavelength, the object will return the flux (in cgs units) of the best fit blackbody at the given wavelength. This is especially helpful when plotting the function and calculating the UV and IR corrections (see subsection 3.3.2)

3.3 Implementation

As can be seen in chapter 2, a wide variety of techniques have been used in the literature to determine the bolometric luminosities of supernovae with BSG progenitors. This itself is a subset of the techniques which have been used to calculate the bolometric luminosities of supernovae, in general — some of which were discussed in section 1.1.

The goal of writing `SuperBoL` is to provide the community with a set of standardized tools to calculate L_{bol} , and to provide best estimates of the uncertainties in those calculations.

3.3.1 Quasi-bolometric technique in SuperBoL

SuperBoL implements the quasi-bolometric technique described in subsection 1.3.1. This requires that the observed magnitudes be converted to a discrete flux-vs-wavelength SED. To accomplish this, the full set of observed photometry from a supernova is read in and converted to a list of `ObservedMagnitude` objects, which is processed according to subsection 3.2.2 and converted to flux using the `mag2flux` module described in subsection 3.2.1 to form SEDs at each observed epoch.

By default, The quasi-bolometric flux F_{qbol} is calculated by the trapezoidal integration technique detailed in subsection 1.3.1 using the `trapz` routine in the `numpy` package⁶. However, the `fqbol` module which handles the calculation of the quasi-bolometric flux is flexible, and in the future other integral calculation schemes can be used, such as a cubic spline fit to the SED as in Taddia et al. (2012).

3.3.2 Augmented bolometric technique in SuperBoL

SuperBoL implements an augmented bolometric technique based on the one published in Bersten and Hamuy, 2009. The first step in this technique is calculating the quasi-bolometric flux using the method outlined in subsection 3.3.1. Once the quasi-bolometric flux has been obtained, it needs to be augmented by a UV correction and an IR correction.

⁶<http://www.numpy.org/>

In order to estimate missing flux in the IR (F_{IR}), a blackbody spectrum is fit to the observed fluxes using the `curve_fit` function from the python package `scipy`⁷ (Jones et al., 2001) as outlined in subsection 3.2.3. The best-fit blackbody curve is then integrated from the longest observed effective wavelength to $\lambda = \infty$.

Missing flux in the UV (F_{UV}) is handled differently depending on the quality of the blackbody fit. To best re-create the method described in Bersten and Hamuy (2009), the blackbody fit is again integrated, this time from the shortest observed wavelength to $\lambda = 0$, unless the U -filter flux falls below that blackbody fit, in which case a linear function linking the shortest observed flux and $f_{\lambda} = 0$ at $\lambda = 2000 \text{ \AA}$ is integrated instead. By default, if no U -filter observations are available, the integrated blackbody flux is integrated from $\lambda = 0$ the shortest wavelength flux in the SED to calculate F_{UV}

The integration of the Planck function proved unreliable with standard integration packages such as `integrate.quad` from `scipy`. To overcome this difficulty, the discrete integral of the Planck function can be expressed as an infinite series as shown in Equation 3.3 (Michels, 1968; Widger and Woodall, 1976):

$$\int_0^{\lambda_1} B_{\lambda}(\lambda, T) d\lambda = \frac{C_1 T^4}{C_2^4} \sum_{n=1}^{\infty} \left(\frac{x_1^3}{n} + \frac{3x_1^2}{n^2} + \frac{6x_1}{n^3} + \frac{6}{n^4} \right) e^{-nx_1} \quad (3.3)$$

where $C_1 = 2hc^2$ and $C_2 = hc/k_B$ are the first and second radiation constants, and $x_1 = C_2/\lambda_1 T$. This infinite series is truncated in **SuperBoL** to produce accuracies to ten digits. The rate of convergence in the series depends upon the

⁷<http://www.scipy.org>

value of x_1 , and in order to achieve this accuracy we found we had to include $n = \min(2 + 20/x_1, 512)$ terms in the series⁸. Calculating the IR correction is accomplished in the following manner:

$$\int_{\lambda_2}^{\infty} B_{\lambda}(\lambda, T) d\lambda = \int_0^{\infty} B_{\lambda}(\lambda, T) d\lambda - \int_0^{\lambda_2} B_{\lambda}(\lambda, T) d\lambda \quad (3.4)$$

where the first term is given by the Stefan-Boltzmann law as σT^4 , and the second term is calculated using the series solution above.

The three fluxes, F_{qbol} , F_{IR} and F_{UV} are added together to form the bolometric flux F_{bol} . This flux is then converted to a luminosity using the standard relation

$$L_{\text{bol}} = 4\pi D^2 F_{\text{bol}}, \quad (3.5)$$

with D taken from Table 4.1.

3.3.3 Bolometric correction in SuperBoL

SuperBoL implements two sets of polynomial coefficients c_i in Equation 1.12: one set from Hamuy (2001) and another from Bersten and Hamuy (2009), although in the future **SuperBoL** will be modified to calculate the bolometric luminosity using any set of coefficients and two-filter colors. Pejcha and Prieto (2015) have shown (their Figure 16) that the results obtained when using the different sets of coefficients outlined in section 1.4 are broadly similar, especially over the range of colors typical of our sample of peculiar Type II-P supernovae ($0.5 \lesssim B - V \lesssim 1.5$,

⁸http://www.spectralcalc.com/blackbody/inband_radiance.html

$$0.5 \lesssim V - I \lesssim 1.0.)$$

We have chosen to average together the results from calculating the bolometric luminosity based on the bolometric correction obtained from $B - V$, $V - I$, and $B - I$ colors ($B - V$ and $V - I$ in the case of using the polynomial coefficients from Hamuy (2001).) **SuperBoL** calculates luminosities based on as many of the color combinations as possible on a given JD before averaging.

3.3.4 Propagation of uncertainties in SuperBoL

One of the goals of producing lightcurves with **SuperBoL** is to estimate the uncertainty in our final bolometric luminosities. This can then be used to constrain the uncertainties in progenitor properties found by matching theoretical lightcurves to observed ones.

The basic input data to **SuperBoL** includes the observed photometry m_X , the explosion date t_0 , the total visual extinction $A_{V, \text{TOT}}$, and the distance D . Uncertainties in the distance and explosion date are shown in Table 4.1, while uncertainties in the observed photometry for each SN are provided in the sources referenced in chapter 2. All of these measurements and uncertainties are included in the HDF5 file used as a database by **SuperBoL**.

We have used the general formula for error propagation (see, for example, Taylor, 1997, Eq. 3.47) in our code to ensure that uncertainties in the basic input data are reflected in the final luminosity. For certain numerical operations, this is not so straightforward. As an example, we must fit a blackbody curve to the observed fluxes. We compute one standard deviation uncertainties on the

fitted parameters by calculating the square root of the diagonal terms in the covariance matrix output by `curve_fit`. Those standard deviations are then used as the uncertainties in those parameters for the purposes of propagation. We also assume that the RMS dispersions listed in Table 1 of Bersten and Hamuy (2009) represent the standard deviation σ_{BC} of the bolometric correction $BC(\text{color})$ in our uncertainty propagation. Uncertainties in the UV and IR correction due to the temperature can be calculated by taking derivatives of the series solution given in Equation 3.3 with respect to the temperature. These are included in our uncertainty calculations.

3.4 Testing and Validation of SuperBoL

3.4.1 Unit Testing

SuperBoL makes use of the `unittest` module of `python`, and is written using the Test-Driven Development (TDD) programming paradigm. The result is that all of the functions in SuperBoL are automatically tested for correctness in isolation with a single command. This serves the dual purpose of ensuring that the program works as intended and making explicit what the intended behavior of each function is. Because the tests can be run automatically and quickly, developers can make changes or add features and know immediately if those modifications have broken the functionality of code elsewhere in the program.

This does not ensure, however, that the overall results of the code are correct – merely that the individual functions produce expected results given certain

inputs. In order to test that the code functions correctly, we need to compare the luminosities produced by **SuperBoL** with known good luminosities of astrophysical origin. We do this in two ways — first with synthetic photometry from blackbody models, and then with synthetic photometry from the pure helium white dwarf (WD) atmosphere models of Holberg and Bergeron (2006), Kowalski and Saumon (2006), and Tremblay et al. (2011) and Bergeron et al. (2011), available online⁹.

3.4.2 Validation using blackbody models

The grid of blackbody models was generated to have the same temperatures and luminosities as the white dwarf models, and synthetic photometry was performed to determine absolute magnitudes in the *UBVRIJK* and *ugriz* bands.

In Figure 3.1, we compare the **SuperBoL**-derived luminosities with the luminosities of the blackbody models. Here, the importance of making the UV and IR corrections correctly can be seen. The quasi-bolometric luminosity underestimates the true luminosity of the blackbody by 10-20% over the range of temperatures typical of the plateau phase of a Type II-P supernova. The disagreement increases as the temperature increases, due to an increasing fraction of the total flux shifting blueward of the bluest filter.

The direct integration scheme in **SuperBoL** performs much better, recovering the blackbody luminosity from synthetic photometry to within 3% over the range of 3500 K - 6000 K. Because the nature of the underlying spectrum is known, the UV correction was made using the blackbody fit integrated to $\lambda = 0$ rather than

⁹<http://www.astro.umontreal.ca/~bergeron/CoolingModels>

the linear interpolation detailed in subsection 3.3.2.

The gap between the true luminosity and the direct integration luminosity from **SuperBoL** widens as the temperature increases, partially due to mismatches between the true temperature of the blackbody model underlying the synthetic photometry and the temperature recovered from fitting a blackbody to the fluxes derived from those magnitudes. The mismatch is shown in Figure 3.2, which reveals that using `curve_fit` to determine the temperatures and angular radii slightly overestimates the temperatures and underestimates the angular radii of the blackbody models from which the synthetic photometry was taken. To show the extent to which these mismatches affect the luminosities, we re-computed the UV and IR corrections using the true temperatures and angular radii from our blackbody models rather than the ones found by fitting the monochromatic fluxes. As shown in Figure 3.1, This brings the luminosities derived from the high-temperature blackbody photometry to within 6% of the true luminosities.

3.4.3 Validation using white dwarf models

A comparison of the **SuperBoL**-derived luminosities with the luminosities calculated from the bolometric magnitudes given in the WD models is shown in Figure 3.3. The same methods were used in both cases, and the UV correction was again made using the full UV tail of the blackbody function rather than the linear interpolation. The WD model results closely resemble those of the blackbody models, and luminosities are recovered to within $\sim 3\%$ over the range typical of the plateau-phase of Type II-P supernovae. Using the true temperatures, **SuperBoL**

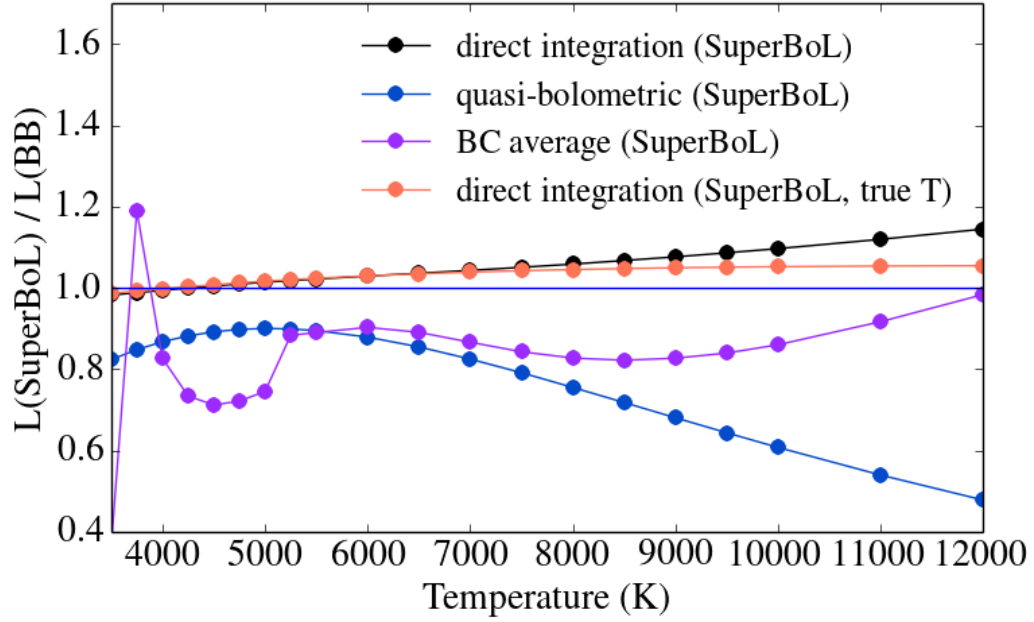


Figure 3.1 Ratio of **SuperBoL**-derived luminosity to blackbody model luminosity over a temperature range typical in the observed evolution of Type II-P supernovae.

recovers the luminosity to within $\sim 2\%$ over the temperature range 3500 K — 6000 K.

3.4.4 Reproducing SN 1987A lightcurve from Bersten and Hamuy (2009)

Our third test of **SuperBoL** was made using photometric data from SN 1987A. The bolometric lightcurve of this well-observed supernova has previously been published in Bersten and Hamuy (2009), using their direct integration technique described in subsection 1.3.2. Figure 3.4 shows the results of computing the bolometric lightcurve of SN 1987A using the three different techniques included in **SuperBoL**. We have adopted the same distance and reddening values of $D = 50 \pm 2$ kpc and

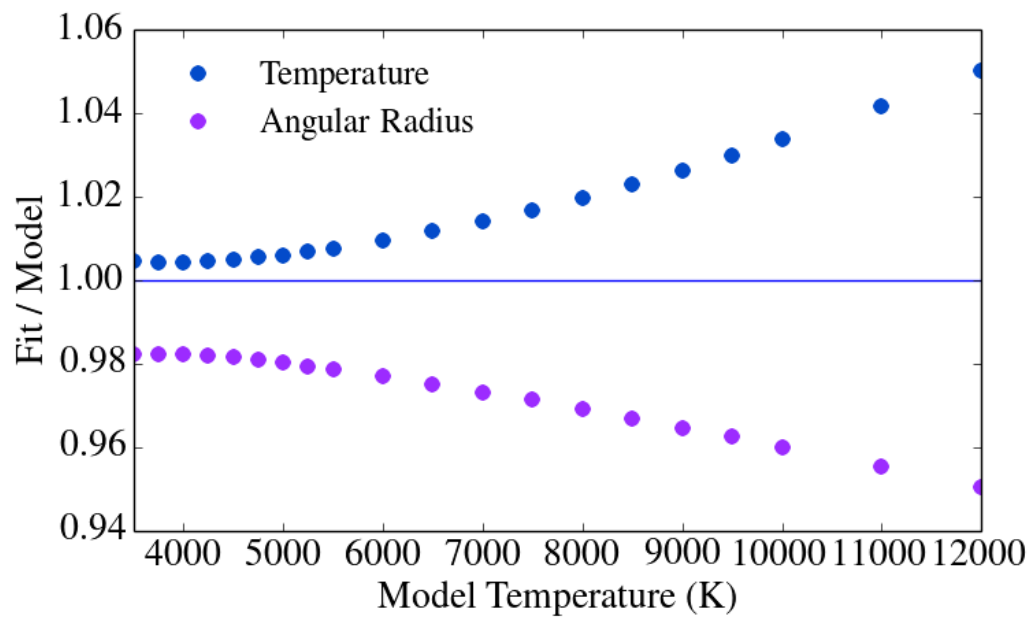


Figure 3.2 Ratio of **SuperBoL**-derived temperatures and angular radii to those of the blackbody models underlying the synthetic photometry used to validate the code.

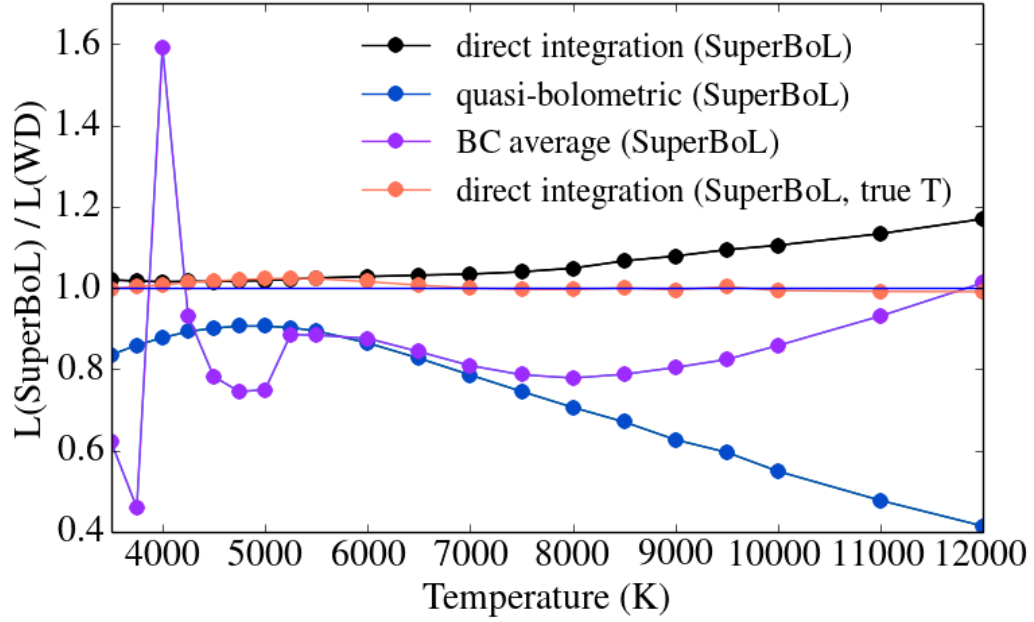


Figure 3.3 Ratio of **SuperBoL**-derived luminosity to white dwarf model luminosity over a temperature range typical in the observed evolution of Type II-P supernovae.

$A_{V, \text{tot}} = 0.465$, also from Bersten and Hamuy (2009).

The quasi-bolometric luminosity consistently under-estimates the luminosity of the supernova, to a degree that varies with the filters used. On nights when the wavelength coverage is good (in this case, U-K), the quasi-bolometric luminosity only slightly under-estimates the accepted luminosity of SN 1987A. However, on nights when the IR filters are unavailable, the quasi-bolometric luminosity drastically under-estimates the true luminosity of SN 1987a. This highlights the main drawback to using the quasi-bolometric method to estimate the luminosity of a supernova: uneven wavelength coverage will directly impact the results.

Our direct integration technique, only slightly modified from that of Bersten and Hamuy (2009), generates a bolometric lightcurve which largely agrees with the

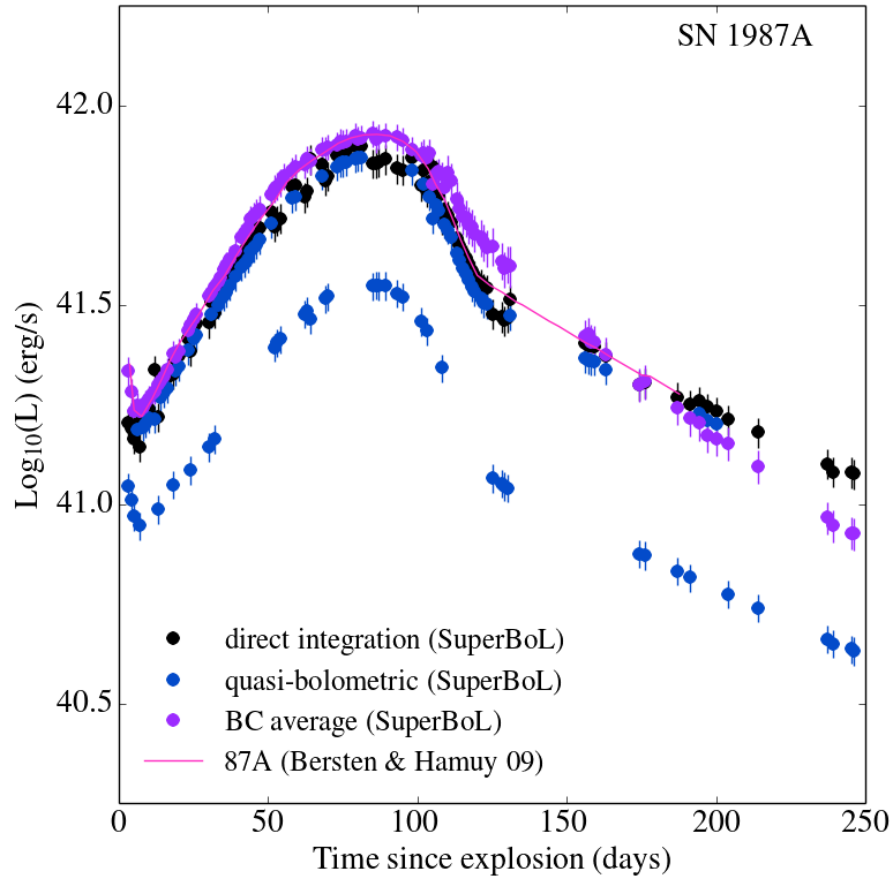


Figure 3.4 Bolometric lightcurves of SN 1987A. The previously published lightcurve is that of Bersten and Hamuy, 2009. The error-bars include the uncertainty in the distance to SN 1987A.

previously published lightcurve. One source of variation in our direct integration luminosity is the inconsistent wavelength coverage of the observations from night to night. Because we chose not to interpolate for missing observations, on nights where only the UBVRI bands were observed, the luminosity during the plateau phase is systematically lower than nights where U-K photometry was taken. This can be seen in Figure 3.5, where only the direct integration data is shown, and the points have been colored according to the wavelength coverage on that night. It should be noted, however, that this effect is largest during the plateau, diminishing as the supernova evolves into the nebular phase and onto the radioactive tail. The problem of inconsistent wavelength coverage from night to night is often treated in the literature by interpolating missing data using observations of previous and subsequent nights. However, we felt that the added complexity of testing the different interpolation schemes that have been used in the past was beyond the scope of this work (see, e.g. Folatelli et al., 2006; Lyman et al., 2014).

The bolometric correction method differs from the previously published lightcurve only at late times, from the transition to the radioactive tail onward. Indeed, Bersten and Hamuy (2009) warn that their published polynomial coefficients are valid only for the optically thick phase, and that the bolometric corrections during the nebular phase are very nearly independent of color. The remarkable agreement between the previously published lightcurve and the bolometric correction method during the rise to peak luminosity is to be expected — SN 1987A was the best-observed template supernova used by Bersten and Hamuy (2009) in the construction of their bolometric correction polynomials.

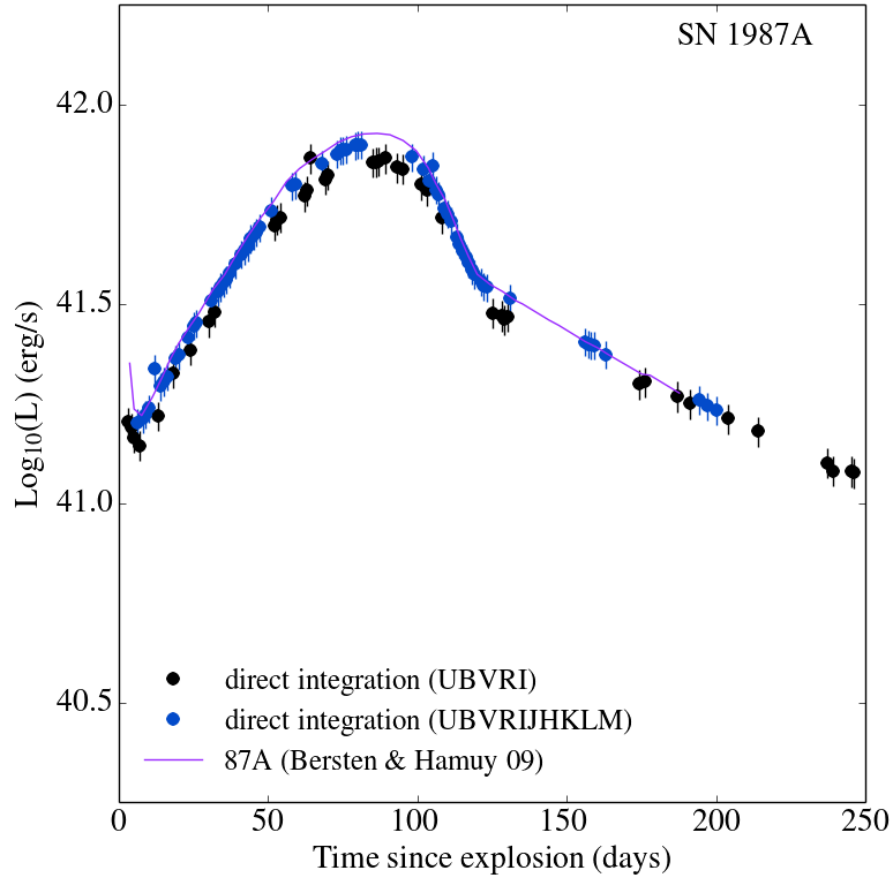


Figure 3.5 Direct integration lightcurve of SN 1987A. Note that on nights with only UBVR photometry, the luminosity is systematically lower during the plateau phase.

3.4.5 Reproducing SN 2000cb lightcurve from Hamuy (2001)

A final check of the bolometric correction module in **SuperBoL** can be made by attempting to re-produce the bolometric lightcurve of SN 2000cb published in Hamuy (2001).

Using the bolometric correction polynomials and “effective” bolometric magnitude zeropoint (see section 1.4) from Hamuy (2001) along with the published photometry from the same source, it is possible to re-create the bolometric lightcurve in Hamuy (2001), Figure 5.10.

The results of the comparison are shown in Figure 3.6. The error-bars in the **SuperBoL** lightcurve do not include the distance uncertainty, both to facilitate comparison with the previously published lightcurve and because both lightcurves use the same distance estimate and uncertainty. The bolometric luminosities produced by **SuperBoL** are nearly identical during the rise to peak luminosity (approximately the first 100 days after explosion.) Late in the evolution of the supernova, the lightcurves begin to disagree slightly, around 100 days post-explosion and around 140 days post-explosion.

The first datapoint on which the two lightcurves differ is on JD 2451752.70, approximately 99 days post-explosion. The source of the discrepancy seems to be the lack of *I*-band observations in the published photometry of SN 2000cb on that date. As mentioned previously, **SuperBoL** does not interpolate missing magnitudes if the gap in observations is as large as the one in the photometry of SN 2000cb (12 days, in this case.) The different criterion used for the interpolation

of missing photometry is also the reason why the previously published lightcurve includes a luminosity on JD 2451711.77 (approximately 58 days post-explosion.) On that date, only the B -band observation was made, the V and I bands were interpolated in Hamuy (2001) to obtain a bolometric luminosity using $B - V$ and $V - I$ color combinations.

However, it appears that in order to have a more complete photometric record, the bolometric luminosity published in Hamuy, 2001 does interpolate for the missing observation. With a linear interpolation to fill in the missing I -band magnitude, the **SuperBoL** average of the $B - V$ and $V - I$ luminosities on JD 2451752.70 is $8.95 \times 10^{41} \pm 2.88$ erg/s, which is a much closer match to the value inferred from Figure 5.10 of Hamuy (2001) of 8.79×10^{41} erg/s.

The value of the last point in the lightcurve from **SuperBoL** is $3.81 \times 10^{41} \pm 1.2$ erg/s, compared to $\sim 3.56 \times 10^{41}$ erg/s in the previously published lightcurve. Because the values of the previously published lightcurve were extracted from the plot itself rather than taken from a table of printed values, it is likely that this small discrepancy comes from the inherent uncertainty involved in re-producing a dataset from a plot.

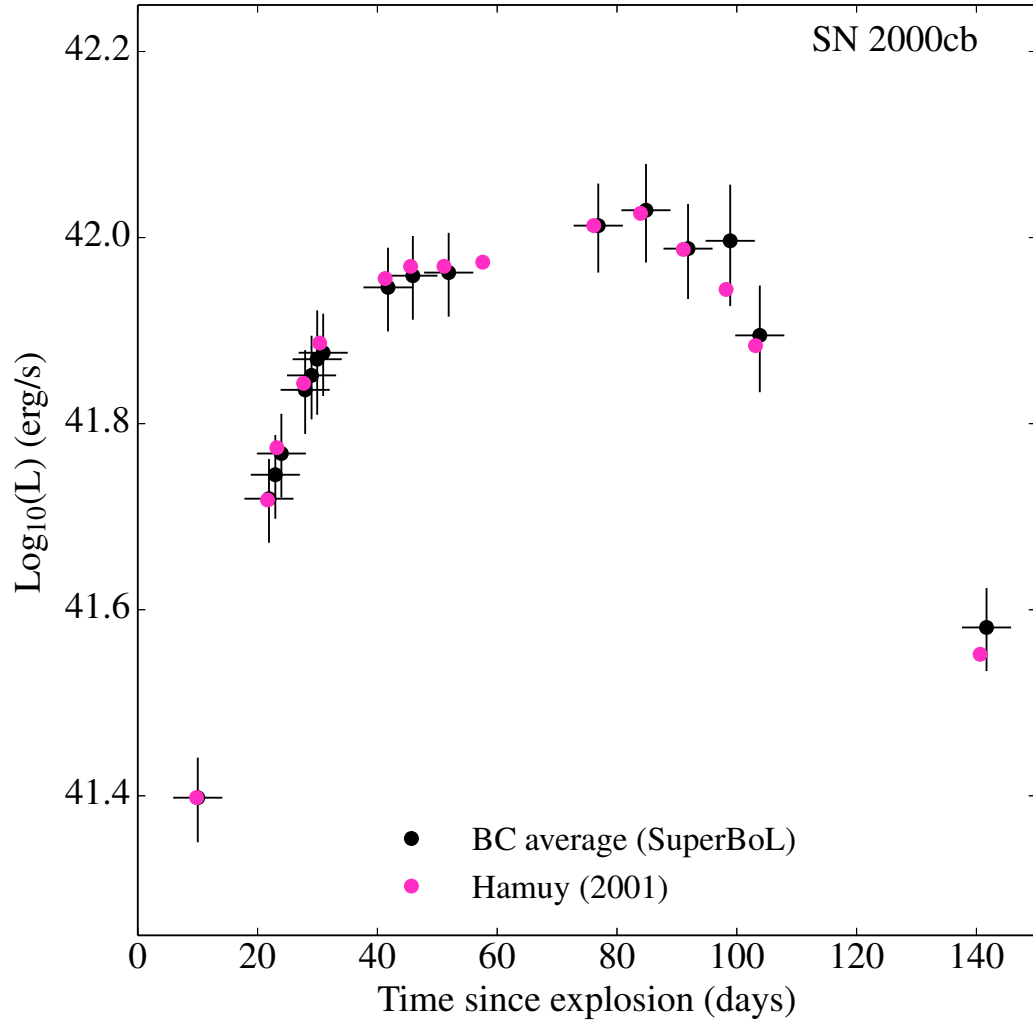


Figure 3.6 Reproducing the bolometric lightcurve of SN 2000cb published by Hamuy (2001) using the bolometric correction technique from the same source. The distance error has been suppressed for clarity, and because both lightcurves assume the same distance.

Chapter 4

Bolometric Luminosities of Peculiar Type II P Supernovae

4.1 Supernova Parameters

In order to compare the bolometric lightcurves produced by **SuperBoL** with those published elsewhere in the literature, we have adopted the same explosion dates, extinction estimates, and distances used in previous studies of each supernova listed in chapter 2. The adopted parameters are listed in Table 4.1, along with references to the sources of those parameters in the literature.

Due to this choice, the bolometric lightcurves of our objects are not calculated using a consistent distance scale. Inter-comparisons between objects must be made with this in mind, since some of the distances from the literature are estimated from redshifts using values of H_0 which vary from $H_0 = 73.8 \pm 2.4 \text{ km s}^{-1} \text{ Mpc}^{-1}$ in the cases of SN 2006V and SN 2006au (section 2.3 and section 2.4) to $H_0 = 65 \text{ km s}^{-1} \text{ Mpc}^{-1}$ in the case of SN 1998A (section 2.1).

4.2 Lightcurves

The bolometric lightcurves produced by **SuperBoL** reveal the large variation in luminosities which results from the different techniques used in the literature. Unsurprisingly, the quasi-bolometric technique results in systematically lower

Table 4.1. Adopted SN parameters from the literature

SN	D (Mpc)	Explosion (JD)	$A_V(\text{total})$	Ref
1998A	30 ± 7	2450801 ± 4	0.399	^a
2000cb	30 ± 7	2451656 ± 4	0.373	^b
2006V	73 ± 5	2453748 ± 4	0.09	^c
2006au	46 ± 3	2453794 ± 9	0.97	^c
2009E	30 ± 2	2454833 ± 3	0.124	^d

References. — ^aPastorello et al., 2005, ^bKleiser et al., 2011, ^cTaddia et al., 2012, ^dPastorello et al., 2012

luminosities than any of the other methods. The quasi-bolometric technique is also dependent upon the number of filters used in the calculation, since no corrections are made for the unobserved flux which falls outside the wavelength range of the filters used. The results of the direct integration and bolometric correction methods agree in most cases with previously published lightcurves in the literature, with the direct integration technique producing systematically higher luminosities in the cases of SN 1998A, SN 2006V, and SN 2006au. Our results also show the high degree of uncertainty in luminosity calculations, typically in the range of $\pm 15\%$ for supernovae with low uncertainties in their distances to $\pm 50\%$ for supernovae with significant distance uncertainties.

The lightcurves shown in Figures 4.1 – 4.5 include the absolute errors calculated by **SuperBoL**, with an upper error of $\log(L + \delta L)$ and a lower error of $\log(L - \delta L)$. This results in asymmetric error-bars on the plot, since we have adopted the common practice of plotting the logarithm of the luminosity and therefore distances

along the y -axis are no longer linear.

Some of the previously published lightcurves include symmetric error-bars, while still plotting the logarithm of the luminosity. This is commonly accomplished by plotting the *relative* error, given by (see, for example, Baird, 1995)

$$\delta z = \delta[\log(y)] \approx d[\log(y)] = \frac{1}{\ln(10)} \frac{dy}{y} \approx 0.434 \frac{\delta y}{y}. \quad (4.1)$$

However, the approximations made to treat the error as a differential only holds for small errors. The uncertainties in the bolometric luminosities calculated by **SuperBoL** are not small, and so we choose to plot the absolute errors. Full tables of our calculated bolometric luminosities is given in Table 4.2 – Table 4.6

4.2.1 SN 1998A

The bolometric lightcurves of SN 1998A are shown in Figure 4.1. The quasi-bolometric luminosities published by Pastorello et al., 2005 are included, and are marginally higher than the quasi-bolometric results of **SuperBoL**, but lie within the uncertainties. Both the direct integration and bolometric correction lightcurves produced by **SuperBoL** are brighter than the direct integration lightcurve of SN 1987A published in Bersten and Hamuy, 2009. The uncertainties in the direct integration lightcurve of SN 1998A are $\delta L_D \approx 0.5 L_D$ while the uncertainties in the bolometric correction lightcurve are $\delta L_{BC} \approx 0.4 L_{BC}$. The large uncertainties in the luminosities are due mainly to the uncertainty in the published distance to SN 1998A (Pastorello et al., 2005) shown in Table 4.1.

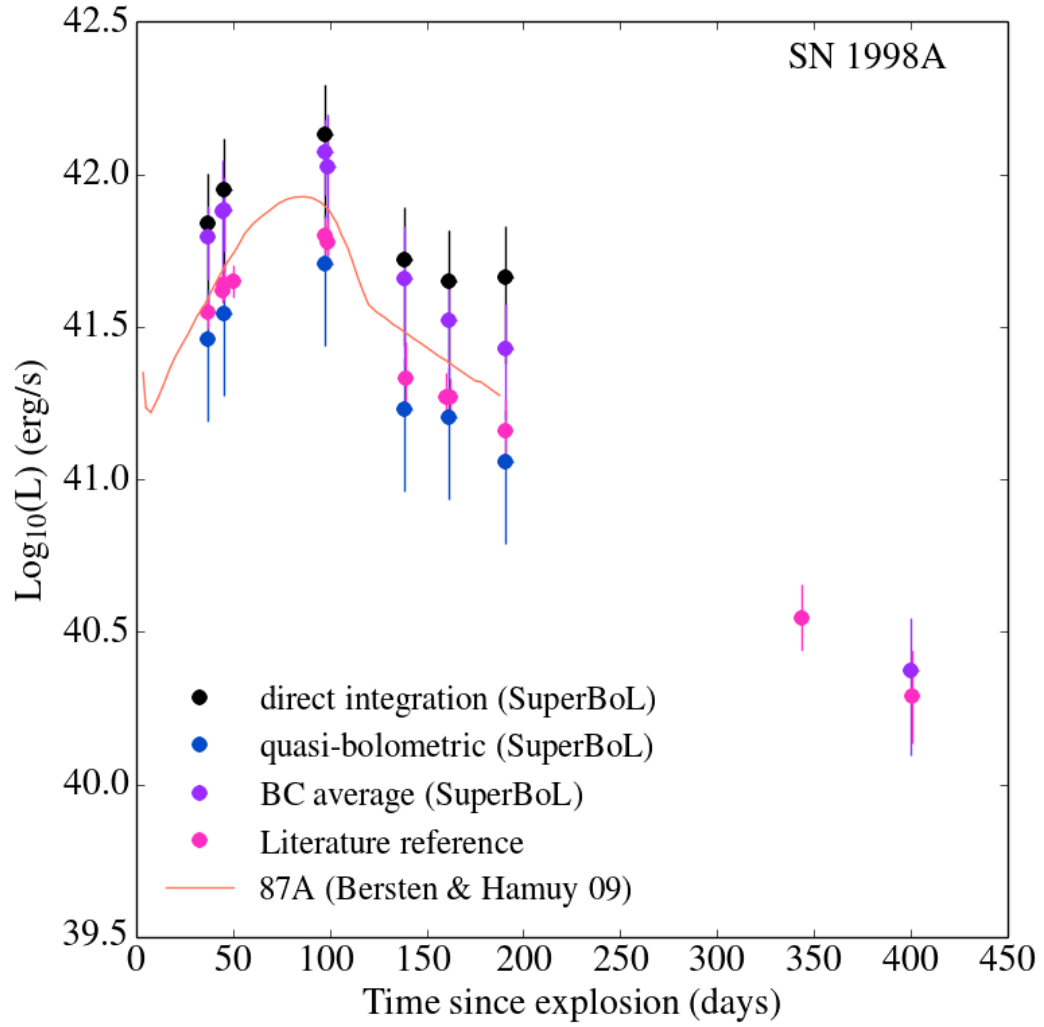


Figure 4.1 Bolometric lightcurves of SN 1998A. The previously published lightcurve is that of Pastorello et al., 2005, described in section 2.1

Table 4.2. Bolometric Lightcurves of SN 1998A

JD	Phase (days)	L_{qbol} 10^{41} (erg/s)	L_{D} 10^{41} (erg/s)	L_{BC} 10^{41} (erg/s)	L_{lit} 10^{41} (erg/s)
2450837.8	37 ± 4	2.9 ± 1.3	7 ± 3	6.2 ± 1.7	$3.6 \pm 0.4^{\text{a}}$
2450845.9	45 ± 4	8 ± 4	$4.2 \pm 0.4^{\text{a}}$
2450846.7	46 ± 4	3.5 ± 1.6	9 ± 4	8 ± 2	$4.4 \pm 0.8^{\text{a}}$
...	50 ± 4	$4.5 \pm 0.6^{\text{a}}$
2450898.5	98 ± 4	5 ± 2	13 ± 6	12 ± 3	$6.3 \pm 1.0^{\text{a}}$
2450899.8	99 ± 4	11 ± 5	$6.0 \pm 1.2^{\text{a}}$
2450939.6	139 ± 4	1.7 ± 0.8	5 ± 3	5 ± 2	$2.1 \pm 0.7^{\text{a}}$
2450960.5	160 ± 4	$1.9 \pm 0.4^{\text{a}}$
2450962.5	162 ± 4	1.6 ± 0.7	4 ± 2	3.3 ± 1.2	$1.9 \pm 0.3^{\text{a}}$
2450991.5	190 ± 4	1.1 ± 0.5	5 ± 2	2.7 ± 1.1	$1.4 \pm 0.4^{\text{a}}$
2451143.8	344 ± 4	$0.35 \pm 0.10^{\text{a}}$
2451200.7	400 ± 4	0.23 ± 0.11	$0.19 \pm 0.09^{\text{a}}$

References. — ^aPastorello et al., 2005

4.2.2 SN 2000cb

In the case of SN 2000cb, there is more available photometry in the literature, taken from Hamuy (2001) and Kleiser et al. (2011). There is also a previously published lightcurve using an early version of the bolometric correction technique, published in Hamuy (2001). Our results are similar to those of SN 1998A, with the quasi-bolometric luminosity lower than the direct integration and bolometric correction lightcurves, which are in close agreement with one another. The lightcurves of SN 2000cb are shown in Figure 4.2. In this supernova, we see that the older version of the bolometric correction technique produces luminosities very similar to those derived from the **SuperBoL** routine. The uncertainties are

Table 4.3. Bolometric Lightcurves of SN 2000cb

JD	Phase (days)	L_{qbol} 10^{41} (erg/s)	L_D 10^{41} (erg/s)	L_{BC} 10^{41} (erg/s)	L_{lit} 10^{41} (erg/s)
2451663.81	8 ± 4	1.1 ± 0.5	2.1 ± 0.9	2.0 ± 0.6	2.5^{b}
2451663.92	8 ± 4	2.4 ± 0.7	... ^c
2451667.86	12 ± 4	2.6 ± 0.7	... ^c
2451675.70	20 ± 4	2.1 ± 1.0	5 ± 2	4.5 ± 1.2	5.2^{b}
2451676.76	21 ± 4	2.3 ± 1.1	5 ± 3	4.8 ± 1.3	... ^b
2451677.77	22 ± 4	2.4 ± 1.1	6 ± 3	5.1 ± 1.4	5.9^{b}
2451681.74	26 ± 4	2.8 ± 1.3	7 ± 3	6.0 ± 1.6	... ^b
2451682.81	27 ± 4	3.0 ± 1.4	7 ± 3	6.2 ± 1.7	7.0^{b}
2451683.75	28 ± 4	6 ± 3	... ^b
2451683.78	28 ± 4	3.1 ± 1.4	7 ± 3	6.4 ± 1.8	... ^b
2451684.75	29 ± 4	3.3 ± 1.5	7 ± 3	7 ± 3	7.7^{b}
2451692.88	37 ± 4	8 ± 2	... ^c
2451695.57	40 ± 4	3.7 ± 1.7	9 ± 4	8 ± 2	9.0^{b}
2451696.87	44 ± 4	8 ± 2	... ^c
2451699.72	44 ± 4	3.8 ± 1.8	10 ± 5	9 ± 2	9.3^{b}
2451700.85	45 ± 4	9 ± 2	... ^c

also large, owing to the uncertainty in supernova distance as published in Kleiser et al. (2011). The direct integration technique has uncertainties of $\delta L_D \approx 0.5 L_D$, and the bolometric correction technique has uncertainties of $\delta L_{BC} \approx 0.3 L_{BC}$.

Table 4.3 (cont'd)

JD	Phase (days)	L_{qbol} 10^{41} (erg/s)	L_{D} 10^{41} (erg/s)	L_{BC} 10^{41} (erg/s)	L_{lit} 10^{41} (erg/s)
2451705.70	50 ± 4	3.8 ± 1.8	10 ± 5	9 ± 2	9.3^{b}
2451706.85	51 ± 4	9 ± 2	... ^c
2451713.82	58 ± 4	9 ± 3	... ^c
2451717.84	62 ± 4	10 ± 3	... ^c
2451721.82	66 ± 4	11 ± 3	... ^c
2451728.77	73 ± 4	11 ± 3	... ^c
2451730.67	75 ± 4	3.9 ± 1.8	12 ± 6	11 ± 3	10.3^{b}
2451735.72	80 ± 4	10 ± 3	... ^c
2451738.64	83 ± 4	3.8 ± 1.8	12 ± 5	12 ± 3	10.6^{b}
2451742.73	87 ± 4	12 ± 4	... ^c
2451745.66	90 ± 4	3.5 ± 1.6	11 ± 5	11 ± 3	9.7^{b}
2451749.69	94 ± 4	11 ± 3	... ^c
2451752.70	97 ± 4	9 ± 5	... ^c
2451756.69	101 ± 4	8 ± 3	... ^c
2451757.64	102 ± 4	2.5 ± 1.2	9 ± 4	10 ± 3	7.7^{b}
2451781.66	126 ± 4	3.9 ± 1.6	... ^c

Table 4.3 (cont’d)

JD	Phase (days)	L_{qbol} 10^{41} (erg/s)	L_{D} 10^{41} (erg/s)	L_{BC} 10^{41} (erg/s)	L_{lit} 10^{41} (erg/s)
2451788.66	133 ± 4	1.9 ± 1.0	... ^c
2451795.49	140 ± 4	1.2 ± 0.6	4.1 ± 1.9	12 ± 7	3.7^{b}
2451795.64	140 ± 4	2.3 ± 0.9	... ^c

References. — ^bHamuy, 2001, ^cKleiser et al., 2011

Note. — The reported photometry of SN 2000cb in Kleiser et al. (2011) did not include the needed 4 photometric filters for **SuperBoL** to calculate the quasi-bolometric and direct integration luminosities.

4.2.3 SNe 2006V and 2006au

Our lightcurves for Supernovae SN 2006V and SN 2006au are shown in Figure 4.3 and Figure 4.4, respectively. The closest match to previously published results from Taddia et al. (2012) is made by the bolometric correction technique, as the direct integration technique produces luminosities systematically higher for both supernovae. The primary difference between the direct integration technique used by **SuperBoL** and the method used by Taddia et al. (2012) is the interpolation scheme used to integrate between the observed fluxes. **SuperBoL** uses a linear interpolation, while the previously published lightcurve uses a cubic spline interpolation as discussed in subsection 1.3.1.

Immediately apparent when comparing our lightcurves of the two supernovae is the apparent “noise” in the lightcurve of SN 2006au. This is because of missing observations in the photometric dataset published by Taddia et al. (2012).

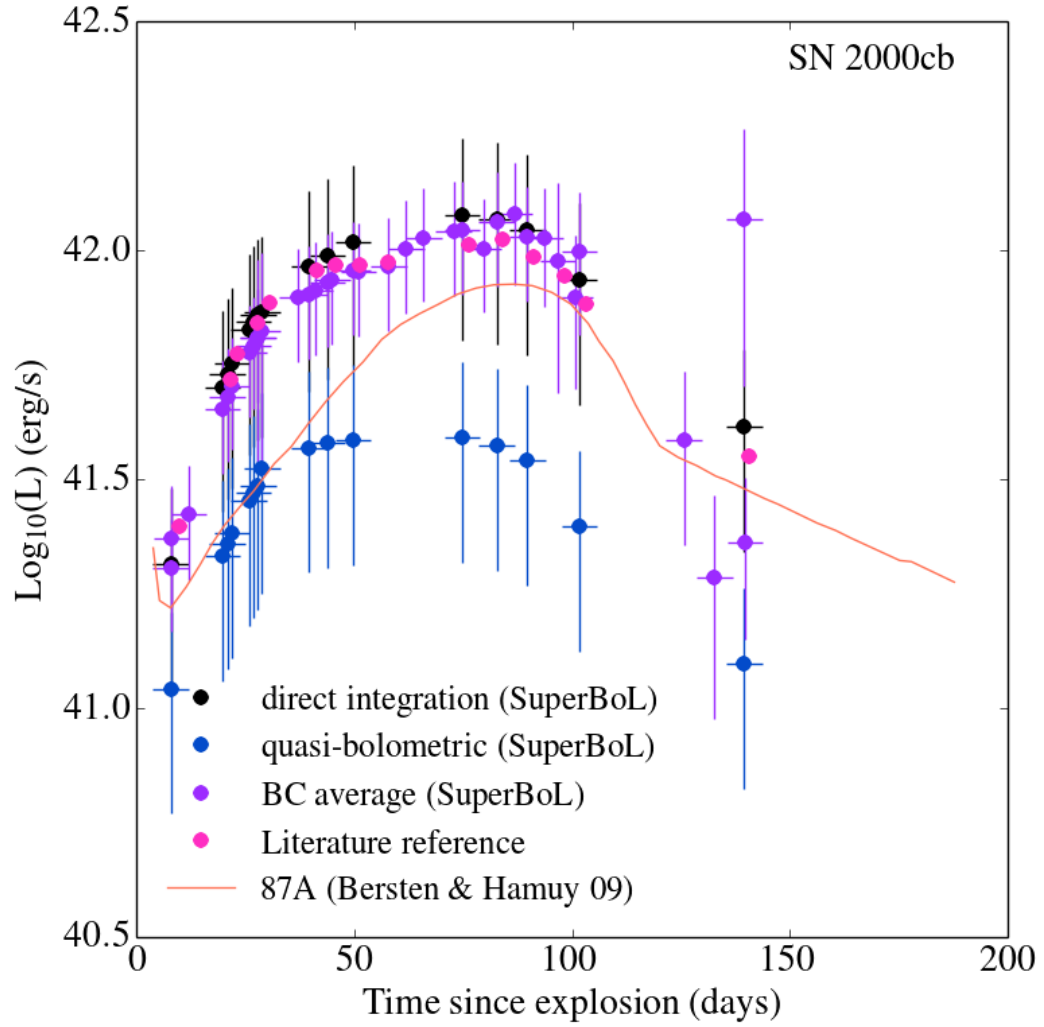


Figure 4.2 Bolometric lightcurves of SN 2000cb. The previously published lightcurve is that of Hamuy, 2001, described in section 2.2

SuperBoL currently makes no attempt to interpolate missing magnitudes in a dataset using observed magnitudes from previous or subsequent nights. As a result, the quasi-bolometric flux on a night with a missing bandpass will be lower than the flux on nights with more complete data. This has an effect on both the quasi-bolometric and the direct integration luminosities.

For both of these supernovae, the bolometric correction lightcurve is calculated using only $B - V$, since the Carnegie Supernova Project uses the filter set *ugriBV*, and the bolometric correction method as implemented in **SuperBoL** relies on $B - V$, $V - I$ and $B - I$ colors. Because of the relatively small uncertainties in the published distances to these supernovae given in Taddia et al., 2012, the error-bars on our calculated lightcurves for SN 2006V and SN 2006au are among the smallest in our sample. For SN 2006V, the direct integration technique has uncertainties of $\delta L_D \approx 0.14 L_D$, and the bolometric correction technique has uncertainties of $\delta L_{BC} \approx 0.17 L_{BC}$. For SN 2006au, the direct integration technique has uncertainties equal to those of SN 2006V, with bolometric correction technique uncertainties of $\delta L_{BC} \approx 0.2 L_{BC}$.

Table 4.4. Bolometric Lightcurves of SN 2006V

JD	Phase (days)	L_{qbol} 10^{41} (erg/s)	L_{D} 10^{41} (erg/s)	L_{BC} 10^{41} (erg/s)	L_{lit} 10^{41} (erg/s)
2453773.71	26 ± 4	3.8 ± 0.5	8.9 ± 1.2	7.1 ± 1.2	$7.5 \pm 0.3^{\text{d}}$
2453774.82	27 ± 4	4.0 ± 0.5	9.3 ± 1.3	7.4 ± 1.3	$7.8 \pm 0.3^{\text{d}}$
2453775.67	28 ± 4	4.1 ± 0.6	9.6 ± 1.3	7.7 ± 1.3	$8.1 \pm 0.3^{\text{d}}$
2453778.81	31 ± 4	4.6 ± 0.6	10.6 ± 1.5	8.7 ± 1.5	$9.0 \pm 0.3^{\text{d}}$
2453784.90	37 ± 4	10.2 ± 1.8	... ^d
2453786.88	39 ± 4	5.8 ± 0.8	13.1 ± 1.8	10.8 ± 1.9	$10.9 \pm 0.2^{\text{d}}$
2453795.84	48 ± 4	6.2 ± 0.8	16 ± 2	13 ± 2	$12.9 \pm 0.3^{\text{d}}$
2453799.75	52 ± 4	6.7 ± 0.9	17 ± 2	14 ± 2	$13.8 \pm 0.4^{\text{d}}$
2453804.84	57 ± 4	7.2 ± 1.0	19 ± 3	15 ± 3	... ^d
2453805.79	58 ± 4	7.3 ± 1.0	19 ± 3	15 ± 3	$15.3 \pm 0.4^{\text{d}}$
2453818.77	71 ± 4	8.3 ± 1.1	22 ± 3	17 ± 3	$17.7 \pm 0.4^{\text{d}}$
2453824.73	77 ± 4	8.5 ± 1.2	22 ± 3	18 ± 3	$18.2 \pm 0.4^{\text{d}}$
2453832.75	85 ± 4	8.2 ± 1.1	22 ± 3	17 ± 3	$17.7 \pm 0.4^{\text{d}}$
2453838.75	91 ± 4	7.6 ± 1.0	20 ± 3	16 ± 3	$16.4 \pm 0.4^{\text{d}}$
2453846.73	99 ± 4	6.0 ± 0.8	17 ± 2	12 ± 2	$13.4 \pm 0.3^{\text{d}}$
2453853.64	106 ± 4	4.1 ± 0.6	12.5 ± 1.7	8.2 ± 1.4	$10.0 \pm 0.3^{\text{d}}$

Table 4.4 (cont'd)

JD	Phase (days)	L_{qbol} 10^{41} (erg/s)	L_{D} 10^{41} (erg/s)	L_{BC} 10^{41} (erg/s)	L_{lit} 10^{41} (erg/s)
2453862.57	115 ± 4	2.8 ± 0.4	9.0 ± 1.2	5.4 ± 0.9	$7.2 \pm 0.3^{\text{d}}$
2453867.57	120 ± 4	2.6 ± 0.4	8.0 ± 1.1	5.5 ± 1.1	$6.5 \pm 0.3^{\text{d}}$
2453892.56	145 ± 4	1.8 ± 0.3	6.4 ± 0.9	...	$5.0 \pm 0.3^{\text{d}}$
2453898.56	151 ± 4	1.8 ± 0.3	6.4 ± 0.9	3.3 ± 0.6	$4.5 \pm 0.2^{\text{d}}$

References. — ^dTaddia et al., 2012

Table 4.5. Bolometric Lightcurves of SN 2006au

JD	Phase (days)	L_{qbol} 10^{41} (erg/s)	L_{D} 10^{41} (erg/s)	L_{BC} 10^{41} (erg/s)	L_{lit} 10^{41} (erg/s)
2453805.89	12 ± 9	5.5 ± 0.8	13.9 ± 1.9	9.2 ± 1.6	$10.4 \pm 0.5^{\text{d}}$
2453809.85	16 ± 9	4.7 ± 0.7	12.5 ± 1.7	9.6 ± 1.7	$9.6 \pm 0.4^{\text{d}}$
2453815.86	22 ± 9	4.9 ± 0.7	12.6 ± 1.8	8.7 ± 1.5	$9.2 \pm 0.4^{\text{d}}$
2453818.90	25 ± 9	5.0 ± 0.7	12.2 ± 1.7	8.5 ± 1.5	$9.3 \pm 0.3^{\text{d}}$
2453819.90	26 ± 9	3.3 ± 0.5	15 ± 2	8.7 ± 1.5	$9.4 \pm 0.7^{\text{d}}$
2453823.83	30 ± 9	5.2 ± 0.7	12.0 ± 1.7	8.6 ± 1.5	$9.4 \pm 0.4^{\text{d}}$
2453824.87	31 ± 9	5.3 ± 0.7	12.3 ± 1.7	8.9 ± 1.5	$9.5 \pm 0.4^{\text{d}}$
2453828.89	35 ± 9	2.4 ± 0.3	16 ± 2	9.6 ± 1.6	$10.1 \pm 0.8^{\text{d}}$
2453829.92	$10.0 \pm 1.2^{\text{d}}$
2453830.89	37 ± 9	5.5 ± 0.8	12.7 ± 1.8	8.7 ± 1.5	$9.9 \pm 0.7^{\text{d}}$
2453831.83	38 ± 9	5.8 ± 0.8	12.6 ± 1.8	...	$10.1 \pm 0.7^{\text{d}}$
2453832.86	39 ± 9	2.4 ± 0.3	14 ± 2	9.5 ± 1.6	$10.3 \pm 0.8^{\text{d}}$
2453835.87	42 ± 9	5.9 ± 0.8	13.2 ± 1.8	9.8 ± 1.7	$10.8 \pm 0.4^{\text{d}}$
2453838.82	45 ± 9	6.7 ± 0.9	15 ± 2	11.2 ± 1.9	$12.0 \pm 0.8^{\text{d}}$
2453840.83	47 ± 9	6.7 ± 0.9	15 ± 2	11 ± 2	$11.9 \pm 0.6^{\text{d}}$
2453841.85	48 ± 9	6.9 ± 1.0	15 ± 2	12 ± 2	$12.1 \pm 0.5^{\text{d}}$

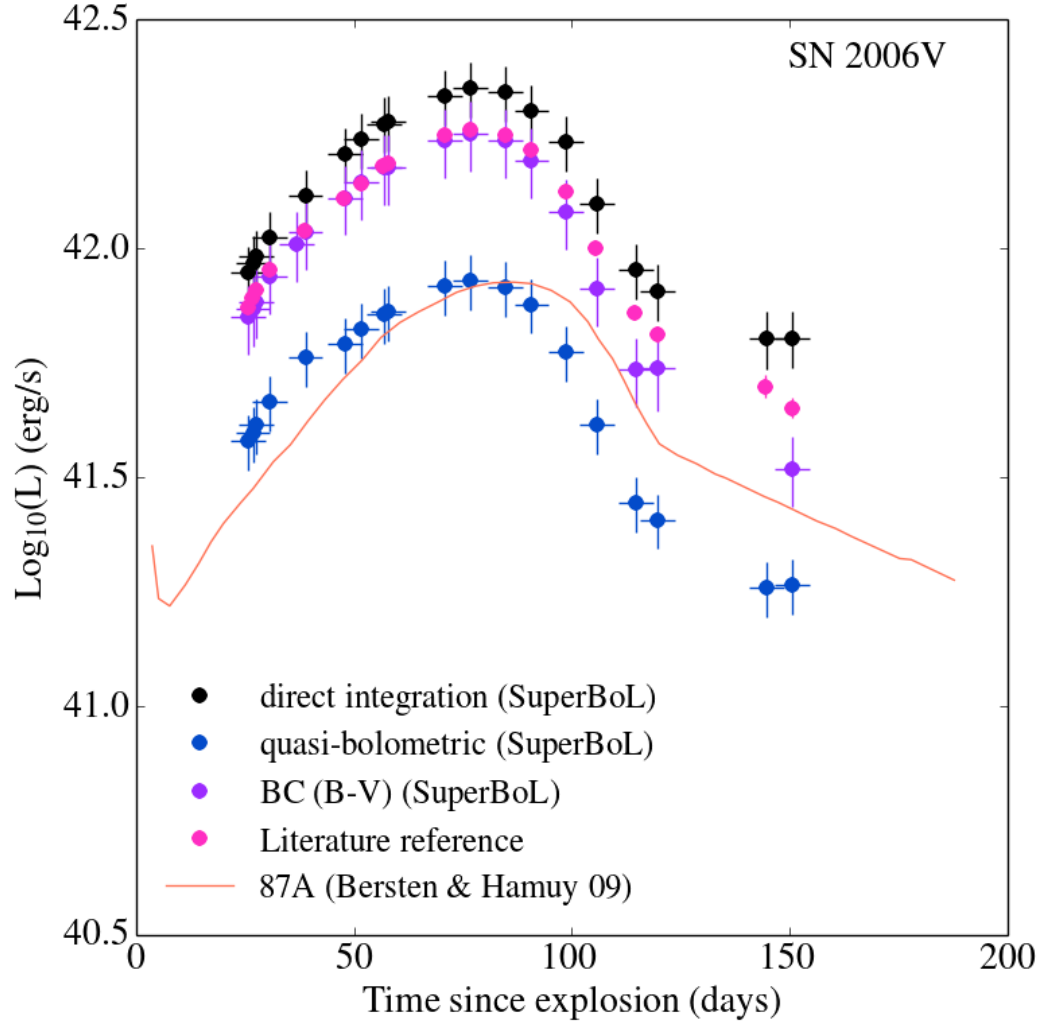


Figure 4.3 Bolometric lightcurves of SN 2006V. The previously published lightcurve is that of Taddia et al., 2012, described in section 2.3

Table 4.5 (cont'd)

JD	Phase (days)	L_{qbol} 10^{41} (erg/s)	L_{D} 10^{41} (erg/s)	L_{BC} 10^{41} (erg/s)	L_{lit} 10^{41} (erg/s)
2453845.82	52 ± 9	6.3 ± 0.9	17 ± 2	12 ± 2	$13.0 \pm 0.7^{\text{d}}$
2453850.81	57 ± 9	6.6 ± 0.9	18 ± 2	13 ± 2	$13.6 \pm 0.7^{\text{d}}$
2453853.85	60 ± 9	6.7 ± 0.9	18 ± 2	13 ± 2	$14.0 \pm 0.8^{\text{d}}$
2453858.79	65 ± 9	7.4 ± 0.9	21 ± 3	14 ± 3	$14.9 \pm 0.8^{\text{d}}$
2453861.82	68 ± 9	7.2 ± 1.0	20 ± 3	14 ± 2	$15.2 \pm 0.8^{\text{d}}$
2453862.80	69 ± 9	4.5 ± 1.0	22 ± 3	14 ± 3	$15.6 \pm 1.2^{\text{d}}$
2453866.75	73 ± 9	7.7 ± 0.6	20 ± 3	15 ± 3	$16.0 \pm 0.9^{\text{d}}$
2453867.78	74 ± 9	7.6 ± 1.1	21 ± 3	15 ± 3	$15.7 \pm 1.0^{\text{d}}$
2453870.80	77 ± 9	7.6 ± 1.1	21 ± 3	15 ± 3	$16.2 \pm 0.9^{\text{d}}$
2453871.79	78 ± 9	7.5 ± 1.0	21 ± 3	15 ± 3	$15.8 \pm 0.8^{\text{d}}$
2453872.78	79 ± 9	7.4 ± 1.0	21 ± 3	14 ± 2	$15.7 \pm 1.0^{\text{d}}$
2453886.78	93 ± 9	8.9 ± 1.6	$11.5 \pm 1.0^{\text{d}}$
2453890.72	97 ± 9	4.5 ± 0.6	13.3 ± 1.9	8.2 ± 1.9	$9.7 \pm 0.7^{\text{d}}$
2453891.74	98 ± 9	4.2 ± 0.6	14 ± 2	7.7 ± 1.3	$9.2 \pm 0.5^{\text{d}}$
2453892.76	99 ± 9	4.0 ± 0.5	15 ± 2	7.7 ± 1.4	$9.4 \pm 0.5^{\text{d}}$
2453893.71	100 ± 9	4.1 ± 0.7	16 ± 2	7.2 ± 1.2	$8.5 \pm 0.5^{\text{d}}$

Table 4.5 (cont’d)

JD	Phase (days)	L_{qbol} 10^{41} (erg/s)	L_{D} 10^{41} (erg/s)	L_{BC} 10^{41} (erg/s)	L_{lit} 10^{41} (erg/s)
2453894.75	101 ± 9	3.6 ± 0.5	11.9 ± 1.7	6.9 ± 1.2	$7.6 \pm 0.4^{\text{d}}$
2453897.66	104 ± 9	4.5 ± 0.9	$5.3 \pm 0.6^{\text{d}}$
2453898.71	105 ± 9	$4.0 \pm 0.5^{\text{d}}$

References. — ^dTaddia et al., 2012

4.2.4 SN 2009E

The lightcurves of SN 2009E calculated with **SuperBoL** are shown along with the previously published lightcurve from Pastorello et al. (2012) in Figure 4.5. This object was extensively monitored by amateur astronomers during its evolution, resulting in a lightcurve very well-sampled in time (see Pastorello et al., 2012, §2.3). Most of the images were captured unfiltered — so although there is abundant photometry available, the limited use of bandpasses means that the number of days on which enough filters were available to re-construct a quasi-bolometric flux are few. The small uncertainties in the lightcurves ($\delta L_{\text{D}} \approx 0.19 L_{\text{D}}$ and $\delta L_{\text{BC}} \approx 0.2 L_{\text{BC}}$) are again due to the small published uncertainty in the distance to the object.

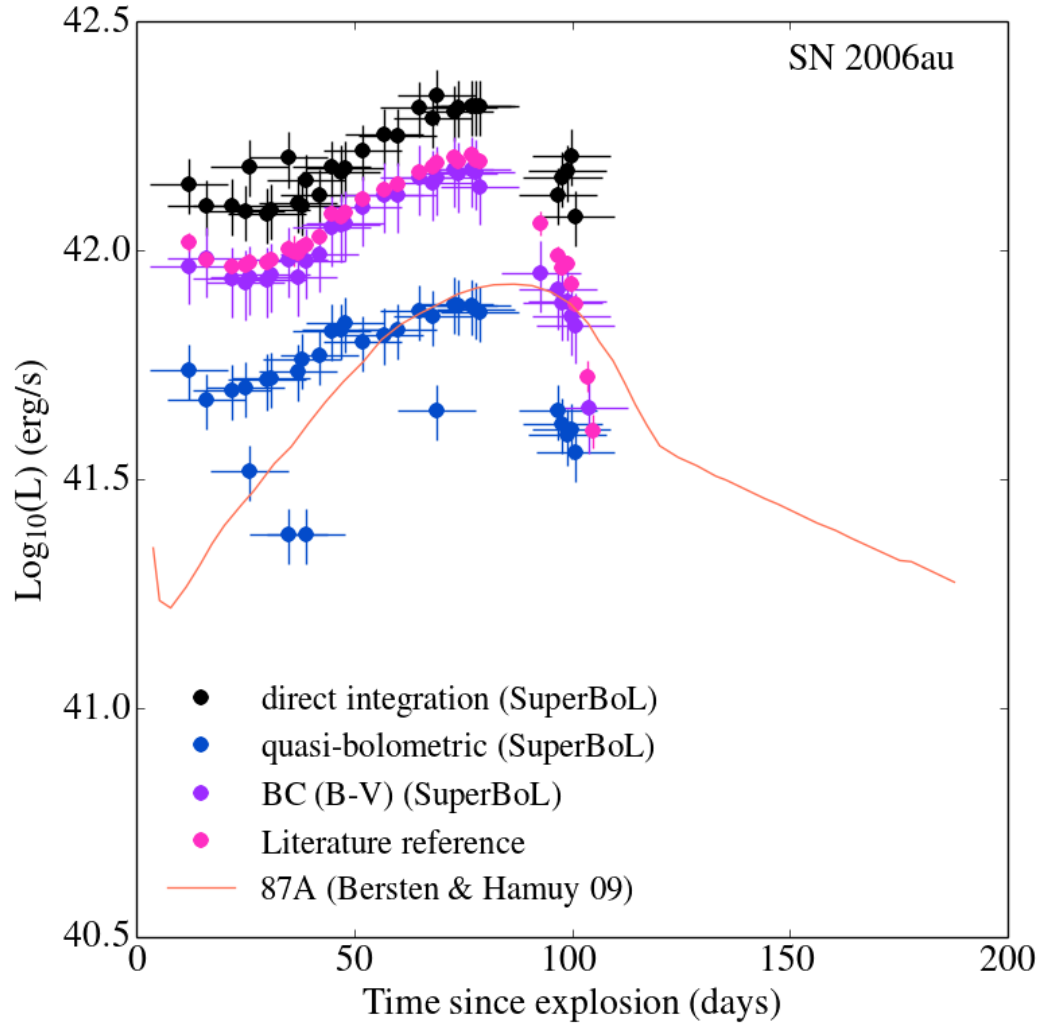


Figure 4.4 Bolometric lightcurves of SN 2006au. The previously published lightcurve is that of Taddia et al., 2012, described in section 2.4

Table 4.6. Bolometric Lightcurves of SN 2009E

JD	Phase (days)	L_{qbol} 10^{41} (erg/s)	L_{D} 10^{41} (erg/s)	L_{BC} 10^{41} (erg/s)	L_{lit} 10^{41} (erg/s)
2454840.84	1.7 ^e
2454858.01	26 ± 9	1.1 ± 0.16	2.6 ± 0.5	2.6 ± 0.3	2.6 ^e
2454915.41	83 ± 9	2.5 ± 0.3	6.1 ± 0.9	5.6 ± 0.6	6.2 ^e
2454917.33	85 ± 9	6.3 ± 1.8	6.4 ^e
2454922.49	90 ± 9	2.5 ± 0.3	6.3 ± 0.9	5.7 ± 0.6	6.2 ^e
2454923.34	91 ± 9	6.2 ^e
2454926.42	94 ± 9	6.3 ^e
2454928.33	96 ± 9	6.5 ± 1.2	6.4 ^e
2454934.39	102 ± 9	6.3 ± 1.1	6.4 ^e
2454934.46	102 ± 9	2.7 ± 0.4	7.5 ± 1.1	5.8 ± 0.6	6.4 ^e
2452938.41	106 ± 9	6.3 ± 1.1	6.4 ^e
2454938.53	106 ± 9	2.4 ± 0.3	6.2 ± 0.9	5.6 ± 0.6	6.3 ^e
2454944.38	112 ± 9	2.1 ± 0.3	5.8 ± 1.2	5.8 ± 1.4	5.6 ^e
2454946.40	114 ± 9	5.1 ± 1.0	5.0 ^e
2454955.45	123 ± 9	1.04 ± 0.15	3.2 ± 0.5	3.5 ± 0.9	3.0 ^e
2454955.53	123 ± 9	1.07 ± 0.15	3.3 ± 0.5	3.4 ± 0.5	2.9 ^e

Table 4.6 (cont'd)

JD	Phase (days)	L_{qbol} 10^{41} (erg/s)	L_{D} 10^{41} (erg/s)	L_{BC} 10^{41} (erg/s)	L_{lit} 10^{41} (erg/s)
2454957.42	125 ± 9	2.6 ^e
2454964.66	132 ± 9	0.72 ± 0.10	2.4 ± 0.4	2.6 ± 0.8	2.0 ^e
2454971.52	139 ± 9	0.63 ± 0.09	2.2 ± 0.3	2.8 ± 0.8	1.8 ^e
2454979.37	147 ± 9	1.7 ^e
2454982.59	150 ± 9	0.59 ± 0.09	2.0 ± 0.4	2.1 ± 1.4	1.7 ^e
2455009.38	177 ± 9	1.2 ^e
2455031.39	199 ± 9	0.97 ^e
2455042.36	210 ± 9	0.90 ^e
2455056.35	224 ± 9	0.29 ± 0.04	1.0 ± 0.2	0.6 ± 0.2	0.77 ^e
2455063.37	231 ± 9	0.72 ^e
2455072.34	240 ± 9	0.25 ± 0.04	0.8 ± 0.2	0.49 ± 0.18	0.64 ^e
2455079.34	247 ± 9	0.24 ± 0.04	0.8 ± 0.2	0.48 ± 0.14	0.63 ^e
2455154.69	322 ± 9	0.34 ^e
2455285.43	453 ± 9	0.042 ± 0.008	0.09 ± 0.03	0.079 ± 0.019	... ^e

References. — ^ePastorello et al., 2012

4.3 Nickel Mass Estimates

The post-plateau luminosity of a Type II P supernova comes primarily from energy deposited by the gamma-rays produced in the decay chain $^{56}\text{Ni} \rightarrow ^{56}\text{Co} \rightarrow ^{56}\text{Fe}$.

We use the γ -ray specific energy for pure ^{56}Ni from Sutherland and Wheeler, 1984:

$$s = 3.90 \times 10^{10} e^{-\gamma_1 t} + 6.78 \times 10^9 (e^{-\gamma_2 t} - e^{\gamma_1 t}) \quad (4.2)$$

where s is in $\text{erg s}^{-1} \text{ g}^{-1}$. The constants $\gamma_1 = 1.32 \times 10^{-6} \text{ s}^{-1}$, and $\gamma_2 = 1.02 \times 10^{-7} \text{ s}^{-1}$ are the decay rates of ^{56}Ni and ^{56}Co , corresponding to half-lives of 6.08 d and 78.65 d, respectively.

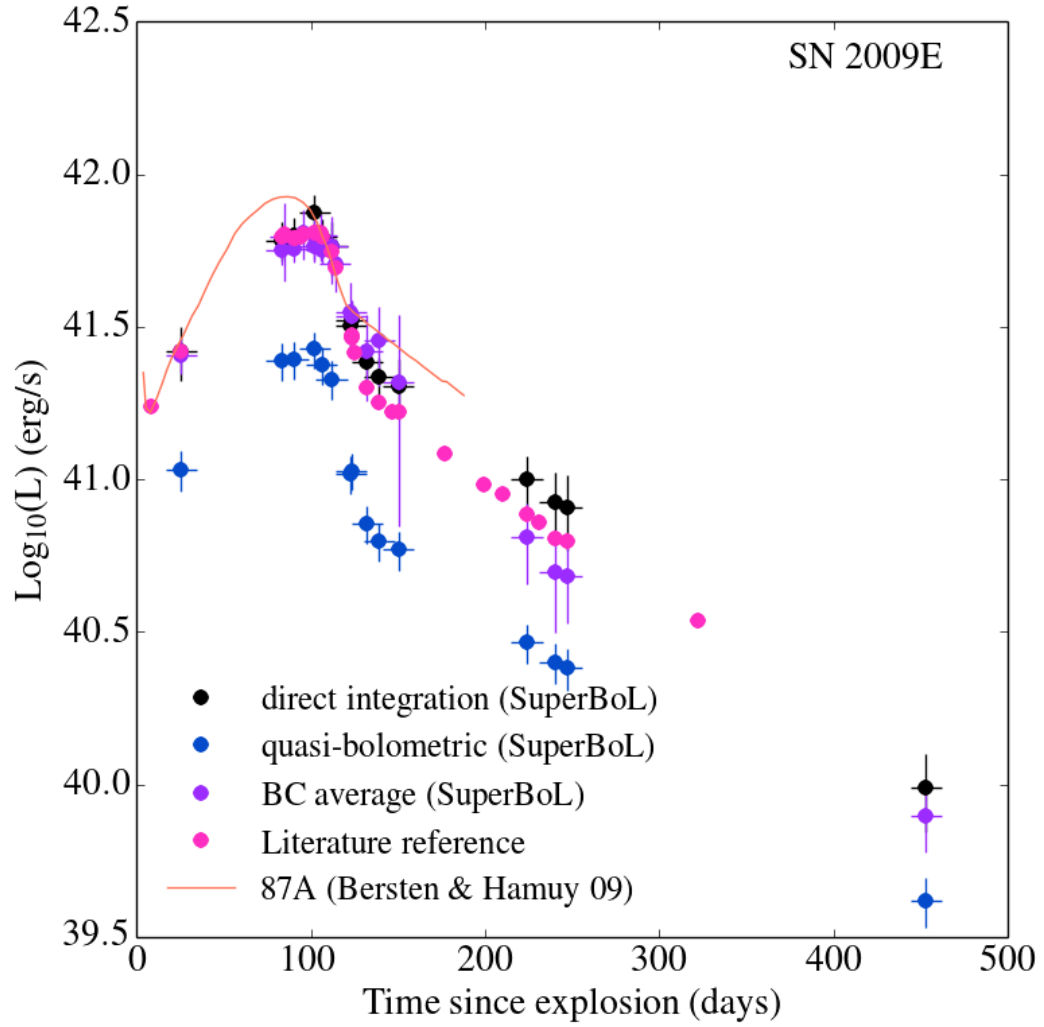


Figure 4.5 Bolometric lightcurves of SN 2009E. The previously published lightcurve is that of Pastorello et al., 2012, described in section 2.5

The nickel mass ejected by the supernova can be estimated by fitting the luminosity of the post-plateau tail with the equation

$$L_{\text{Ni}} = sM_{\text{Ni}} \quad (4.3)$$

In our calculations, we again use the `curve_fit` function from `scipy` to determine the mass of ^{56}Ni ejected by each supernova. We included bolometric lightcurve points between 120 and 350 days post-explosion in our fit. The results of our best-fit ^{56}Ni masses are shown in Table 4.7, with one standard deviation errors determined by calculating the square root of the variance σ_X^2 output by `curve_fit`. Also shown in Table 4.7 are values for the ejected mass of ^{56}Ni from previously published literature. The results are also shown in Figure 4.6, where the horizontal axis serves to separate the results from the different supernovae. Excluded from our analysis is SN 2006au, which does not include any observations which conclusively fall on the radioactive tail.

The differences between the lightcurves calculated by `SuperBoL` and those previously published in the literature are reflected here in the inferred nickel masses. Where the direct integration technique produced luminosities significantly greater than those in previously published studies (most notably in the cases of SN 1998A and SN 2006V,) the resulting nickel mass was correspondingly higher. Similarly, it is clear that using quasi-bolometric luminosities will result in nickel masses many times smaller than the other techniques analyzed here.

It is encouraging to note that our results for the mass of ^{56}Ni using the

Table 4.7. Ejected ^{56}Ni masses

SN	qbol (M_{\odot})	Direct (M_{\odot})	BC (M_{\odot})	lit (M_{\odot})	Method
1998A	0.046 ± 0.012	0.15 ± 0.04	0.11 ± 0.02	0.11^{a}	D, SA
2000cb	0.032 ± 0.015	0.11 ± 0.05	0.060 ± 0.015	$0.09 \pm 0.037^{\text{b}}$ $0.1 \pm 0.02^{\text{c}}$ $0.083 \pm 0.039^{\text{d}}$	P D, H D, H
2006V	0.050 ± 0.005	0.17 ± 0.017	0.092 ± 0.016	$0.127 \pm 0.010^{\text{e}}$ 0.127^{e}	D D, SA
2006au	—	—	—	$\leq 0.073^{\text{e}}$	D, SA
2009E	0.017 ± 0.001	0.06 ± 0.004	0.048 ± 0.005	0.043^{f} 0.039^{f}	D, H D, SA

References. — ^aPastorello et al., 2005, ^bHamuy, 2001 ^cKleiser et al., 2011, ^dUtrobin and Chugai, 2011, ^eTaddia et al., 2012, ^fPastorello et al., 2012

Note. — Reported uncertainties are one standard deviation errors from the least squares fitting. Two significant figures are reported for uncertainties with a leading digit of 1. For each value of the ^{56}Ni mass from the literature, the method used to calculate it has also been reported. D: L_{bol} from direct integration. P: L_{bol} from polynomial fits. H: $M(^{56}\text{Ni})$ from hydrodynamic models. SA: $M(^{56}\text{Ni})$ from semi-analytic models.

direct integration and bolometric correction techniques broadly agree with those produced by semi-analytic lightcurve models and hydrodynamic models used previously in the literature. In the case of SN 1998A, Pastorello et al. (2005) used the semi-analytic code developed by Zampieri et al. (2003) to produce a best-fit bolometric lightcurve. The ^{56}Ni mass ejected by the supernova is one of the input parameters of the model, along with other progenitor and explosion parameters, outlined in Pastorello et al. (2005) (their Table 5.) Other studies have used the hydrodynamic models of Young (2004) (Kleiser et al., 2011, in the case of SN 2000cb), the semi-analytic models of Imshennik and Popov (1992) (Taddia et al., 2012, in the case of SN 2006V and SN 2006au), and the hydrodynamic models of Pumo et al. (2010) and Pumo and Zampieri (2011) (Pastorello et al., 2012, in the case of SN 2009E)

4.4 Peak Luminosities

Another observationally meaningful parameter is the peak luminosity of a supernova, L_{peak} . We measure L_{peak} as the highest of our bolometric luminosities, and compare that with values taken from the literature in Table 4.8. The first three columns include the uncertainties output by **SuperBoL**, and the last column includes, where possible, uncertainties reported in the literature. We note that the uncertainties in our values for the peak bolometric luminosity are very large compared to those previously published in the literature. The cause of this discrepancy is unclear. Not all published bolometric lightcurves include error-bars, and those that do often lack a detailed description of the uncertainty calculations.

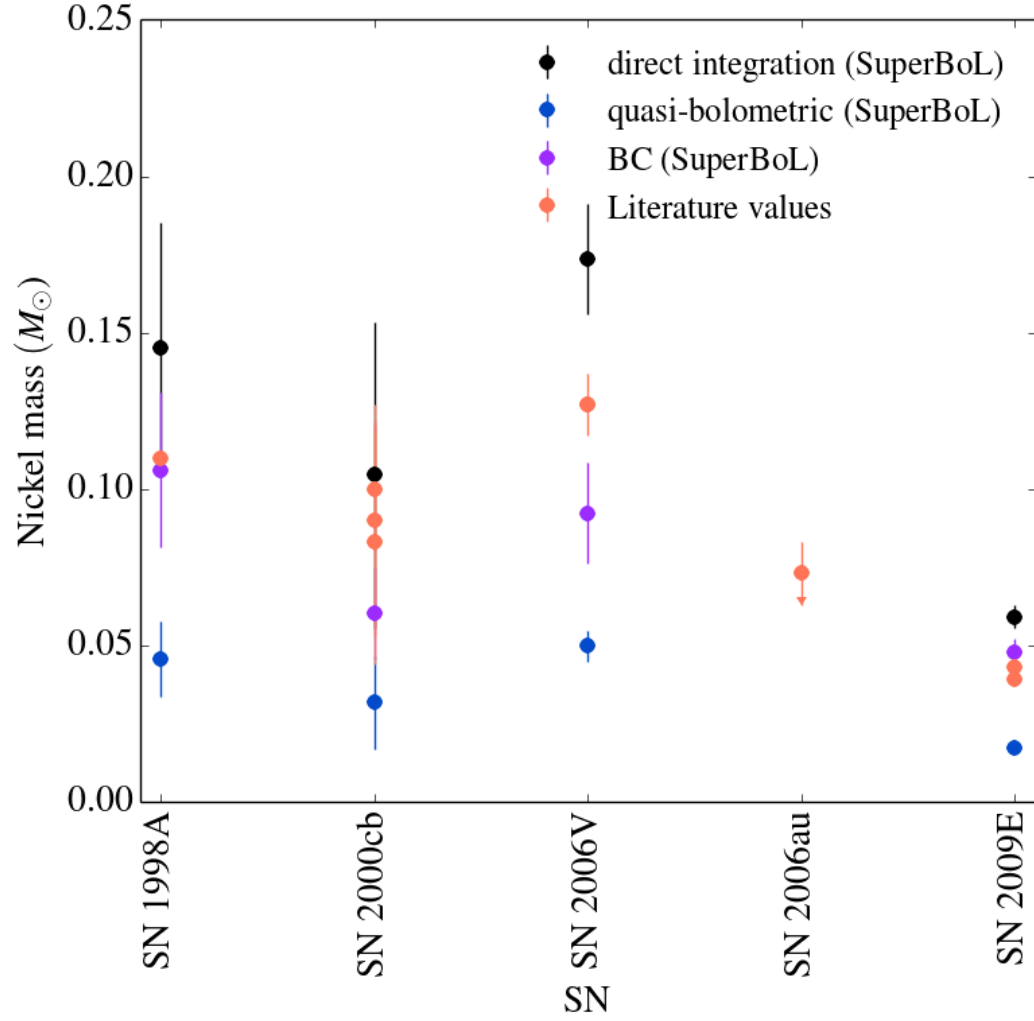


Figure 4.6 Comparison of ejected ^{56}Ni masses generated by **SuperBoL** and those previously published in the literature.

Table 4.8. Peak observed SN luminosities

SN	L_{qbol} 10^{41} (erg/s)	L_{D} 10^{41} (erg/s)	L_{BC} 10^{41} (erg/s)	L_{lit} 10^{41} (erg/s)
1998A	5 ± 2	13 ± 6	12 ± 3	$6.3 \pm 0.8^{\text{a}}$
2000cb	4 ± 1.8	12 ± 6	12 ± 4	9.4^{b}
2006V	8.5 ± 1.2	22 ± 3	18 ± 3	$18.2 \pm 0.4^{\text{c}}$
2006au	7.7 ± 1.1	20 ± 3	15 ± 3	$16.2 \pm 0.6^{\text{c}}$
2009E	2.7 ± 0.4	7.5 ± 1.1	6.5 ± 1.2	6.4^{d}

References. — ^aPastorello et al., 2005, ^bHamuy, 2001, ^cTaddia et al., 2012, ^dPastorello et al., 2012

As mentioned in section 4.1, the meaningful comparisons in Table 4.8 are between the different methods used for calculating the bolometric luminosity of a single supernova. Inter-comparisons between supernovae are hampered by the different methods of making distance estimates, and the different cosmological parameters used in the redshift-distance relations by different groups.

4.5 Nickel - Luminosity Relation

The radioactive decay of ^{56}Ni is known to power the lightcurves of supernovae during late stages in their evolution. For Type Ia supernovae, the lightcurve is entirely driven by radioactive decay, which leads to a natural relationship between the peak luminosity of the supernova and the mass of ejected ^{56}Ni known as “Arnett’s Law” (Arnett, 1982; Arnett et al., 1985; Branch, 1992). For Type II-P supernovae, there is also a correlation between plateau luminosity and ejected ^{56}Ni mass (Hamuy, 2003; Spiro et al., 2014). In Figure 4.7, we add the supernovae

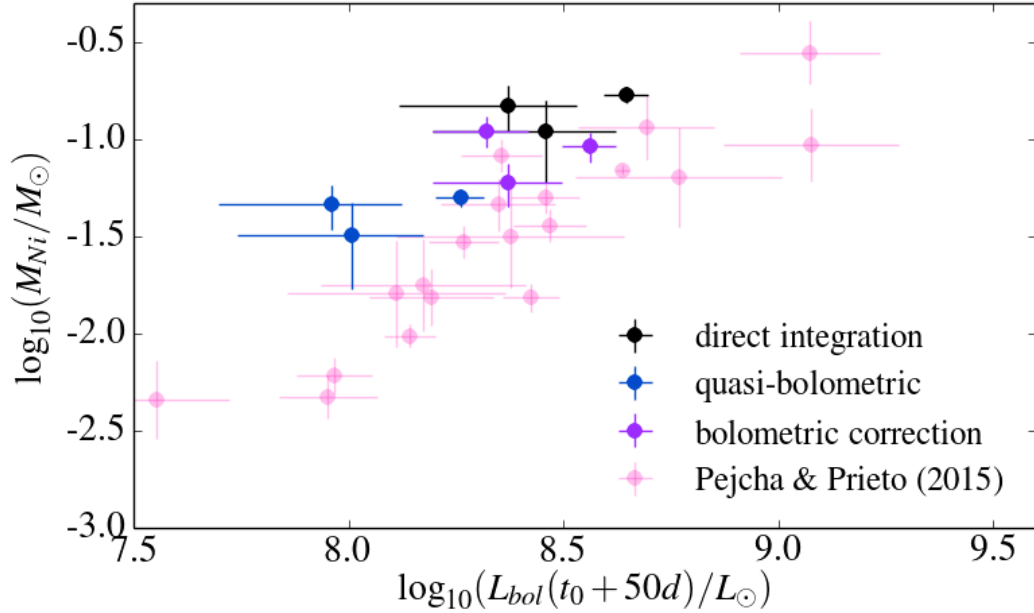


Figure 4.7 Relation between the ejected nickel mass and the bolometric luminosity of the supernova measured at $t_0 + 50d$. SN 2009E is excluded from this comparison, because no photometry is available around $t_0 + 50d$

in our sample to the dataset published by Pejcha and Prieto (2015) (their figure 15, after removal of the outlier SN 2007od for clarity.)

It should be noted that in producing these plots, we are violating the principle laid out in section 4.1, and inter-comparing the luminosities and ejected nickel masses of the supernovae in our sample. These results, therefore, should be viewed as preliminary.

While the three different methods used in this paper for calculating the bolometric luminosity produce results that follow a similar trend to the previously published results, the luminosities of the peculiar Type II-P supernovae in this sample appear systematically lower for a given value of the nickel mass than their counterparts in Pejcha and Prieto (2015). This is likely due to the slow rise

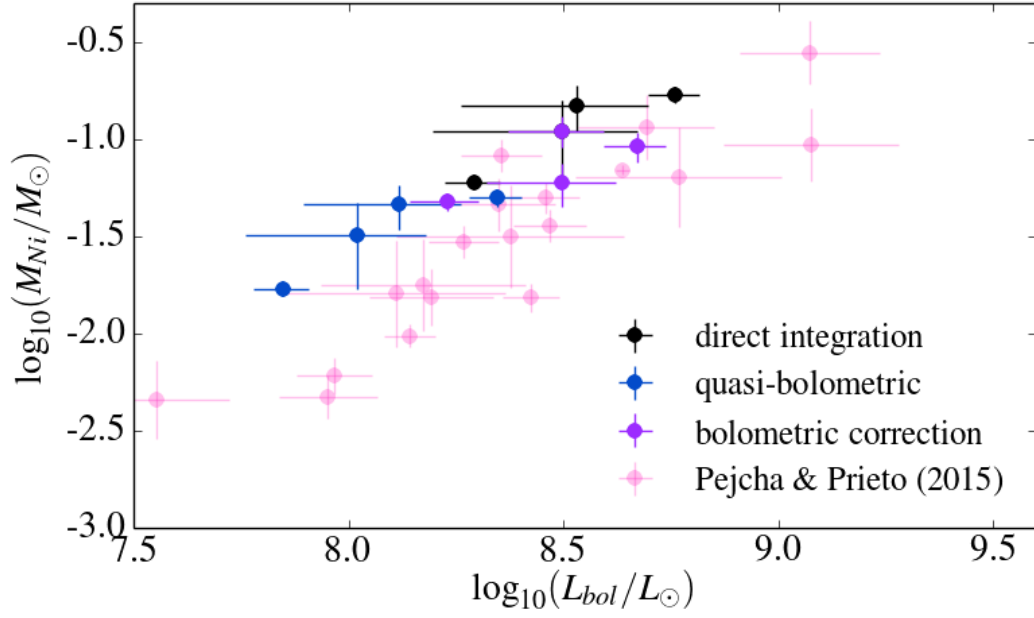


Figure 4.8 Relation between the ejected nickel mass and the bolometric luminosity of the supernova measured at peak brightness. The data from Pejcha and Prieto (2015) are still measured at $t_0 + 50\text{d}$.

times which make this set of supernovae photometrically distinct. The choice of measuring the plateau luminosity at $t_0 + 50\text{d}$ in Pejcha and Prieto (2015) works for typical Type II-P supernovae, with rise times of ~ 10 days. The SN 1987A-like supernovae in this sample, however, rise to peak luminosity much more slowly, and so are systematically dimmer at $t_0 + 50\text{d}$.

To somewhat remedy this, we instead compare the peak luminosity of our supernovae to the same dataset. This is shown in Figure 4.8. The SN 1987A-like supernovae are still dimmer for a given value of the ejected nickel mass, but are shifted closer to the main trend.

Another possible interpretation of the data is that these SN 1987A-like supernovae are producing more radioactive ^{56}Ni than more typical Type II-P supernovae

at a given plateau luminosity. If the progenitors of these SN 1987A-like supernovae are blue supergiant stars as was the progenitor of SN 1987A and as has been suggested by past studies of these supernovae, this may be an observable signature of the the progenitor star or explosion characteristics that set these supernovae apart from the general population of Type II-P supernovae.

Chapter 5

Comparison with PHOENIX models

In chapter 4, it was shown that the augmented and bolometric correction lightcurves broadly agree for this sample of peculiar Type II P supernovae, while the quasi-bolometric technique consistently under-estimated the luminosity compared to the other two techniques. Without knowing the true luminosity of the supernova, however, it is impossible to determine if the agreement between the augmented and bolometric correction luminosities reflects the true bolometric luminosity of the supernova. In order to make progress toward verifying the results of the direct integration and bolometric correction techniques, we would need to feed **SuperBoL** photometry from a supernova of known luminosity, and then compare the values of L_{bol} resulting from the different calculation techniques.

To that end, we make use of the NLTE radiative transfer code **PHOENIX** (see, for example, Hauschildt and Baron, 1999). Because **PHOENIX** calculates the full spectrum of a supernova, it is possible to convolve the output spectrum with the filter response functions of various photometric systems and compute synthetic photometry of the spectrum. In this way, it is possible to determine the absolute magnitudes of the synthetic supernova spectrum. Because the bolometric luminosity of the **PHOENIX** spectrum is known, these synthetic photometric magnitudes become excellent test data for the various bolometric luminosity calculation

techniques.

In this chapter, PHOENIX is used to produce a range of synthetic supernova spectra which roughly match the observed spectra of the supernovae studied in chapter 4. The synthetic spectra are then fed through integration routines which calculate the the synthetic absolute magnitudes of the model supernovae. Those absolute magnitudes are converted in to apparent magnitudes using the distances in Table 4.1. The apparent magnitudes are then used by **SuperBoL** to determine how closely each technique reproduces the bolometric luminosity reported by PHOENIX. This will also give us a way of better estimating any systematic errors in the luminosity calculation techniques.

The properties of the underlying hydrodynamic models used in the PHOENIX calculations are detailed in appendix A.

5.1 Initial Proof-of-concept

The initial application of PHOENIX synthetic photometry to test the different bolometric luminosity techniques was made in Lusk and Baron (2017). In that paper, the PHOENIX spectrum used was unrelated to the sample of Type II P supernovae in chapter 2. In an attempt to avoid biasing the results of this test, the author running **SuperBoL** (JL) was only given the synthetic photometry — the luminosity of the underlying PHOENIX model was not revealed until after the results had been calculated.

The initial calculations were promising. The bolometric luminosity of the synthetic spectrum was $L_{\text{bol}} = 11.08 \times 10^{41} \text{ erg s}^{-1}$. The quasi-bolometric

Table 5.1. Bolometric Luminosity with Sparse Photometry

Bands	L_{qbol} 10^{41} (erg/s)	L_{D} 10^{41} (erg/s)	L_{BC} 10^{41} (erg/s)
VRI	—	—	6.18
BVR	—	—	12.52
UBV	—	—	12.52
BVRI	3.49	10.54	8.62
UBVR	3.78	10.51	12.52
UBVRI	4.88	10.64	8.62
UBVRIJHK	7.25	11.59	8.62
L_{bol} (PHOENIX)		11.08	

technique, using the full compliment of bandpasses produced a luminosity of $L_{\text{qbol}} = 7.25 \times 10^{41} \text{ erg s}^{-1}$. The direct integration routine calculated a bolometric luminosity of $L_{\text{D}} = 11.30 \times 10^{41} \text{ erg s}^{-1}$ when utilizing all available bandpasses. The bolometric correction method resulted in $L_{\text{BC}} = 8.61 \times 10^{41} \text{ erg s}^{-1}$ when averaging the results of $B - V$, $V - I$, and $B - I$ calculations. The value calculated using the direct integration technique is remarkably close (within 5%) of the true luminosity of the synthetic spectrum. The luminosity determined through the bolometric correction technique is lower, but within 25% of the true luminosity.

In order to check the dependence of these methods on the completeness of the photometric observations, the bolometric luminosities of the PHOENIX spectrum were re-calculated using several smaller subsets of the available synthetic magnitudes. The results are shown in Table 5.1.

As was evident in the bolometric lightcurves of SN 2006au in section 4.2, the quasi-bolometric technique is very sensitive to the wavelength range of the observed photometry. Since no corrections were made for flux which falls outside

the observed range, this method consistently under-estimated the bolometric luminosity of the PHOENIX model by a significant amount.

One promising result was the consistency in the luminosity calculated using the direct integration technique, even when the wavelength range of the observed photometry varied significantly. Based on the design of the technique, this is to be expected — since missing flux blueward and redward of the observed wavelength range is filled in using the assumption of a blackbody SED. The concordance between the expected behavior of the technique and the results produced by SuperBoL, and the close match between the calculated and model luminosity for all subsets of the observed photometry, are encouraging.

The results obtained by the bolometric correction technique were more puzzling. The luminosity shows a large variation, depending on which of the three filter combinations are available for averaging.

With only one PHOENIX model, any conclusions of the above analysis are tentative at best. In order to more fully investigate the performance of the different bolometric luminosity calculation techniques, it is necessary to create many more PHOENIX spectra which match as closely as possible the observed spectroscopic data from a sample of supernovae. In the sections to come, we present 26 PHOENIX spectra of different luminosities, constructed to closely match 6 different observed spectra of peculiar Type II-P supernovae (3 early-phase spectra and 1 plateau-phase spectrum of SN 2000cb, 1 early-phase spectrum and 1 plateau-phase spectrum of SN 2006au.) With four different techniques used to calculate the bolometric luminosity of each different PHOENIX spectrum, this gives

a set of 104 comparisons between true and calculated luminosities in section 5.2 and section 5.3. An additional 152 comparisons are made in section 5.5, this time to investigate how limiting the photometry available to **SuperBoL** to subsets of the more commonly-used *UBVRI* optical bands changes the accuracies of the quasi-bolometric and augmented bolometric calculation techniques.

5.2 Early phase synthetic spectra

Of the supernovae in this sample, only SNe 2000cb and 2006au have observed spectra within the first ~ 2 weeks after explosion. Being Type II-P supernovae, they exhibit strong lines of hydrogen and helium in their spectra, slowly developing lines of intermediate-mass elements and iron-peak elements as the ejecta expands and cools (see, e.g. Filippenko, 1997, for an excellent review.)

5.2.1 SN 2000cb, JD 2451662.9

The earliest available spectrum of SN 2000cb was taken on April 28 (2000-04-28 08:52 UT) using the FAST spectrograph on the Tillinghast 1.5-m telescope at the F. L. Whipple Observatory. Details of this spectroscopic observation and an analysis of the spectroscopic evolution of SN 2000cb can be found in Kleiser et al., 2011. The most striking spectroscopic feature of SN 2000cb is the high expansion velocities inferred from the P-Cygni profiles of dominant lines such as H- α . The earliest available spectrum, taken roughly 7 days after explosion, shows an H- α expansion velocity of over 18,000 km s $^{-1}$. At similar epochs, the H- α velocities of SNe 1987A and 1999em are 15,000 km s $^{-1}$ and 10,000 km s $^{-1}$, respectively.

The H- α velocities remain several thousand km/s higher than either of the other supernovae throughout the spectroscopic evolution of the objects.

The synthetic spectra that best fit the observed spectrum of SN 2000cb were created using a hydrodynamic model with inner and outer density power-law exponents of $m = 1.06$ and $n = 7$, respectively. The velocity range covered by the model stretches from $v_{\min} = 3100 \text{ km s}^{-1}$ at the inner boundary of the model to $v_{\max} = 30,000 \text{ km s}^{-1}$ at the outer boundary. All models contain an ejected mass of $M_{\text{ej}} = 20.0 \text{ M}_{\odot}$ and total deposited energy of $E = 3.0 \times 10^{51} \text{ erg}$. Assuming the explosion date given in Table 4.1 is correct, the model is assumed to have been in homologous expansion for 7 days.

Several different models were created with these parameters, differing only by their total luminosities. Figure 5.1 shows a comparison between three of these models and the observed spectrum of SN 2000cb from Kleiser et al. (2011), de-reddened assuming the extinction ratio given in Table 4.1 using the extinction law of Fitzpatrick, 1999 with $R_V = 3.1$.

Table 5.2 shows the synthetic photometry of these models in the Vega magnitude system. Throughout this chapter, we will assume that the distance to SN 2000cb is 30 Mpc.

Table 5.3 gives the results of applying the bolometric luminosity calculation techniques implemented in **SuperBoL** to the synthetic photometry given in Table 5.2. These luminosities are calculated assuming no uncertainty in the distance to the supernova, but with the assumption of a 0.015 mag uncertainty in the synthetic photometry. The relatively small uncertainty was chosen to reflect the

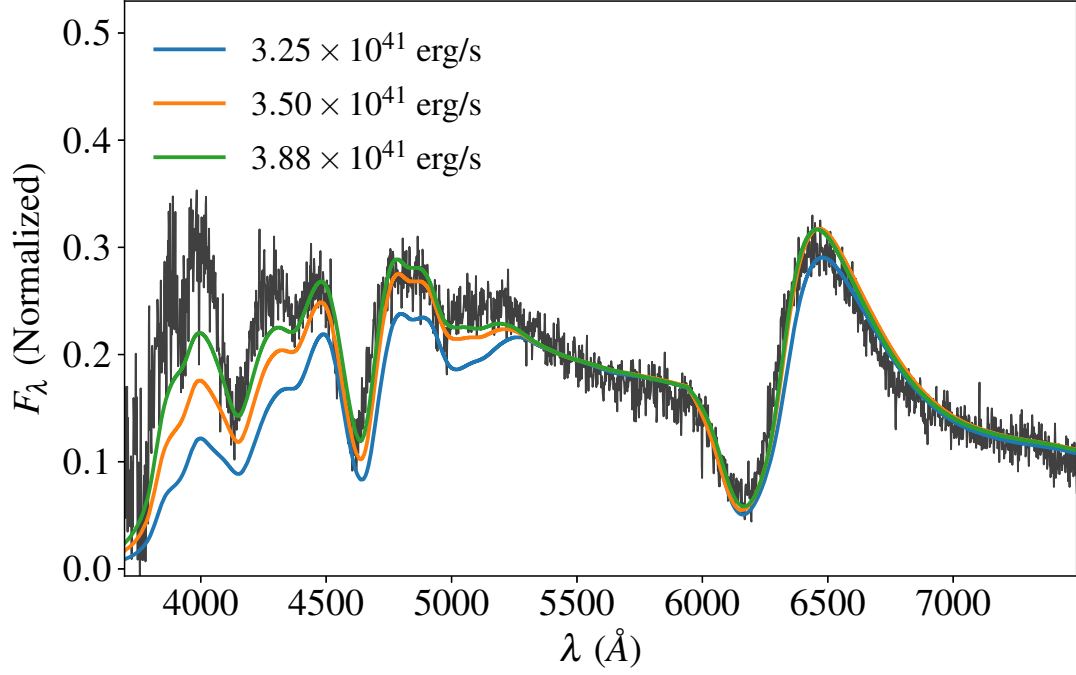


Figure 5.1 PHOENIX spectra similar to that of SN 2000cb 7 days post-explosion, normalized to match the observed spectrum at $\lambda = 5500\text{\AA}$

Table 5.2. Synthetic photometry of PHOENIX spectra similar to SN 2000cb 7 days post-explosion, assuming a distance of 30 Mpc

Model L_{bol} erg/s	U mag	B mag	V mag	R mag	I mag	J mag	H mag
3.25×10^{41}	19.532	18.000	17.158	16.809	16.669	16.311	16.201
3.50×10^{41}	18.906	17.797	17.143	16.778	16.590	16.296	16.166
3.88×10^{41}	18.434	17.585	17.049	16.696	16.482	16.237	16.095

Table 5.3. Comparison of **SuperBoL** bolometric luminosities from **PHOENIX** synthetic photometry, assuming a distance of 30.0 ± 0 Mpc and photometric uncertainties of 0.015 mag

Model L_{bol} 10^{41} erg/s	L_{qbol} 10^{41} erg/s	L_{aug} 10^{41} erg/s	L_{BC} (H01) 10^{41} erg/s	L_{BC} (BH09) 10^{41} erg/s
3.25	2.77 ± 0.02	3.22 ± 0.06	3.5 ± 0.4	3.3 ± 0.3
3.50	2.97 ± 0.02	3.45 ± 0.10	3.6 ± 0.4	3.4 ± 0.3
3.88	3.29 ± 0.02	3.83 ± 0.16	4.1 ± 0.4	3.7 ± 0.4
MRE:	15.0×10^{-2}	1.09×10^{-2}	5.7×10^{-2}	2.9×10^{-2}

minimum error in the observed photometry published in Hamuy (2001). The value of 0.015 mag was chosen by Hamuy (2001) to be representative of the Poisson statistics in a single CCD observation of a Landolt standard star. The synthetic photometry process, where the filter transmission functions and the model spectra are known, has actual uncertainties much smaller than this value – but those small uncertainties are an unrealistic representation of the uncertainty in typical photometric observations. To more easily compare the accuracy with which the different bolometric luminosity calculation techniques reproduce the true luminosity of the model, the last row gives the mean relative error (MRE) for each of the different techniques. As an example, the mean relative error in the case of the quasi-bolometric technique is defined by Equation 5.1.

$$MRE_{\text{qbol}} = \frac{1}{N} \sum_{i=1}^N \frac{|L_{\text{qbol},i} - \text{Model } L_{\text{bol},i}|}{\text{Model } L_{\text{bol},i}}, \quad (5.1)$$

where the index i runs over the available **PHOENIX** models. The other mean relative errors are defined in the same manner.

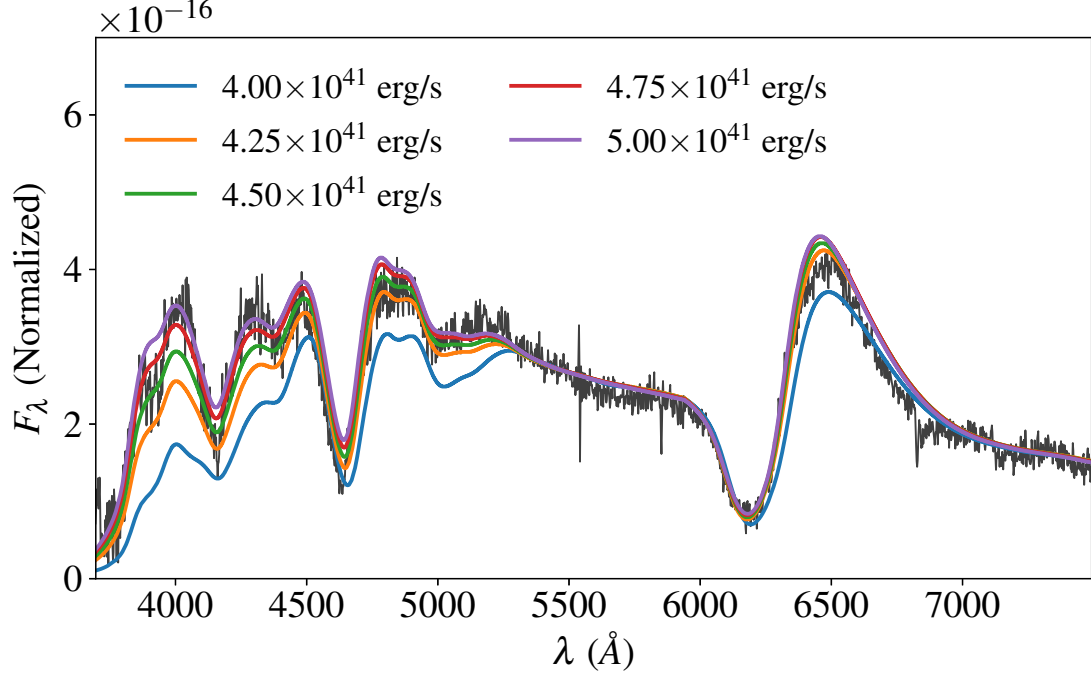


Figure 5.2 PHOENIX spectra similar to that of SN 2000cb 8 days post-explosion, normalized to match the observed spectrum at $\lambda = 5500\text{\AA}$

5.2.2 SN 2000cb, JD 2451663.9

The spectrum of SN 2000cb taken on April 29 (2000-04-29 08:40 UT) using the 4.0-m telescope at the Cerro Tololo Inter-American Observatory (CTIO) was released as part of a dataset of 888 spectra of Type II supernovae by Gutiérrez et al., 2017. Details of this spectroscopic observation and an discussion of the photometric and spectroscopic features of SN 2000cb can be found in Hamuy, 2001.

The hydrodynamic models used at inputs to PHOENIX are exactly the same as the models used to produce the spectra in Figure 5.1, but allowed to expand an extra day.

Table 5.4 shows the synthetic photometry of these models in the Vega magni-

Table 5.4. Synthetic photometry of **PHOENIX** spectra similar to SN 2000cb 8 days post-explosion, assuming a distance of 30 Mpc

Model L_{bol} erg/s	U mag	B mag	V mag	R mag	I mag	J mag	H mag
4.00×10^{41}	19.320	17.730	16.900	16.572	16.416	16.051	15.925
4.25×10^{41}	18.593	17.564	16.923	16.567	16.367	16.100	15.971
4.50×10^{41}	18.330	17.440	16.881	16.527	16.314	16.071	15.933
4.75×10^{41}	18.114	17.334	16.838	16.486	16.268	16.048	15.910
5.00×10^{41}	17.945	17.239	16.787	16.440	16.222	16.015	15.872

Table 5.5. Comparison of **SuperBoL** bolometric luminosities from **PHOENIX** synthetic photometry, assuming a distance of 30.0 ± 0 Mpc and photometric uncertainties of 0.015 mag

Model L_{bol} 10^{41} erg/s	L_{qbol} 10^{41} erg/s	L_{aug} 10^{41} erg/s	L_{BC} (H01) 10^{41} erg/s	L_{BC} (BH09) 10^{41} erg/s
4.00	3.51 ± 0.02	4.08 ± 0.07	4.5 ± 0.5	4.2 ± 0.4
4.25	3.62 ± 0.02	4.20 ± 0.14	4.5 ± 0.5	4.2 ± 0.4
4.50	3.83 ± 0.02	4.45 ± 0.18	4.7 ± 0.5	4.4 ± 0.4
4.75	4.02 ± 0.02	4.7 ± 0.2	5.0 ± 0.5	4.6 ± 0.4
5.00	4.24 ± 0.03	4.9 ± 0.3	5.3 ± 0.6	4.8 ± 0.5
MRE:	14.5×10^{-2}	1.40×10^{-2}	6.4×10^{-2}	3.8×10^{-2}

tude system.

Table 5.5 gives the bolometric luminosity estimates from the different calculation techniques implemented in **SuperBoL**, using the synthetic photometry given in Table 5.4 as inputs. These luminosities are calculated assuming no uncertainty in the distance to the supernova, but assuming a 0.015 mag uncertainty in the synthetic photometry.

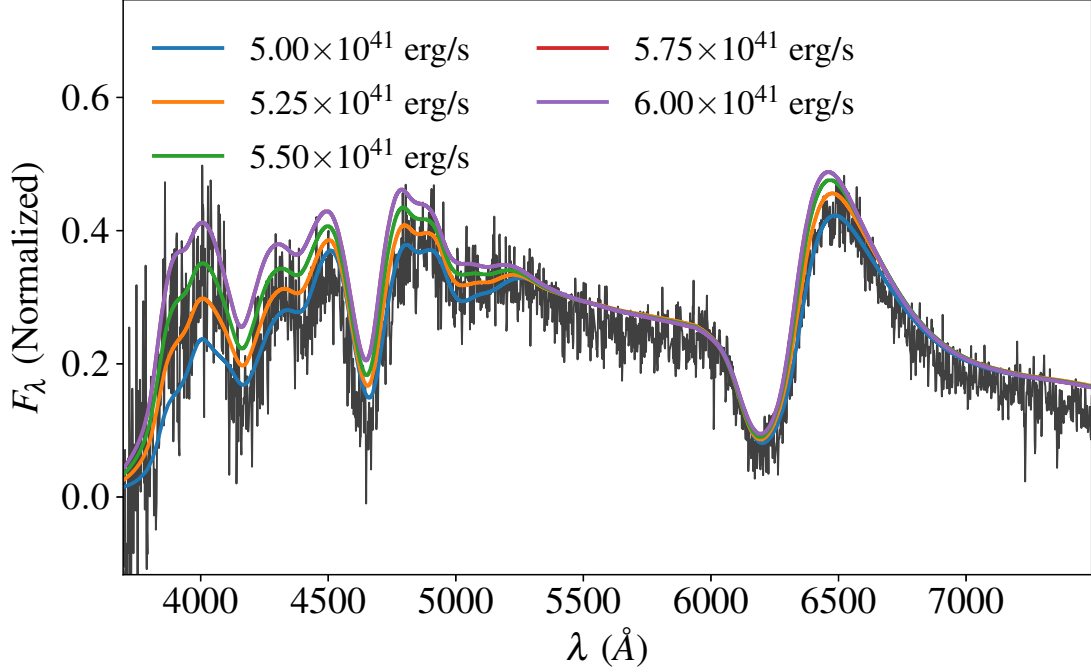


Figure 5.3 PHOENIX spectra similar to that of SN 2000cb 9 days post-explosion, normalized to match the observed spectrum at $\lambda = 5500\text{\AA}$

5.2.3 SN 2000cb, JD 2451664.9

The observed spectrum of SN 2000cb shown in Figure 5.3 was taken on April 30 (2000-04-30:09:07 UT), again with the FAST spectrograph on the Tillinghast 1.5-m telescope at the F. L. Whipple Observatory.

The hydrodynamic models have the same parameters as those shown previously, differing only in the assumed time since explosion (9 days, in the case of the models shown here) and the luminosities.

Synthetic photometry of the models shown in Figure 5.3 is given in Table 5.6.

The bolometric luminosities derived from the synthetic photometry in Table 5.6 are shown in Table 5.7.

Table 5.6. Synthetic photometry of PHOENIX spectra similar to SN 2000cb 9 days post-explosion, assuming a distance of 30 Mpc

Model L_{bol} erg/s	U mag	B mag	V mag	R mag	I mag	J mag	H mag
5.00×10^{41}	18.818	17.405	16.679	16.358	16.201	15.872	15.742
5.25×10^{41}	18.307	17.297	16.687	16.345	16.145	15.881	15.753
5.50×10^{41}	18.005	17.184	16.665	16.320	16.104	15.885	15.749
5.75×10^{41}	17.827	17.093	16.630	16.285	16.065	15.861	15.724
6.00×10^{41}	17.679	17.014	16.591	16.250	16.031	15.839	15.702

Table 5.7. Comparison of SuperBoL bolometric luminosities from PHOENIX synthetic photometry, assuming a distance of 30.0 ± 0 Mpc and photometric uncertainties of 0.015 mag

Model L_{bol} 10^{41} erg/s	L_{qbol} 10^{41} erg/s	L_{aug} 10^{41} erg/s	L_{BC} (H01) 10^{41} erg/s	L_{BC} (BH09) 10^{41} erg/s
5.00	4.33 ± 0.03	5.02 ± 0.11	5.6 ± 0.6	5.2 ± 0.5
5.25	4.48 ± 0.03	5.20 ± 0.18	5.6 ± 0.6	5.2 ± 0.5
5.50	4.67 ± 0.03	5.4 ± 0.2	5.8 ± 0.6	5.3 ± 0.5
5.75	4.88 ± 0.03	5.7 ± 0.3	6.1 ± 0.6	5.5 ± 0.5
6.00	5.09 ± 0.03	5.9 ± 0.3	6.4 ± 0.7	5.7 ± 0.6
MRE:	14.7×10^{-2}	1.01×10^{-2}	7.0×10^{-2}	3.3×10^{-2}

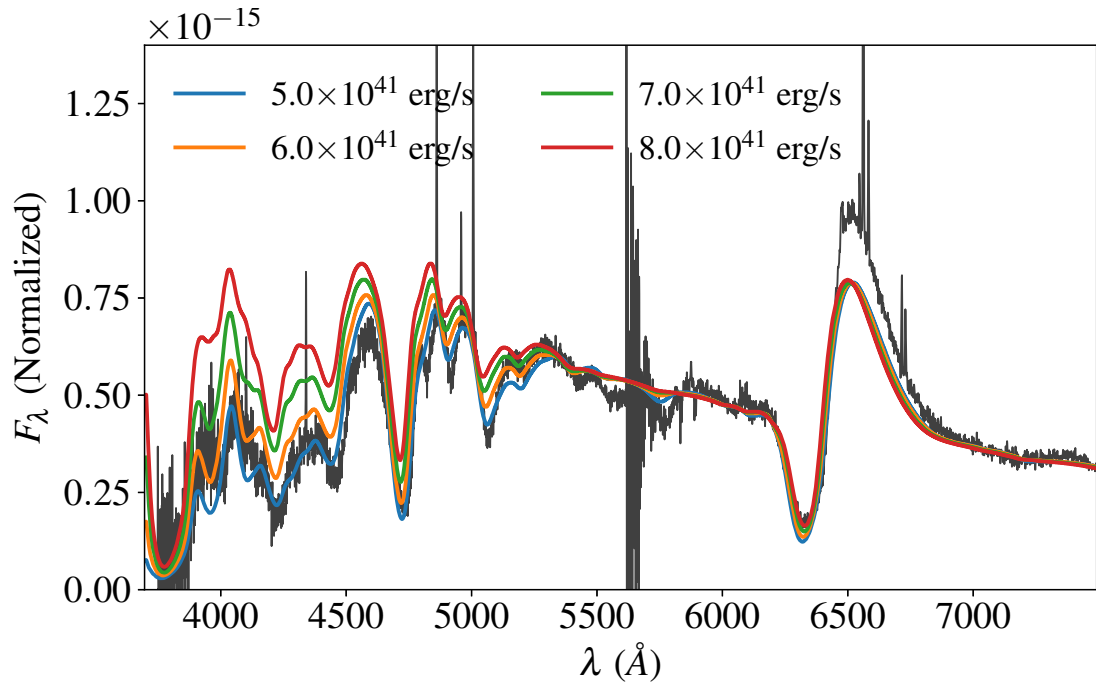


Figure 5.4 PHOENIX spectra similar to that of SN 2006au 15 days post-explosion, normalized to match the observed spectrum at $\lambda = 6000\text{\AA}$

5.2.4 SN 2006au, JD 2453808.9

Supernova SN 2006au is the only other supernova in this sample with spectroscopic observations taken during the first ~ 2 weeks of evolution after explosion. The earliest available spectrum of SN 2006au was taken on March 14, 2006 (2006-03-14:09:20 UT) using the Low Dispersion Survey Spectrograph on the 6.5-m Clay telescope at Las Campanas Observatory, first published in Taddia et al. (2012). The spectrum is shown in Figure 5.4, and exhibits clear signs of intermediate-mass elements like Na ID (5890\AA & 5896\AA), and clear absorption lines of Fe (most notably the Fe II lines at 5169\AA , 5018\AA , and 4924\AA .) The prominent noise around $\sim 5600\text{\AA}$ is instrumental: the spectrum is a combination of two grism spectra, one covering a range of $3785\text{\AA} - 6129\text{\AA}$, and the other covering $5673\text{\AA} - 9969\text{\AA}$.

The synthetic spectra that best fit the observed spectrum of SN 2006au are based on hydrodynamic models with inner and outer density power-law exponents of $m = 1.06$ and $n = 9$, respectively. The outer density power-law exponent is steeper than that needed for the SN 2000cb models shown in the previous sections. The steeper power-law is needed to re-produce the correct H- α line profile, with its steeper transition from emission peak to absorption trough. Steepening the power-law also locates the photosphere at the correct velocity such that the Fe II absorption minima appear at the correct velocities with respect to the rest wavelengths of the lines. These iron lines are commonly used as indicators of photospheric velocity because the line-forming region for these lines tracks the transition from optically-thin to optically-thick quite well (Taddia et al., 2012). The velocity range covered by the model stretches from $v_{\min} = 3100 \text{ km s}^{-1}$ at the inner boundary of the model to $v_{\max} = 18,000 \text{ km s}^{-1}$ at the outer boundary. The lower outer boundary velocity of the model, along with the outer density power-law exponent helps to set the bluest wavelength extent of the H- α absorption feature. All models contain an ejected mass of $M_{\text{ej}} = 20.0 \text{ M}_{\odot}$ and total deposited energy of $E = 3.0 \times 10^{51} \text{ erg}$. Assuming the explosion date given in Table 4.1 is correct, the model is assumed to have been in homologous expansion for 15 days.

Table 5.8 shows the synthetic photometry of these models in the Vega magnitude system. Throughout this chapter, we assume that the distance to SN 2006au is 46 Mpc – the same value used by Taddia et al. (2012) and in the bolometric lightcurve analysis in chapter 4.

Table 5.9 gives the bolometric luminosity estimates from **SuperBoL** using the

Table 5.8. Synthetic photometry of PHOENIX spectra similar to SN 2006au 15 days post-explosion, assuming a distance of 46 Mpc

Model L_{bol} erg/s	U mag	B mag	V mag	R mag	I mag	J mag	H mag
5.00×10^{41}	19.928	18.450	17.550	17.226	16.997	16.717	16.564
6.00×10^{41}	19.319	18.129	17.380	17.070	16.837	16.583	16.430
7.00×10^{41}	18.723	17.837	17.234	16.941	16.699	16.487	16.336
8.00×10^{41}	18.225	17.593	17.113	16.833	16.584	16.409	16.259

Table 5.9. Comparison of SuperBoL bolometric luminosities from PHOENIX synthetic photometry in Table 5.8, with photometric uncertainties of 0.015 mag

Model L_{bol} 10^{41} erg/s	L_{qbol} 10^{41} erg/s	L_{aug} 10^{41} erg/s	L_{BC} (H01) 10^{41} erg/s	L_{BC} (BH09) 10^{41} erg/s
5.00	4.56 ± 0.03	5.31 ± 0.10	5.8 ± 0.6	5.6 ± 0.5
6.00	5.40 ± 0.03	6.27 ± 0.17	6.8 ± 0.7	6.5 ± 0.6
7.00	6.27 ± 0.04	7.3 ± 0.3	7.9 ± 0.8	7.4 ± 0.7
8.00	7.14 ± 0.04	8.3 ± 0.5	9.2 ± 1.0	8.2 ± 0.8
MRE:	9.97×10^{-2}	4.7×10^{-2}	14×10^{-2}	6.6×10^{-2}

the synthetic photometry given in Table 5.8 as inputs to the different calculation techniques detailed in chapter 3. These luminosities are calculated assuming no uncertainty in the distance to the supernova, but assuming a 0.015 mag uncertainty in the synthetic photometry.

5.3 Plateau phase synthetic spectra

Both SN 2000cb and SN 2006au were observed during the broad, dome-shaped plateau phase which seems typical of the supernovae in this sample. While SN 2000cb was observed near its peak luminosity, the spectroscopic observations

of SN 2006au end shortly before the peak of the bolometric lightcurve. The hydrodynamic models of both supernovae used in the construction of these plateau-phase spectra have different outer density power-law exponents compared to those in section 5.2. This is done in each case to best re-produce the observed spectrum of the supernova. Because the goal of this investigation is not to fully characterize the progenitor of these supernovae, but rather to test the accuracy of different bolometric lightcurve investigation techniques, the models used are not fully consistent from one epoch to the next. However, the density profile of the actual ejecta is likely not described by a simple two power-law model with a sharp transition – so it is perhaps reasonable to assume that as the supernova expands and cools, the photosphere would recede in velocity to regions where the density exponents would take on intermediate values between the inner and outer power-law exponents used in the early-phase models. Indeed, the power-law exponents used in the sections that follow are both shallower than the outer power-law exponents used in the previous sections. The purpose of these “snapshot” models is to produce supernova spectra with shapes that match as closely as possible the observed spectra, to provide realistic synthetic photometry that can be fed into the different bolometric luminosity calculation techniques.

5.3.1 SN 2006au, JD 2453850.9

The most evolved spectrum of SN 2006au available was taken on April 25, 2006 (2006-04-25:08:51 UT) using Wide Field Reimaging CCD Camera on the 2.5-m Irénée du Pont telescope at Las Campanas Observatory, first published in Taddia

et al. (2012).

The plateau-phase spectrum of SN 2006au is broadly similar to that of other peculiar Type II-P supernovae in this sample. Prominent P-Cygni lines of H- α , Ca II, Na I D, Fe II, and other metals all appear, though Ba II is much weaker in this object than other members of the class. The expansion velocities inferred from the P-Cygni profile of H- α is initially quite fast, exceeding 10,000 km s⁻¹ in the first spectrum taken on March 14, but the velocities decline in much the same way as those of SN 1987A. Photospheric lines of Fe II have lower velocities of between 6,000 – 5,000 km s⁻¹.

The PHOENIX spectra that best re-create the observed spectrum of SN 2006au are based on hydrodynamic models with an inner density power-law exponent of $m = 1.06$ and an outer power-law exponent of $n = 8$. The velocity range covered by the model stretches from $v_{\min} = 2000$ km s⁻¹ at the inner boundary of the model to $v_{\max} = 11,700$ km s⁻¹ at the outer boundary. The outer velocity of the model and the outer density power-law exponent were constrained by the narrower H- α , P-Cygni profile evident in this spectrum, and the sharp transition from emission peak to absorption trough. All models contain an ejected mass of $M_{\text{ej}} = 20.0 M_{\odot}$ and total deposited energy of $E = 3.0 \times 10^{51}$ erg. Using the explosion date given in Table 4.1, the model is assumed to have been in homologous expansion for 57 days.

Figure 5.5 shows the observed spectrum and four PHOENIX spectra derived from the aforementioned hydrodynamic model at different bolometric luminosities.

The synthetic photometry of the models shown in Figure 5.5 is given in

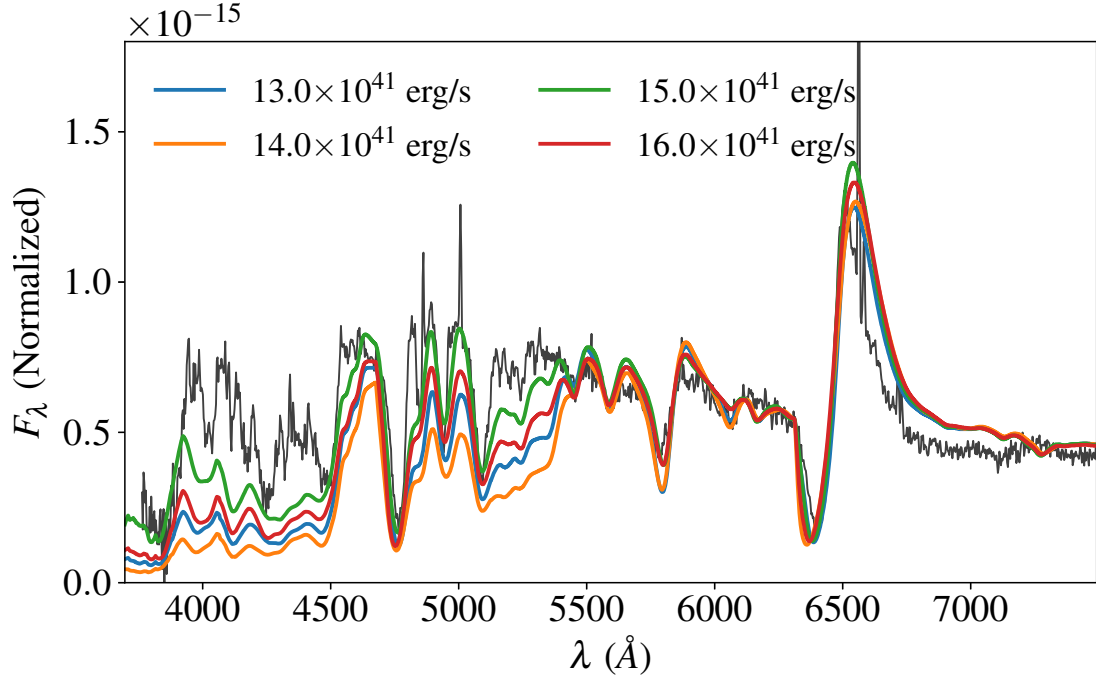


Figure 5.5 PHOENIX spectra similar to that of SN 2006au 57 days post-explosion, normalized to match the observed spectrum at $\lambda = 6260\text{\AA}$

Table 5.10, using the assumed distance of SN 2006au of 46 Mpc.

The synthetic magnitudes were input into **SuperBoL**, and the resulting bolometric luminosities from each of the different luminosity calculation techniques is given in Table 5.11, assuming a distance to SN 2006au of 46 Mpc and an uncertainty in the photometric magnitudes of 0.015 mag.

5.3.2 SN 2000cb, JD 2451722.8

The spectrum of SN 2000cb shown in Figure 5.6 was taken near the peak brightness of the supernova lightcurve on June 27, 2000 (2000-06-27:06:21) using the Kast Double Spectrograph attached to the 3.0-m Shane telescope at Lick Observatory. Especially prominent in the spectrum at this epoch are the strong Ba II 6142 \AA

Table 5.10. Synthetic photometry of PHOENIX spectra similar to SN 2006au 57 days post-explosion, assuming a distance of 46 Mpc

Model L_{bol} erg/s	U mag	B mag	V mag	R mag	I mag	J mag	H mag
13.0×10^{41}	19.243	18.167	16.838	16.240	15.697	15.551	15.337
14.0×10^{41}	19.660	18.311	16.815	16.107	15.678	15.426	15.196
15.0×10^{41}	18.208	17.666	16.586	16.089	15.464	15.471	15.286
16.0×10^{41}	18.741	17.831	16.580	16.004	15.494	15.374	15.173

Table 5.11. Comparison of SuperBoL bolometric luminosities from PHOENIX synthetic photometry in Table 5.10, with photometric uncertainties of 0.015 mag

Model L_{bol} 10^{41} erg/s	L_{qbol} 10^{41} erg/s	L_{aug} 10^{41} erg/s	L_{BC} (H01) 10^{41} erg/s	L_{BC} (BH09) 10^{41} erg/s
13.0	11.57 ± 0.08	13.87 ± 0.19	13.4 ± 1.4	15.9 ± 1.5
14.0	12.15 ± 0.08	14.81 ± 0.15	14.5 ± 1.6	22 ± 2
15.0	14.14 ± 0.09	16.6 ± 0.5	16.9 ± 1.8	15.7 ± 1.5
16.0	14.21 ± 0.09	16.9 ± 0.3	16.5 ± 1.7	17.5 ± 1.7
MRE:	10.3×10^{-2}	7.20×10^{-2}	5.59×10^{-2}	23×10^{-2}

Table 5.12. Synthetic photometry of PHOENIX spectra similar to SN 2000cb 67 days post-explosion, assuming a distance of 30 Mpc

Model L_{bol} erg/s	U mag	B mag	V mag	R mag	I mag	J mag	H mag
9.00×10^{41}	18.225	17.298	16.263	15.696	14.995	15.164	14.998
10.0×10^{41}	18.273	17.321	16.169	15.558	14.953	15.008	14.854
11.0×10^{41}	17.488	16.846	16.001	15.497	14.720	15.014	14.871
12.0×10^{41}	17.352	16.800	15.914	15.360	14.627	14.890	14.739
13.0×10^{41}	16.240	16.373	15.821	15.370	14.343	14.922	14.788

and Na ID (5890Å & 5896Å) lines, along with the photospheric Fe II lines.

The PHOENIX models which best re-produce the observed spectrum of SN 2000cb during the plateau phase are shown in Figure 5.6. The broken power-law hydrodynamic models behind these synthetic spectra are formed from an inner shallow density power-law exponent of $m = 1.06$ and an outer steep power-law exponent of $n = 5.2$. The outer power-law exponent is shallower than that of SN 2006au at a similar stage in its evolution, but was necessary to produce the correct H- α line profiles and photospheric line velocities. The inner velocity boundary of the models is $v_{\text{min}} = 1,750$ km/s, and the outer velocity is set to $v_{\text{max}} = 14,000$ km/s to best match the blue edge of the H- α line profile. The models contain an ejected mass of $M_{\text{ej}} = 20.0 M_{\odot}$ and total deposited energy of $E = 3.0 \times 10^{51}$ erg. Using the explosion date given in Table 4.1, the model is assumed to have been in homologous expansion for 67 days.

After adopting a distance to SN 2000cb of 30 Mpc, the synthetic photometry of the models shown in Figure 5.5 was calculated, and is presented in Table 5.12.

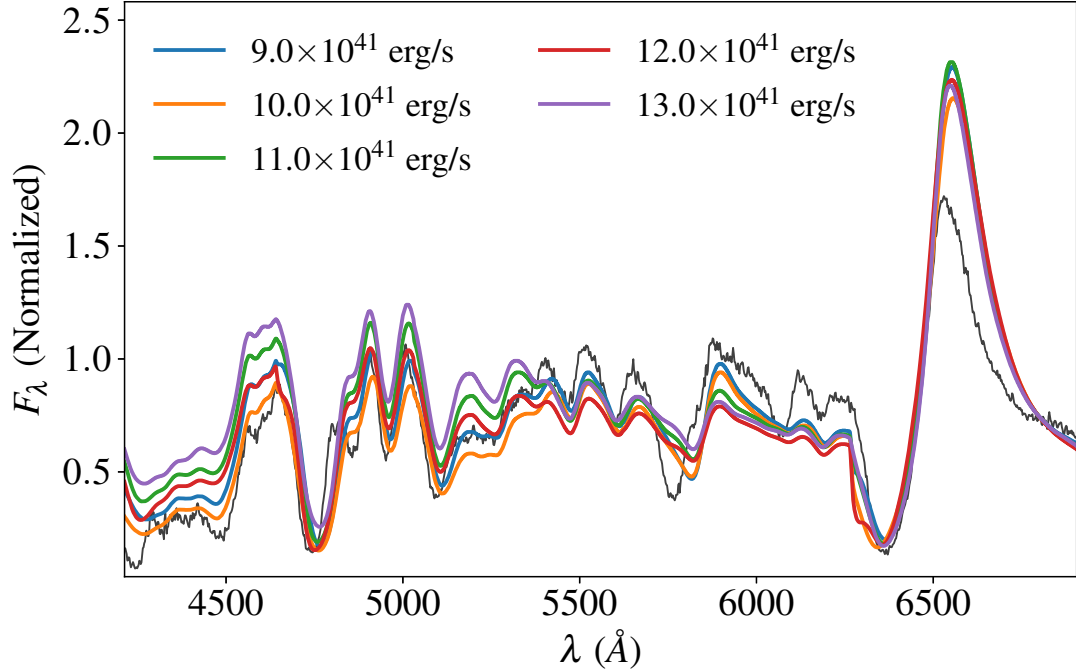


Figure 5.6 PHOENIX spectra similar to that of SN 2000cb 67 days post-explosion, normalized to match the observed spectrum at $\lambda = 6800\text{\AA}$

With synthetic magnitudes from Table 5.12, SuperBoL was used to calculate bolometric luminosities using each of the different luminosity calculation techniques discussed in chapter 3. The resulting bolometric luminosities are given in Table 5.13, assuming a distance to SN 2000cb of 30 Mpc and an uncertainty in the photometric magnitudes of 0.015 mag.

5.4 Analysis of bolometric luminosity techniques

5.4.1 Early phase luminosities

Figure 5.7 shows the data from Table 5.3, normalized to the true luminosity of the PHOENIX model. As expected from the limitations of the technique, the quasi-bolometric method of calculating the luminosity systematically under-estimates

Table 5.13. Comparison of **SuperBoL** bolometric luminosities from **PHOENIX** synthetic photometry, assuming a distance of 30.0 ± 0 Mpc and photometric uncertainties of 0.015 mag

Model L_{bol} 10^{41} erg/s	L_{qbol} 10^{41} erg/s	L_{aug} 10^{41} erg/s	L_{BC} (H01) 10^{41} erg/s	L_{BC} (BH09) 10^{41} erg/s
9.00	8.61 ± 0.06	10.0 ± 0.20	10.4 ± 1.1	9.6 ± 0.9
10.0	9.28 ± 0.06	10.84 ± 0.19	11.1 ± 1.2	11.1 ± 1.1
11.0	10.95 ± 0.08	12.6 ± 0.4	13.4 ± 1.4	10.9 ± 1.0
12.0	12.02 ± 0.08	13.9 ± 0.4	14.5 ± 1.5	12.1 ± 1.2
13.0	14.46 ± 0.10	16.8 ± 1.2	16.6 ± 1.7	12.4 ± 1.2
MRE:	4.67×10^{-2}	15.7×10^{-2}	19.3×10^{-2}	4.91×10^{-2}

the true luminosity of the **PHOENIX** model. The augmented bolometric luminosity technique performs quite well for all three models, reproducing the true luminosity to within a few percent. All three luminosities produced by the augmented technique are slightly dimmer than the true luminosities of the models. The performance of the bolometric correction techniques is more varied: The newer technique of Bersten and Hamuy (2009) agrees to within $\sim 5\%$, over-estimating the luminosity of the 3.25×10^{41} erg s $^{-1}$ model, but under-estimating the luminosities of the other two. The older bolometric correction technique of Hamuy (2001) seems to systematically over-estimate the luminosity by $\sim 5\%$, perhaps owing to a systematic effect resulting from the smaller set of template supernovae used in the calculation of the bolometric correction polynomial coefficients.

Roughly the same relations hold for the bolometric luminosity estimates listed in Table 5.5 and shown in Figure 5.8. The exceptions are the quasi-bolometric luminosity and the augmented bolometric luminosity of the 4.00×10^{41} erg s $^{-1}$

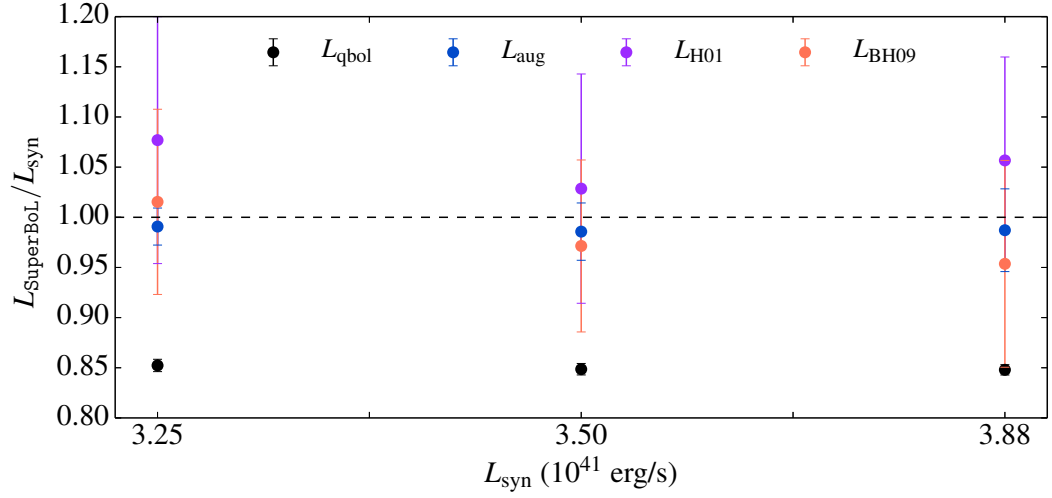


Figure 5.7 Comparison of **SuperBoL**-derived luminosities of **PHOENIX** model synthetic photometry with the luminosity of the **PHOENIX** model, for models similar to SN 2000cb 7 days post-explosion

model. The quasi-bolometric luminosity is slightly closer to the true value than the other quasi-bolometric luminosities of this sample of models. Similarly, rather than slightly under-estimating the luminosity of the model, the augmented bolometric luminosity is slightly over-estimated. To understand why, it is instructive to look at the SED generated by **SuperBoL** over-plotted with the model spectrum and the blackbody fit. This is shown in Figure 5.9 and Figure 5.10.

The differences between the quasi-bolometric luminosities for the $4.00 \times 10^{41} \text{ erg s}^{-1}$ model and the $4.50 \times 10^{41} \text{ erg s}^{-1}$ model seem to come from the B -band portion of the SED. More of the model flux between $\approx 4000\text{\AA}$ and $\approx 6000\text{\AA}$ lies above the SED in the $4.5 \times 10^{41} \text{ erg s}^{-1}$ model than in the same wavelength region of the $4.0 \times 10^{41} \text{ erg s}^{-1}$ model. This difference leads to the more pronounced under-estimation of the true luminosity of the brighter model by the quasi-bolometric

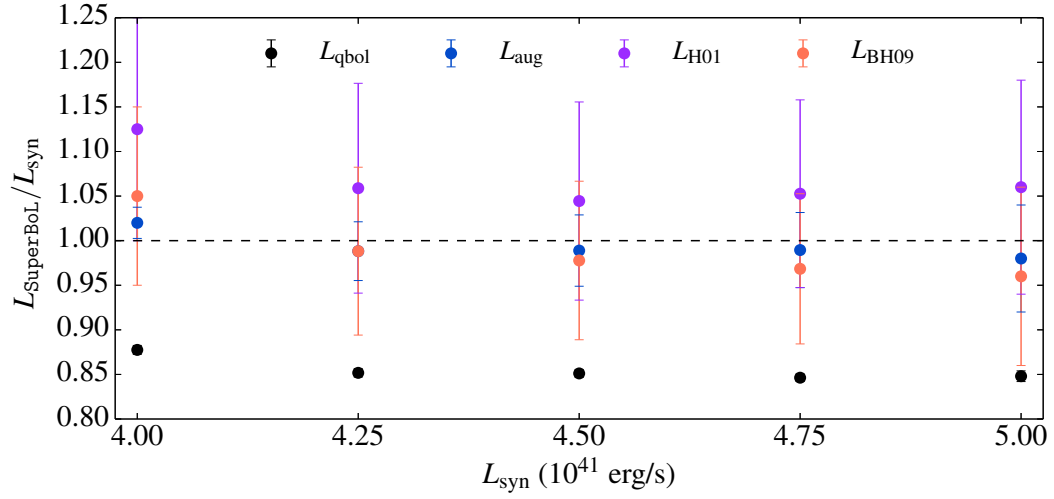


Figure 5.8 Comparison of **SuperBoL**-derived luminosities of **PHOENIX** model synthetic photometry with the luminosity of the **PHOENIX** model, for models similar to SN 2000cb 8 days post-explosion.

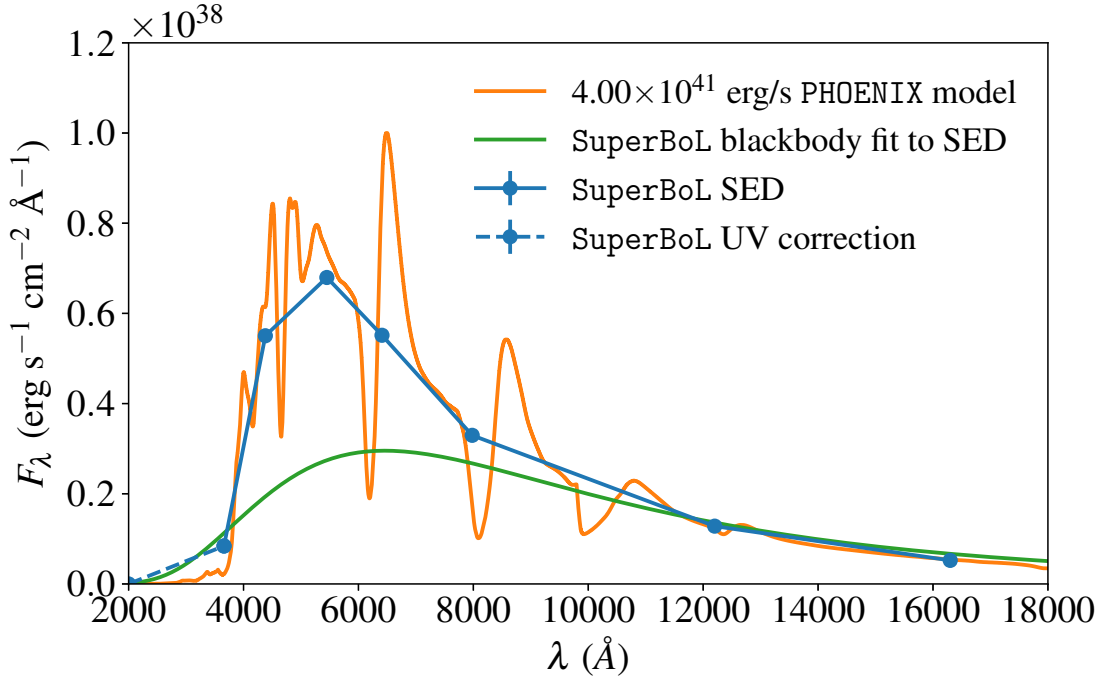


Figure 5.9 Comparison between the spectrum of the $4.00 \times 10^{41} \text{ erg s}^{-1}$ **PHOENIX** model with the **SuperBoL**-SED derived from its synthetic photometry and the blackbody fit to the fluxes of the full SED. Since the *U*-band flux is lower than the blackbody fit, the linear UV correction is used.

Table 5.14. Comparison of the luminosities derived from bolometric correction techniques using different color combinations, based on the synthetic magnitudes of two PHOENIX models similar to SN 2000cb 8 days post-explosion

Model	L_{bol} 10^{41} erg/s	$B - V$ mag	$L_{(B-V)}$ 10^{41} erg/s	$B - I$ mag	$L_{(B-I)}$ 10^{41} erg/s	$V - I$ mag	$L_{(V-I)}$ 10^{41} erg/s
4.00		0.83	4.22 ± 0.44	1.314	4.27 ± 0.36	0.484	4.18 ± 0.36
4.50		0.559	4.27 ± 0.45	1.126	4.31 ± 0.37	0.567	4.52 ± 0.47

technique.

The bolometric correction luminosity technique from Bersten and Hamuy (2009) similarly over-estimates the luminosity of the 4.0×10^{41} erg s⁻¹ model and under-estimates the luminosity of the 4.5×10^{41} erg s⁻¹ model. To understand why, the photometric colors of the two models need to be compared.

Table 5.4 gives the synthetic photometry of the two PHOENIX models. The photometric colors and the corresponding bolometric luminosities using the method of Bersten and Hamuy (2009) are given in Table 5.14. Because the B -band flux is higher in the 4.50×10^{41} erg s⁻¹ model, the $B - V$ and $B - I$ colors of the model are both bluer than the other model. The process of converting these bluer colors into bolometric luminosities results in luminosities which under-estimate the true luminosity of the model for those two filter combinations.

Figure 5.11 shows the data from Table 5.7, normalized to the true luminosity of the PHOENIX model. The overall agreement between the augmented bolometric luminosity and the true luminosity of the model is excellent for all the models calculated. The general trends again hold: the quasi-bolometric luminosity

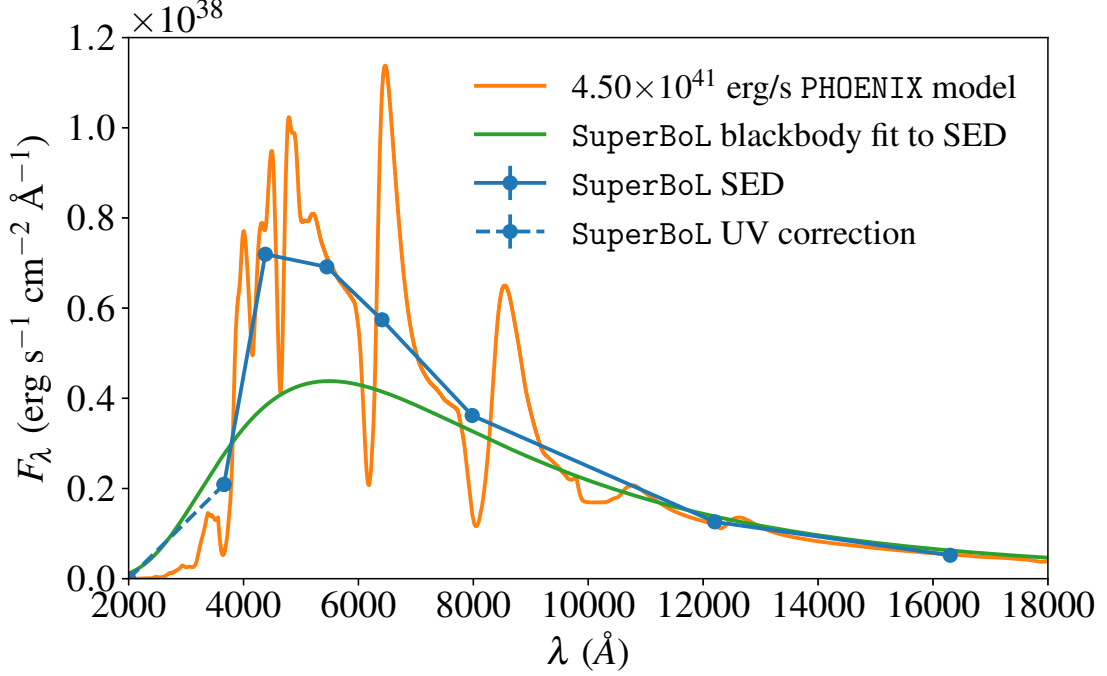


Figure 5.10 Comparison between the spectrum of the $4.50 \times 10^{41} \text{ erg s}^{-1}$ PHOENIX model with the SuperBoL-SED derived from its synthetic photometry and the blackbody fit to the fluxes of the full SED. Since the U -band flux is lower than the blackbody fit, the linear UV correction is used.

is systematically dimmer than the true luminosity by $\sim 15\%$, and the newer bolometric correction luminosities of Bersten and Hamuy (2009) are in much better agreement with the models than those of Hamuy (2001).

The next group of models are based on the spectrum of SN 2006au, about 15 days post-explosion. Both the observed spectrum and the models show more pronounced Fe II lines around 5169Å, 5018Å, and 4924Å. In addition, the Ba II 5554Å and H γ 4340Å absorption troughs appear deeper in this spectrum than in the spectra of SN 2000cb modeled at earlier times in their evolution. This is in accordance with the typical evolution of a Type II supernova spectrum, which shows more pronounced absorption of the intermediate-mass and iron-

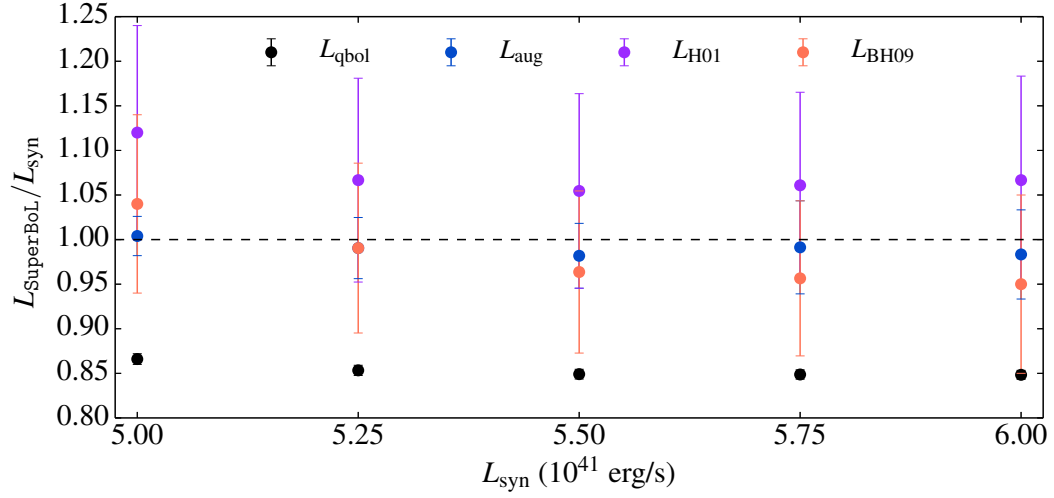


Figure 5.11 Comparison of SuperBoL-derived luminosities of PHOENIX model synthetic photometry with the luminosity of the PHOENIX model, for models similar to SN 2000cb 9 days post-explosion

peak elements as the spectrum evolves (see, e.g. Filippenko, 1997, Figure 12).

Figure 5.12 shows the data from Table 5.9, normalized as in the previous figures to the true luminosity of the PHOENIX model.

It is apparent that the bolometric luminosity estimates derived from the SN 2006au models are different from those derived from the earlier SN 2000cb models. The quasi-bolometric luminosities, while still systematically dimmer than the true luminosities, are now only $\sim 10\%$ below the true luminosities. This is likely due to the expansion and cooling of the supernova. Broadly speaking, as the effective photospheric temperature drops, more of the flux from the supernova should shift into the wavelength range covered by the synthetic bandpasses. This seems supported by the blackbody fits to the SuperBoL SED: The blackbody curve fit to the SED of the $4.50 \times 10^{41} \text{ erg s}^{-1}$ model of SN 2000cb 8 days post-

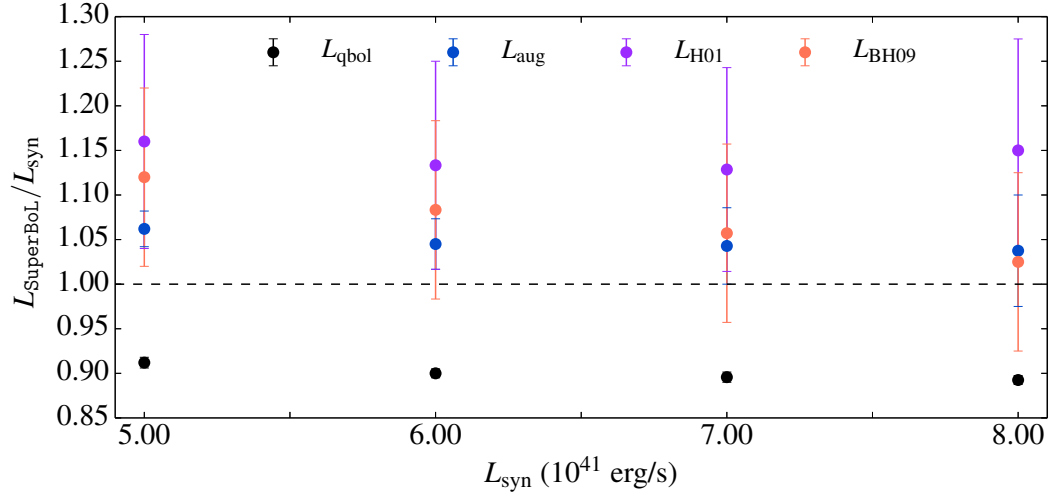


Figure 5.12 Comparison of SuperBoL-derived luminosities of PHOENIX model synthetic photometry with the luminosity of the PHOENIX model, for models similar to SN 2006au 15 days post-explosion

explosion has a temperature of 5277.2 K, while the blackbody fit to the SED of the $5.00 \times 10^{41} \text{ erg s}^{-1}$ model of SN 2006au has a temperature of 4512.5 K. It should be noted that, because these blackbody fits are made to the *entire* SED, they are not representative of the true photospheric temperature of the PHOENIX model. Line blanketing by iron-peak element in the UV causes the SED to deviate from that of a blackbody blueward of $\sim 5000\text{\AA}$. This will be examined in greater detail in section 5.5.

The model spectrum similar to SN 2006au 15 days post-explosion with a luminosity of $5.00 \times 10^{41} \text{ erg s}^{-1}$ is shown in comparison to the SuperBoL SED and the blackbody fit to the full SED in Figure 5.13.

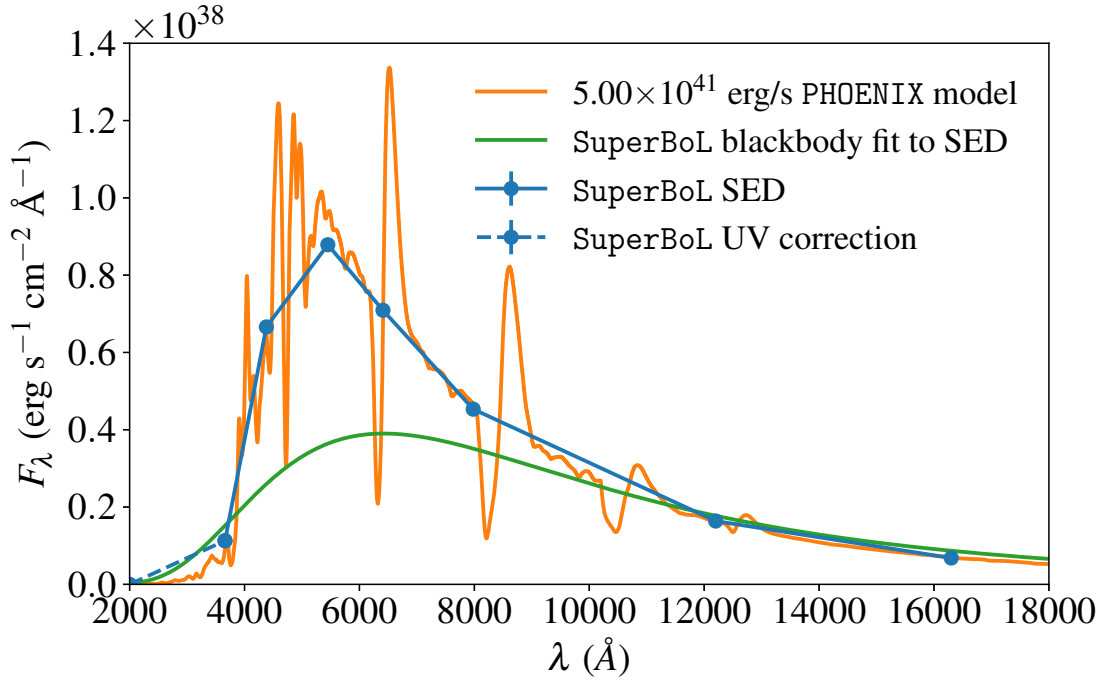


Figure 5.13 Comparison between the spectrum of the $5.00 \times 10^{41} \text{ erg s}^{-1}$ PHOENIX model with the SuperBoL-SED derived from its synthetic photometry and the blackbody fit to the fluxes of the full SED. Since the U -band flux is lower than the blackbody fit, the linear UV correction is used.

5.4.2 Plateau phase luminosities

The plateau-phase models of both SN 2000cb and SN 2006au deviated from the template observed spectra more significantly than the early phase models, evidenced by the comparisons in Figure 5.5 and Figure 5.6. The appearance of spectroscopic lines of more intermediate-mass and iron-peak elements in the spectrum which need to be treated in NLTE and the increased line blanketing in the UV all introduce additional variables and computational complexity to the PHOENIX model.

The **SuperBoL** bolometric luminosities of these models derived from the synthetic photometry also deviate from the true luminosities of the models more dramatically. Figure 5.14 shows the data from Table 5.11 normalized to the true luminosities of the underlying PHOENIX models. The general agreement between bolometric luminosity estimates and the true luminosities is good, with the clear exception of the bolometric correction luminosity of the $14.0 \times 10^{41} \text{ erg s}^{-1}$ model using the method of Bersten and Hamuy (2009). In a reversal from the previous models, the older bolometric correction technique of Hamuy (2001) actually reproduces the true luminosity of the model better than the newer technique of Bersten and Hamuy (2009). To help understand why, Figure 5.15 shows the PHOENIX spectrum compared to the **SuperBoL** SED formed from the synthetic photometry of the model spectrum, along with the blackbody flux fit to the SED.

The expansion and cooling of the supernova model have shifted the peak flux of the **SuperBoL** SED to the *R*-band. The temperature of the best-fit blackbody

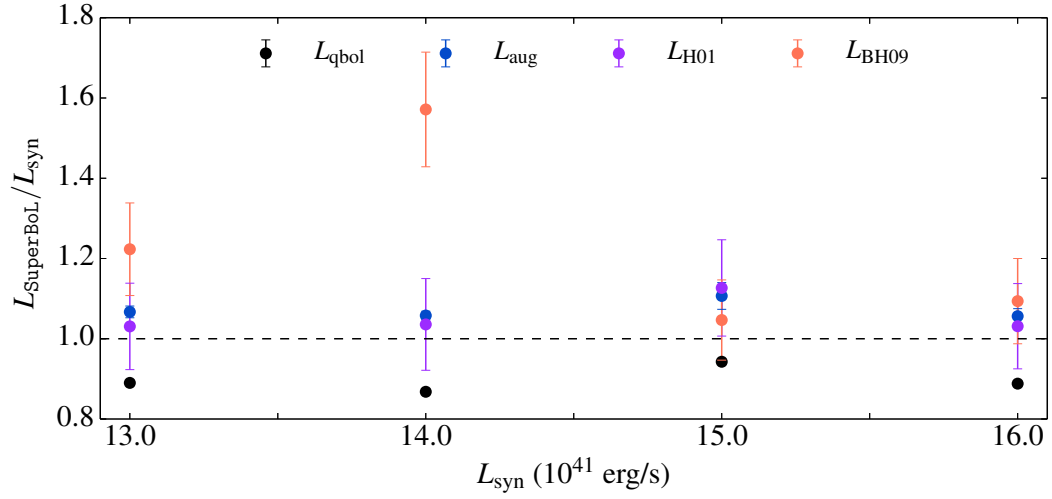


Figure 5.14 Comparison of **SuperBoL**-derived luminosities of **PHOENIX** model synthetic photometry with the luminosity of the **PHOENIX** model, for models similar to SN 2006au 57 days post-explosion

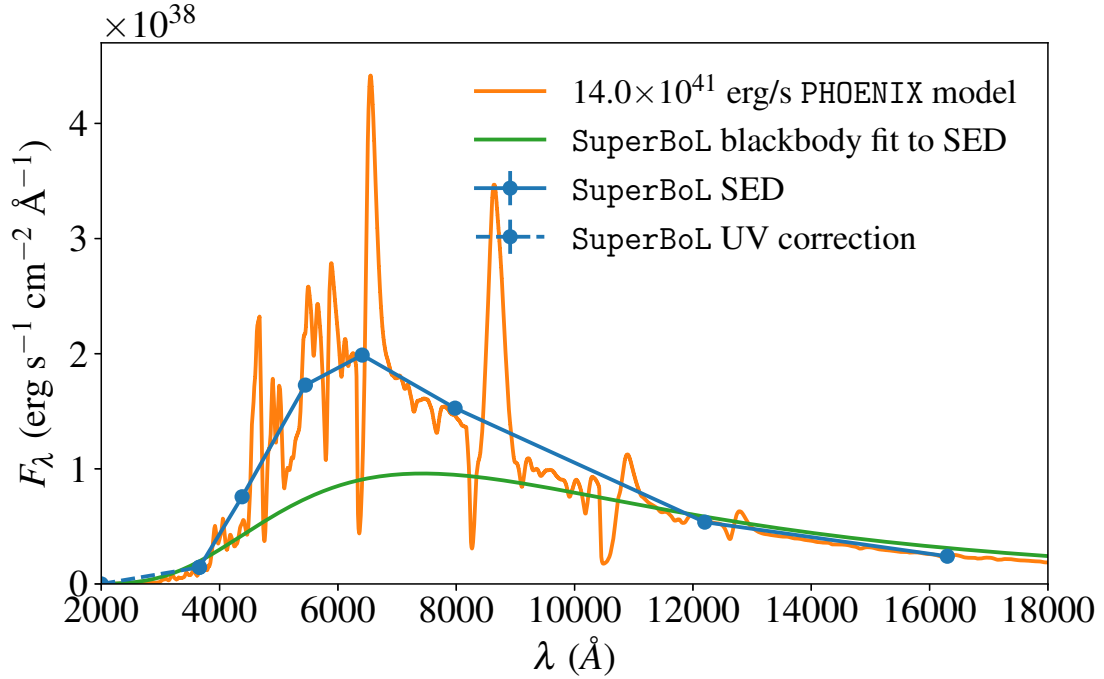


Figure 5.15 Comparison between the spectrum of the $14.0 \times 10^{41} \text{ erg s}^{-1}$ **PHOENIX** model with the **SuperBoL**-SED derived from its synthetic photometry and the blackbody fit to the fluxes of the full SED. Since the *U*-band flux is lower than the blackbody fit, the linear UV correction is used.

Table 5.15. Comparison of the luminosities derived from bolometric correction techniques using different color combinations, based on the synthetic magnitudes of two PHOENIX models similar to SN 2006au 57 days post-explosion. The $V - I$ colors fall outside the valid range of the polynomials published in Bersten and Hamuy (2009).

Model	L_{bol} 10^{41} erg/s	$B - V$ mag	$L_{(B-V)}$ 10^{41} erg/s	$B - I$ mag	$L_{(B-I)}$ 10^{41} erg/s	$V - I$ mag	$L_{(V-I)}$ 10^{41} erg/s
14.0		1.496	14.31 ± 1.65	2.633	28.74 ± 2.80	1.137	...
15.0		1.08	13.45 ± 1.41	2.202	17.96 ± 1.58	1.122	...

curve to the entire SED is 3899.3 K. In previous models, the lines connecting the SED points tracked the contours of the supernova continuum from $\sim 5000\text{\AA}$ all the way to the effective wavelength of the H -band at 16300\AA . In the plateau-phase model of SN 2000cb, this is no longer true. Between the effective wavelengths of the I -band at 7980\AA and the J -band at 12200\AA , the supernova continuum flux is noticeably lower than the SED. This is likely also tied to the lower effective temperature of the supernova photosphere shifting the peak of the continuum flux to longer wavelengths – the region between the I and J bands of the model now lies on a steeper part of the Rayleigh-Jeans tail of the continuum emission.

To understand why the bolometric correction luminosity is so high, Table 5.15 shows a comparison between the photometric colors and the corresponding bolometric luminosities of the 14.0×10^{41} erg s $^{-1}$ model and the 15.0×10^{41} erg s $^{-1}$ model using the method of Bersten and Hamuy (2009) and the synthetic photometry of the model spectra listed in Table 5.10.

The clear cause of the over-estimated bolometric correction luminosity is the

extremely high bolometric luminosity obtained through the use of the $B - I$ color. Figure 5 in Bersten and Hamuy (2009) gives a possible explanation: the extremely red $B - I$ color of the $14.0 \times 10^{41} \text{ erg s}^{-1}$ model corresponds to a bolometric correction of about -0.5 mag . On the other hand, the model's $B - V$ color of $\sim 1.5 \text{ mag}$ corresponds to a bolometric correction of about -0.25 mag . Such red colors were not evident in the well-observed template supernovae until they had already transitioned off the plateau and onto the decline to the radioactive tail. Furthermore, Bersten and Hamuy (2009) state that due to a discrepancy between the bolometric corrections derived from SN 1987A and the other two well-observed template supernovae, only the bolometric corrections from SN 1987A are used to set the polynomial after the transition off the plateau. So long as the colors of the PHOENIX model spectra are the same as that of SN 1987A, the different methods of obtaining a bolometric correction will agree on the final luminosity. Clearly, the $B - V$ and $V - I$ colors of the PHOENIX model in question differ from that of SN 1987A, and thus produce very different bolometric luminosities.

This could be a defect in the PHOENIX model, rather than a problem with the bolometric correction technique. The PHOENIX models, when compared to the observed spectrum of SN 2006au, show a clear flux deficit in the region between $5000 - 5500 \text{ \AA}$ and between $3500 - 4500 \text{ \AA}$. The fact that both regions have lower fluxes would result in lower fluxes through both the B and V filters, while the I filter remained largely unaffected. This might explain the relatively normal $B - V$ color (since the flux through both filters was lower) and the abnormally red $B - I$ and $V - I$ colors. The PHOENIX model's lower fluxes in the UV might

be evidence of more line blanketing from iron-peak elements blueward of the deep Ba II absorption line at 5554\AA than is evident in the observed spectrum.

Interestingly, Figure 11 of Taddia et al. (2012) seems to suggest that the UV flux of SN 2006au is elevated compared to that of SN 1987A in both the wavelength regions mentioned previously. This would seem to suggest that the PHOENIX models are closer matches to an SN 1987A-like spectrum than to an SN 2006au-like spectrum, in tension with the previous paragraph (since it was the photometry of SN 1987A that was used to calculate the bolometric corrections, so SN 1987A-like spectra should be the more accurately treated by the bolometric correction techniques, not less.) Further modeling will be needed to address this puzzling outlier in the bolometric luminosity data.

5.4.3 Enhanced Ca II emission in plateau-phase models of SN 2000cb

Figure 5.16 shows the data from Table 5.13, normalized to the true luminosities of the PHOENIX models from which the synthetic photometry was calculated. Compared to the results of the previous groups of models, these bolometric luminosities are outliers in this sample. As an example, for the $11.0 \times 10^{41} \text{ erg s}^{-1}$ and $12.0 \times 10^{41} \text{ erg s}^{-1}$ models, the quasi-bolometric luminosities reproduce the true luminosities of the models almost perfectly. Given the evidence shown in the previous sections, the quasi-bolometric technique should always under-estimate the luminosity of the model, making it even more curious that the quasi-bolometric luminosity of the $13.0 \times 10^{41} \text{ erg s}^{-1}$ model actually over-estimates the luminosity of the model.

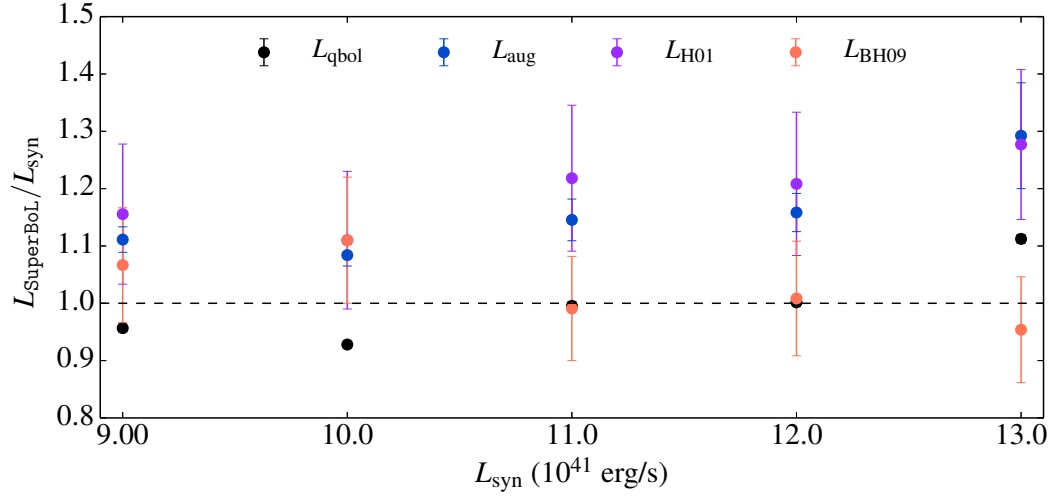


Figure 5.16 Comparison of SuperBoL-derived luminosities of PHOENIX model synthetic photometry with the luminosity of the PHOENIX model, for models similar to SN 2000cb 67 days post-explosion

To understand the cause of these strange results, Figure 5.17 shows an example of the PHOENIX model spectrum, the SuperBoL SED built from the synthetic photometry of the model, and the blackbody fit to the SED. The reason behind the high luminosity produced by the quasi-bolometric technique lies in the extremely strong Ca II emission around 8500Å in the PHOENIX model, with little associated absorption. The excess of emission is increasing the flux near the effective wavelength of the *I*-band at 7980Å, causing the contours of the SED to depart significantly from the continuum of the underlying PHOENIX model. Because of the relatively large wavelength separation between the effective wavelengths of the *V*, *I*, and *J* filters, the over-estimation of the flux in this region when integrating under the SED is enough to make-up for the missing flux blueward of the *U*- and redward of the *H*-band.

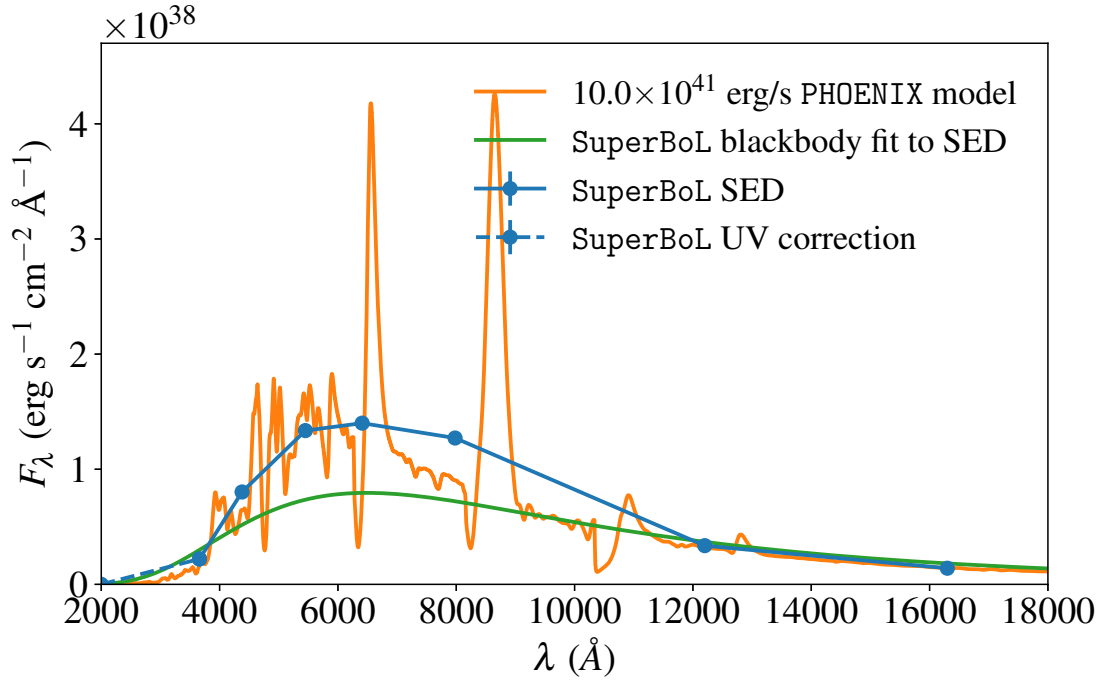


Figure 5.17 Comparison between the spectrum of the $10.0 \times 10^{41} \text{ erg s}^{-1}$ PHOENIX model with the SuperBoL-SED derived from its synthetic photometry and the blackbody fit to the fluxes of the full SED. Since the U -band flux is lower than the blackbody fit, the linear UV correction is used.

Ca II is prominent in the near-IR spectrum of Type II P supernovae (see, e.g. Filippenko, 1997, Figure 12). Unfortunately, the observed spectrum of SN 2000cb during this epoch does not extend into the near-IR for a comparison with the PHOENIX model. However, it is possible to infer whether the PHOENIX model is diverging from the observed behavior of the supernova using SuperBoL. Figure 5.18 shows the PHOENIX model and SuperBoL SED, but normalized to match the observed spectrum of SN 2000cb on JD 2451722.8 at the effective wavelength of the *V*-band (5450Å). Also shown is the observed SED of SN 2000cb, calculated from photometry taken on JD 2451721.8 (the day before the spectrum was observed) normalized to the observed spectrum in the same manner as the synthetic spectrum and SED. All observed data was corrected for reddening using the reddening law of Schlafly and Finkbeiner (2011) assuming reddening of $E(B - V) = 0.114$ and a visual extinction to reddening ratio of 3.1.

The observed SED does not show the enhanced flux in the *I*-band seen in the SuperBoL SED. This suggests that despite the excellent fit to the visible spectrum seen in Figure 5.6, the strength of the near-IR Ca II emission in the model spectrum diverges from the corresponding spectrum of SN 2000cb.

5.5 Limited bandpasses and blackbody fits

The bolometric luminosities calculated by SuperBoL in section 5.2 and section 5.3 utilized a full compliment of *UBVRIJH* synthetic photometry of various PHOENIX models created to emulate the observed spectra of SNe 2006au and 2000cb. In addition, the blackbody fits were made to the full SED. However, most supernovae

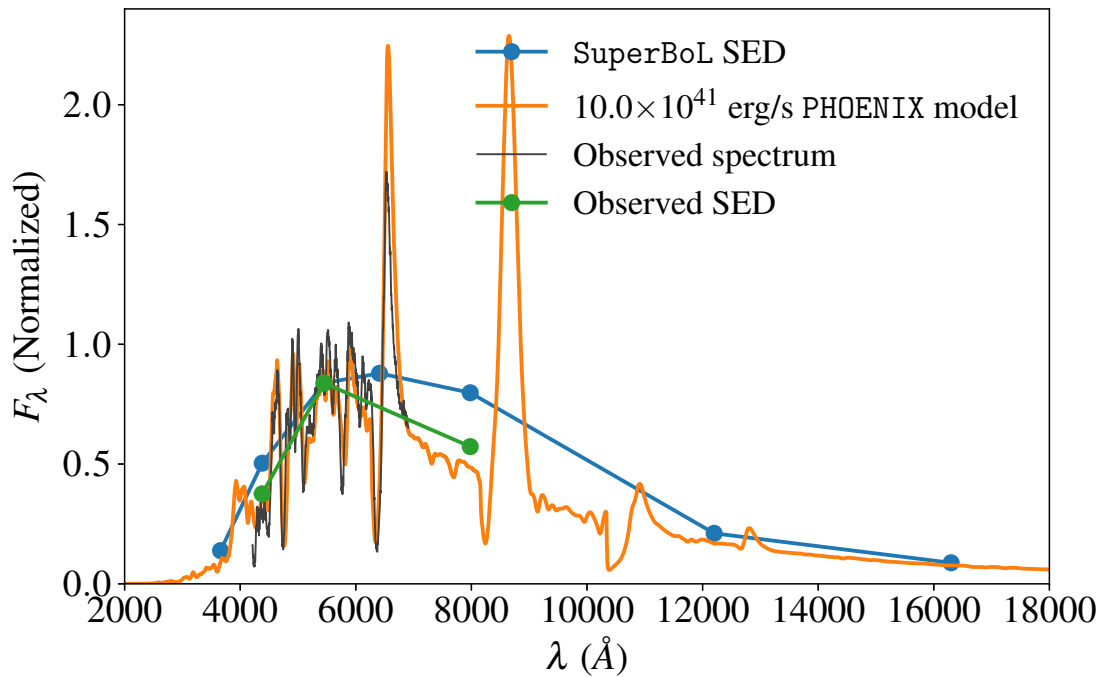


Figure 5.18 Comparison between the observed spectrum of SN 2000cb, the SED computed from contemporaneous photometry, the PHOENIX model fit to the observed spectrum with a luminosity of $10.0 \times 10^{41} \text{ erg s}^{-1}$, and the SuperBoL SED computed from synthetic photometry of the model spectrum. The slope of the observed SED from the V - to I -bands seems to indicate that the strong Ca II emission in the model was much weaker in the spectrum of SN 2000cb.

are not observed with a full compliment of photometric bandpasses on a given night. In the sections that follow, the bolometric luminosities of the PHOENIX models will be re-calculated with a smaller subset of the bandpasses, chosen to mimic the photometric bands typically used in the observation of supernovae in our sample.

For the full set of supernovae in chapter 2, IR photometry with longer effective wavelengths than the I band is uncommon. SN 1998A only has two nights of JHK photometry (Pastorello et al., 2005), while SN 2000cb has none. SNe 2006V and 2006au had better near-IR photometry: both were observed in the CSP YJH filters on 13 and 11 nights, respectively (Taddia et al., 2012). SN 2009E, like SN 2000cb, was not observed in the IR.

To reflect the scarcity of IR photometry, the J - and H -band synthetic photometry used in section 5.4 are omitted from the following analysis.

The omission of the J - and H -band fluxes from the SED leads to another complication: the fitting of a blackbody spectrum to the SED. In section 5.2 and section 5.3 the J and H bands helped to constrain the blackbody fit, ensuring that despite the inclusion of U - and B - band fluxes which typically fall well below the fluxes expected of a blackbody (due to line blanketing,) the blackbody temperature and angular radius arrived at through the fitting procedure would still prove to match the Rayleigh-Jeans tail of the model spectrum.

Without the J - and H -band fluxes, the U - and B - band fluxes have a greater influence on the temperature and angular radius of the blackbody fit, leading to fits which do not describe the supernova model spectrum redward of the photometric

SED. To address this issue, the effect of only fitting the blackbody to SED fluxes redward of 5000\AA (effectively, the V , R , and I bands) is examined in the sections below. In addition, the manner in which the UV correction is made is also tested. In subsection 3.3.2, the UV correction is made in one of three ways: if the U filter is absent from the observed photometry, the Wein tail of the blackbody fit is integrated from the bluest observed flux to $\lambda = 0$. If the U filter is present, but falls below the flux of the best fit blackbody function, then a straight line from the effective wavelength of the U filter to zero flux at $\lambda = 2000\text{\AA}$ is used to augment the observed SED in the UV region. If the U filter flux is equal to or greater than the blackbody flux, then the Wein tail of the blackbody is integrated to $\lambda = 0$. For the analysis in section 5.4, where the full compliment of $UBVRIJH$ filters were used, these criteria for calculating the UV correction proved sufficient to produce excellent agreement between the true luminosity of the supernova and the luminosity calculated using the augmented bolometric method.

However, as will be seen in the sections that follow, the omission of J , H , and often U filters means that not only must the criteria for fitting the blackbody to the SED change, but the method of calculating the UV correction must also change. Rather than default to integrating the Wein tail in the absence of the U filter, it proves necessary to also test the B -band flux against the best fit blackbody function. If the B -band falls below the blackbody flux, integrating the Wein tail leads to over-estimation of the bolometric luminosity. To remedy this, another linear interpolation of the SED is made, from the flux and effective wavelength of the B -band to zero flux at $\lambda = 2000\text{\AA}$.

5.5.1 SN 2000cb, JD 2451663.9

By omitting the J - and H -band photometry from the present analysis, the remaining bands available are $UBVRI$, representing an effective wavelength range of 3660Å to 7980Å. From this set of bands, subsets are formed to emulate the actual photometric observations that might be made of a supernova. In order to choose the combinations of bands which should be used in the analysis, it is instructive to examine which bands are used in the photometry of a relatively well-observed supernova like SN 2000cb.

There are two published sets of photometric observations made of SN 2000cb observed on JD 2451663.9, from Hamuy (2001) and Kleiser et al. (2011). Hamuy (2001) lists observations made with $UBVRI$ bands, while Kleiser et al. (2011) observed the supernova with BVI bands along with an unfiltered 'clear' observation. The photometry listed in Hamuy (2001) on JD 2451663.9 includes the U -band magnitude, but the majority of observations of SN 2000cb do not. Therefore, a third filter combination, $BVRI$ is used to represent this frequently-used subset of filters.

Table 5.16 gives the results of calculating a bolometric luminosity with subsets of the synthetic photometry listed in Table 5.4, as well as different fitting criteria for the blackbody flux used to calculate the augmented bolometric luminosity.

The quasi-bolometric luminosity, calculated by trapezoidal integration of the SED, now under-estimates the true luminosity of the supernova by a factor of 2. The omission of the U and then R bands from the set of filters used to

construct the SED only exasperates the disagreement between model luminosity and quasi-bolometric luminosity. This is to be expected, since in the quasi-bolometric method, no corrections are made for flux which falls outside the observed wavelength range of the photometry used to construct the SED.

The performance of the augmented bolometric method differs depending on the choices made in the blackbody fit criteria and the UV correction scheme. The results of the different modifications made to the augmented bolometric method are shown in Figure 5.19, which plots the luminosities in Table 5.16 normalized to the true luminosities of the models.

For the five PHOENIX models similar to SN 2000cb 8 days post-explosion, the best matches to the true luminosities of the models come when the blackbody fit to the *BVRI* or *BVI* SED is restricted to fluxes with wavelengths greater than 5000\AA ($V-I$), and the UV correction is made by a linear interpolation of the SED to zero flux at $\lambda = 2000\text{\AA}$. Interestingly, the inclusion of the *U*-filter causes an under-estimation of the bolometric luminosity. The other methods examined all over-estimate the true luminosity of the supernovae, sometimes to a large degree ($\sim 35\%$ in the case of the augmented bolometric luminosity of the $4.00 \times 10^{41} \text{ erg s}^{-1}$ model, calculated using the full *UBVRI* SED to fit the blackbody) but in most cases by $\sim 10-15\%$. To understand why the different subsets of photometric bands, different criteria for fitting the blackbody curve, and different schemes for calculating the UV correction cause these under- and over-estimations of the model luminosity, it is necessary to look at the model spectrum in comparison to the SED and blackbody curve being used to re-construct it.

Table 5.16. Comparison of **SuperBoL** bolometric luminosities from subsets of the PHOENIX synthetic photometry listed in Table 5.4.

Bands	Model L_{bol} 10^{41} erg/s	L_{qbol} 10^{41} erg/s	L_{aug} full SED 10^{41} erg/s	L_{aug} $V \rightarrow I$, BB 10^{41} erg/s	L_{aug} $V \rightarrow I$, lin 10^{41} erg/s
<i>UBVRI</i>	4.00	2.17 ± 0.02	5.47 ± 0.10	3.62 ± 0.12	3.62 ± 0.12
	4.25	2.28 ± 0.02	5.11 ± 0.15	3.91 ± 0.17	3.91 ± 0.17
	4.50	2.43 ± 0.02	5.24 ± 0.19	4.2 ± 0.2	4.2 ± 0.2
	4.75	2.58 ± 0.02	5.4 ± 0.2	4.4 ± 0.2	4.4 ± 0.2
	5.00	2.74 ± 0.02	5.6 ± 0.3	4.7 ± 0.3	4.7 ± 0.3
	MRE:	45.8×10^{-2}	20×10^{-2}	7.4×10^{-2}	7.4×10^{-2}
<i>BVRI</i>	4.00	1.94 ± 0.01	4.52 ± 0.08	5.1 ± 0.3	4.0 ± 0.7
	4.25	1.99 ± 0.01	4.70 ± 0.10	5.0 ± 0.2	4.3 ± 0.8
	4.50	2.10 ± 0.02	4.99 ± 0.11	5.2 ± 0.2	4.5 ± 0.9
	4.75	2.21 ± 0.02	5.29 ± 0.12	5.4 ± 0.2	4.8 ± 1.0
	5.00	2.32 ± 0.02	5.61 ± 0.13	5.7 ± 0.2	5.1 ± 1.0
	MRE:	53.0×10^{-2}	12×10^{-2}	17×10^{-2}	0.74×10^{-2}
<i>BVI</i>	4.00	1.93 ± 0.02	4.44 ± 0.09	5.0 ± 0.3	4.0 ± 0.7
	4.25	1.98 ± 0.02	4.65 ± 0.10	4.9 ± 0.2	4.2 ± 0.8
	4.50	2.09 ± 0.02	4.95 ± 0.11	5.1 ± 0.2	4.5 ± 0.9

Table 5.16 (cont'd)

Bands	Model L_{bol}	L_{qbol}	L_{aug} full SED	L_{aug} $V \rightarrow I$, BB	L_{aug} $V \rightarrow I$, lin
	10^{41} erg/s	10^{41} erg/s	10^{41} erg/s	10^{41} erg/s	10^{41} erg/s
	4.75	2.20 ± 0.02	5.25 ± 0.13	5.3 ± 0.2	4.8 ± 1.0
	5.00	2.32 ± 0.02	5.58 ± 0.14	5.6 ± 0.2	5.0 ± 1.0
MRE:		53.2×10^{-2}	11×10^{-2}	16×10^{-2}	0.69×10^{-2}

Figure 5.20 shows the spectrum of the $4.00 \times 10^{41} \text{ erg s}^{-1}$ PHOENIX model, compared with the SuperBoL SED constructed from the synthetic photometry and two different blackbody curves: one fit to the full SED, and the other fit only to the fluxes with wavelength longer than 5000\AA . This comparison is plotted three times, one for each of the subsets of synthetic photometry used in Table 5.16.

The top panel of Figure 5.20 reveals the reason that the augmented bolometric method over-estimates the true luminosity by such a high degree when the blackbody curve is fit the the full SED. Without the J - and H -filters to constrain the Rayleigh-Jeans tail of the blackbody, the U -band forces the temperature and angular radius of the blackbody to values that result in a very poor fit to the underlying PHOENIX model for wavelengths longer than $\sim 7000\text{\AA}$. The temperature of the blackbody fit to the entire SED is 4025 K, with an angular radius of $\theta = 1.72 \times 10^{-11}$. The integrated IR flux under this portion of the blackbody flux is responsible for the $\sim 35\%$ over-estimation of the luminosity.

When the blackbody fit is restricted to the $V - I$ bands, only, the Rayleigh-Jeans tail of the blackbody function is a much better fit to the behavior of the PHOENIX spectrum. The temperature and angular radius of the blackbody fit to

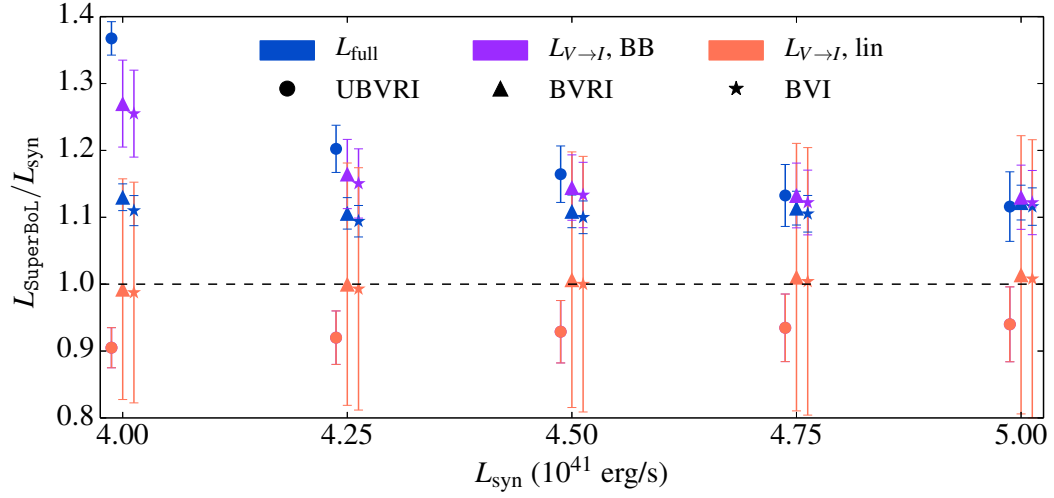


Figure 5.19 Comparison of bolometric luminosities using different subsets of the available synthetic photometry, normalized to the true luminosities of the **PHOENIX** models similar to SN 2000cb 8 days post-explosion. Data from Table 5.16. Each subset of the synthetic photometry is displaced horizontally for clarity.

only the $V - I$ bands of the $UBVRI$ SED is $T = 7500.8 \text{ K}$ and $\theta = 5.20 \times 10^{-12}$.

However, line blanketing causes the **PHOENIX** spectrum and therefore the U and B SED fluxes to fall well below the flux of a blackbody curve which fits the long-wavelength behavior of the spectrum. The U filter flux falling below the blackbody flux means that **SuperBoL** automatically uses the linear interpolation to zero flux at $\lambda = 2000 \text{ \AA}$, which explains why the last two columns of the $UBVRI$ data in Table 5.16 are always the same.

The middle panel of Figure 5.20 shows the effect of excluding the U flux from the SED. The result is a blackbody curve fit to the entire SED which is actually a better match to the long-wavelength behavior of the **PHOENIX** spectrum. The absence of the U band means that the default behavior of **SuperBoL** is to integrate the blackbody curve from the effective wavelength of the B filter to

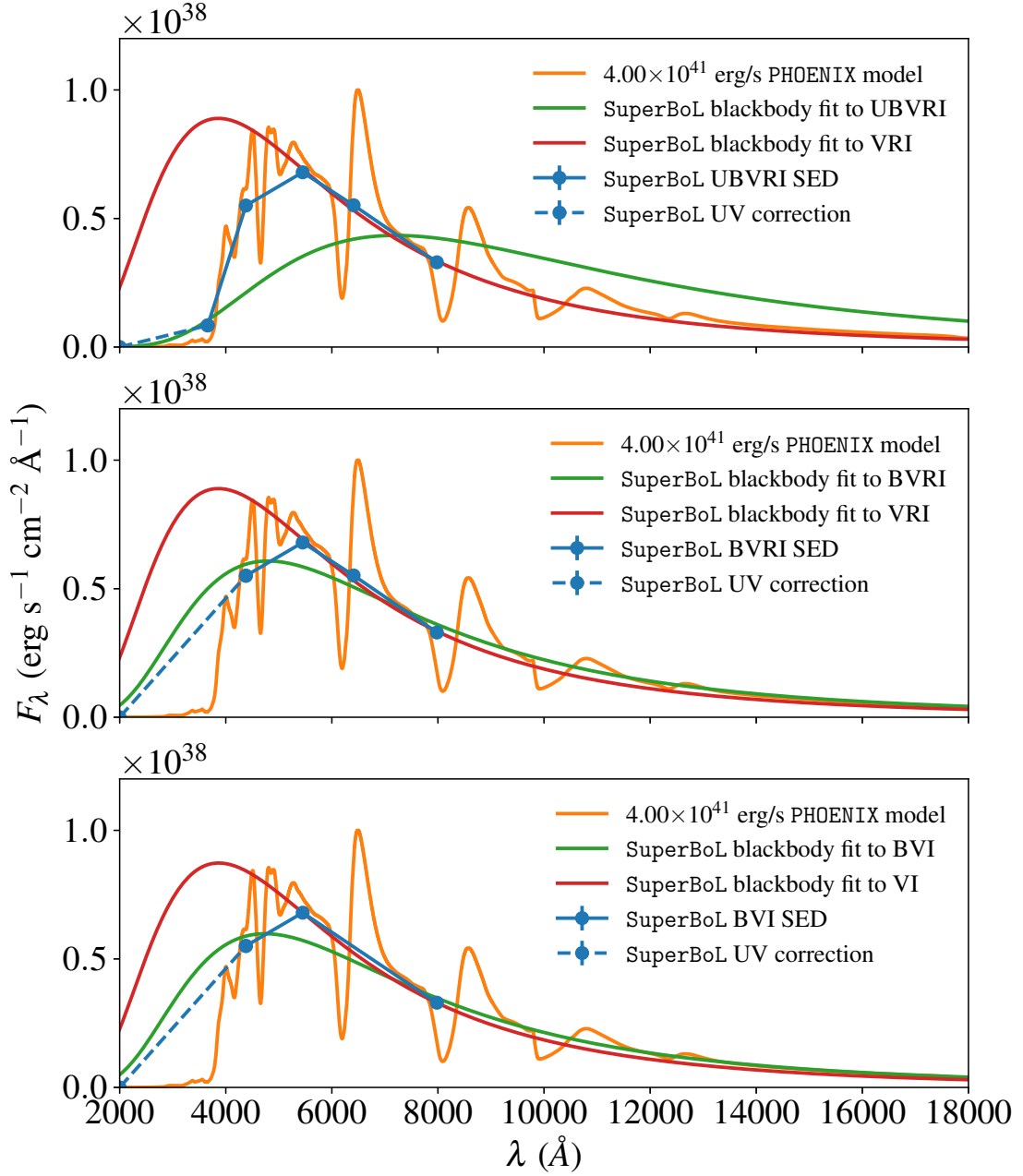


Figure 5.20 Comparison between the spectrum of the $4.00 \times 10^{41} \text{ erg s}^{-1}$ PHOENIX model with the SuperBoL-SED derived from *UBVRI* (top), *BVRI* (middle), and *BVI* (bottom) subsets of its synthetic photometry. Also shown are the blackbody fits to the fluxes of the full SED and to the *VRI* portion of the SED.

$\lambda = 0$. For the case when the blackbody is fit to the entire SED, this will result in a substantial over-estimation of the UV correction, but the effect is exaggerated if the blackbody is fit to just the V , R , and I -band fluxes. This explains why the augmented bolometric luminosities calculated in column 5 of Table 5.16 are so much higher than the luminosities calculated by other means. The more accurate blackbody fit to the long-wavelength portion of the PHOENIX model comes at the cost of dramatically over-estimating the flux at wavelengths shorter than the B -band.

The removal of the R band in the bottom panel of Figure 5.20 has little effect on the results. In fact, the temperature of the blackbody function only changes by $\sim 0.1\%$, and the angular radius by $\sim 0.7\%$.

The solution which balances the need to accurately reproduce the IR portion of the model while avoiding over-estimating the UV correction appears to be one used in the last column of Table 5.16. The agreement with the true luminosities is excellent when the U band is excluded from the photometry, and agrees to within 10% when the U band is included. The reason behind the systematic under-estimation of the luminosity when the U band is used in the SED lies not with the augmented bolometric method, but with the quasi-bolometric method. The augmented bolometric method simply adds the UV and IR corrections to the quasi-bolometric luminosity. The fact that the UV correction shown in the middle panel of Figure 5.20 is clearly too high, yet the overall luminosity is within 1% of the true value of the model indicates that the sum of the luminosity contributions from the trapezoidal integration of the SED and the integration of

the Rayleigh-Jeans tail is too low.

Although only the 4.00×10^{41} erg s⁻¹ model is shown in Figure 5.20, the results for the other models similar to SN 2000cb 8 days post-explosion are very similar, evidenced by the results shown in Figure 5.19. In the next section, the same techniques are applied to the PHOENIX models similar to SN 2006au 15 days post-explosion.

5.5.2 SN 2006au, JD 2453808.9

The same subsets of photometric bands used in subsection 5.5.1 are used in Table 5.17 to calculate the bolometric luminosities of SN 2006au-like models 15 days post-explosion, using the synthetic photometry taken from Table 5.8. The results of applying the different schemes for calculating the augmented bolometric luminosity are tabulated in Table 5.17 and shown in Figure 5.21.

The results follow much the same pattern as those in subsection 5.5.1, with the best results obtained by fitting the blackbody curve to the $V - I$ bands and using a linear interpolation from the shortest-wavelength flux in the SED to zero flux at $\lambda = 2000\text{\AA}$. Unlike the near-perfect match to the model luminosity from the previous section, the results for the models similar to SN 2006au 15 days post-explosion fall within $\pm 5\%$ of the true value, falling below the true value when the U -band flux is included in the SED, and rising above the true value when the U -band flux is excluded from the SED.

The reason for this behavior seems to stem from the overall better agreement between the SED and the PHOENIX model. The steeper density profile (see

Table 5.17. Comparison of **SuperBoL** bolometric luminosities from subsets of the **PHOENIX** synthetic photometry listed in Table 5.8, assuming a distance of 30.0 ± 0 Mpc and photometric uncertainties of 0.015 mag

Bands	Model L_{bol} 10^{41} erg/s	L_{qbol} 10^{41} erg/s	L_{aug} full SED 10^{41} erg/s	L_{aug} $V \rightarrow I$, BB 10^{41} erg/s	L_{aug} $V \rightarrow I$, lin 10^{41} erg/s
<i>UBVRI</i>	5.00	2.78 ± 0.02	7.30 ± 0.14	4.83 ± 0.17	4.83 ± 0.17
	6.00	3.36 ± 0.02	7.97 ± 0.19	5.8 ± 0.2	5.8 ± 0.2
	7.00	4.00 ± 0.03	8.6 ± 0.3	6.8 ± 0.3	6.8 ± 0.3
	8.00	4.65 ± 0.03	9.3 ± 0.5	7.9 ± 0.5	7.9 ± 0.5
	MRE:	43.2×10^{-2}	30×10^{-2}	2.9×10^{-2}	2.9×10^{-2}
<i>BVRI</i>	5.00	2.50 ± 0.02	5.92 ± 0.11	6.4 ± 0.3	5.2 ± 0.8
	6.00	2.97 ± 0.02	7.00 ± 0.14	7.5 ± 0.3	6.3 ± 1.1
	7.00	3.46 ± 0.03	8.22 ± 0.17	8.6 ± 0.4	7.4 ± 1.4
	8.00	3.93 ± 0.03	9.50 ± 0.23	9.7 ± 0.5	8.5 ± 1.8
	MRE:	50.5×10^{-2}	18×10^{-2}	24×10^{-2}	5.2×10^{-2}
<i>BVI</i>	5.00	2.51 ± 0.02	5.85 ± 0.11	6.4 ± 0.3	5.2 ± 0.8
	6.00	2.99 ± 0.03	6.97 ± 0.14	7.5 ± 0.4	6.3 ± 1.1
	7.00	3.50 ± 0.03	8.24 ± 0.19	8.7 ± 0.4	7.4 ± 1.4
	8.00	3.99 ± 0.04	9.6 ± 0.2	9.8 ± 0.5	8.5 ± 1.8
	MRE:	50.0×10^{-2}	18×10^{-2}	25×10^{-2}	5.6×10^{-2}

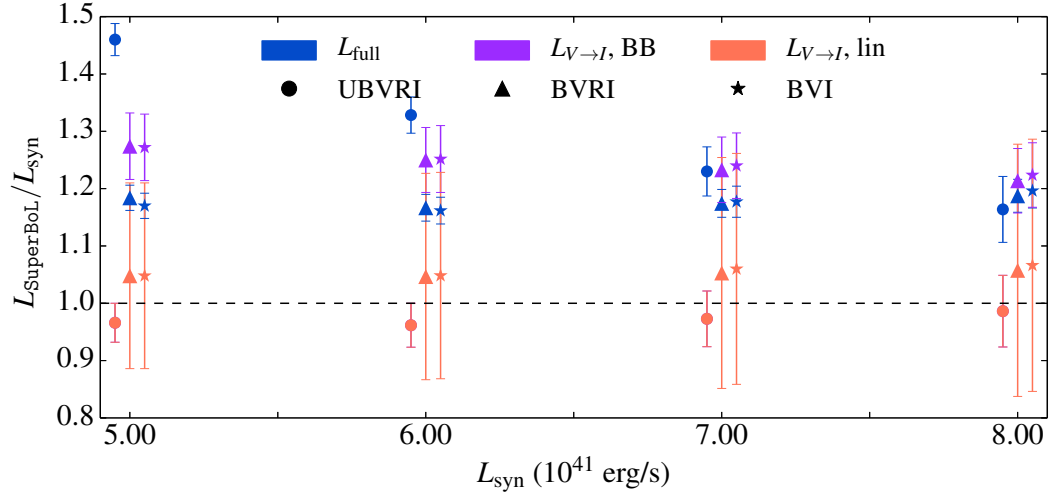


Figure 5.21 Comparison of bolometric luminosities using different subsets of the available synthetic photometry, normalized to the true luminosities of the PHOENIX models similar to SN 2006au 15 days post-explosion. Data from Table 5.17 Each subset of the synthetic photometry is displaced horizontally for clarity.

subsection 5.2.4 and longer time since explosion result in narrower emission and absorption features in the spectrum, and therefore smaller deviations from the continuum flux. The lower effective temperature of the supernova (the $V - I$ blackbody temperatures of the $5.0 \times 10^{41} \text{ erg s}^{-1}$ model of SN 2006au are $\sim 450 \text{ K}$ cooler than the effective $V - I$ blackbody temperature of the $4.0 \times 10^{41} \text{ erg s}^{-1}$ model examined in the previous section) also means that more of the model flux should fall within the wavelengths covered by the trapezoidal integration of the SED.

This seems to be supported by the results in Table 5.5 and Table 5.9, which show the quasi-bolometric luminosities of the $4.0 \times 10^{41} \text{ erg s}^{-1}$ model similar to SN 2000cb 8 days post-explosion and the $5.0 \times 10^{41} \text{ erg s}^{-1}$ model similar to SN 2006au 15 days post-explosion. The quasi-bolometric luminosity of the

SN 2006au model was only $\sim 10\%$ lower than the true luminosity, compared with the SN 2000cb model, which had a quasi-bolometric luminosity $\sim 12.5\%$ lower than the true luminosity.

Augmenting the *UBVRI* quasi-bolometric luminosity with the linear UV correction and an IR correction found using the blackbody fit to the $V - I$ results in a smaller under-estimation of the true luminosity than in the previous section. Removing the *U*-band from the SED causes a similar over-estimation of the UV correction as in the previous section, which due to the better performance of the quasi-bolometric method, leads to an over-estimation of the bolometric luminosity.

The $5.0 \times 10^{41} \text{ erg s}^{-1}$ PHOENIX model similar to SN 2006au 15 days post-explosion is shown in Figure 5.22, with the SED derived from different subsets of the available photometric bands in Table 5.17, and the blackbody fits to the full SED and the $V - I$ bands. The characteristics of the SED and blackbody fits are much the same as those shown in Figure 5.20.

The results of the previous two sections seem to suggest that calculating the augmented bolometric luminosity is most successful in recovering the true luminosity of a supernova model when the blackbody fit is made to the $V - I$ bands, and the UV correction is made using a linear interpolation to zero flux at $\lambda = 2000\text{\AA}$. However, both the models used in the previous two sections were created to match the observed spectra of early phases in the evolution of SN 2000cb and SN 2006au, before the supernovae reached maximum light. As shown in subsection 5.4.3, the models of SN 2000cb near maximum have unusually strong Ca II emission lines which limit their utility in providing realistic tests of

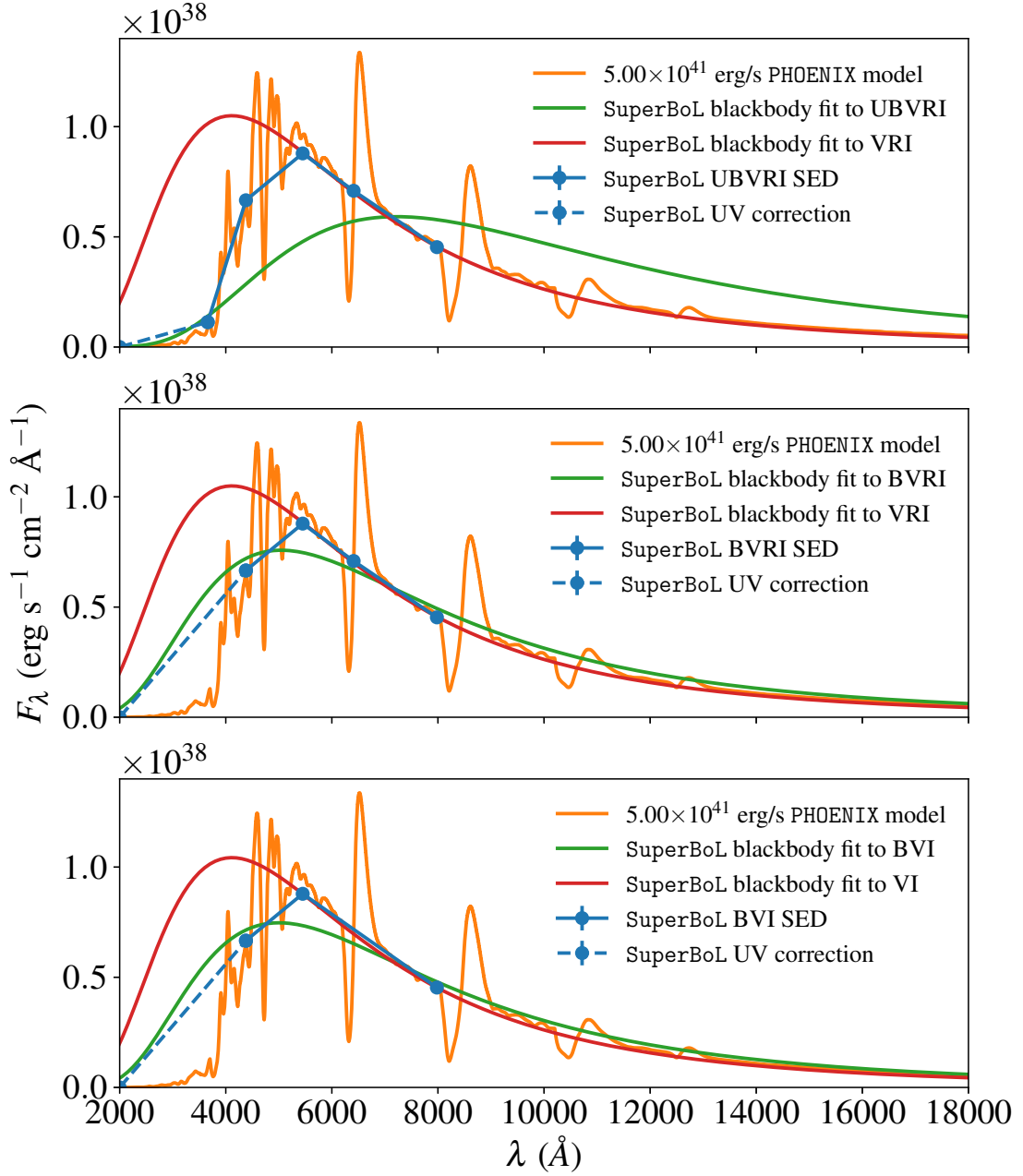


Figure 5.22 Comparison between the spectrum of the $5.00 \times 10^{41} \text{ erg s}^{-1}$ PHOENIX model with the SuperBoL-SED derived from *UBVRI* (top), *BVRI* (middle), and *BVI* (bottom) subsets of its synthetic photometry. Also shown are the blackbody fits to the fluxes of the full SED and to the *VRI* portion of the SED.

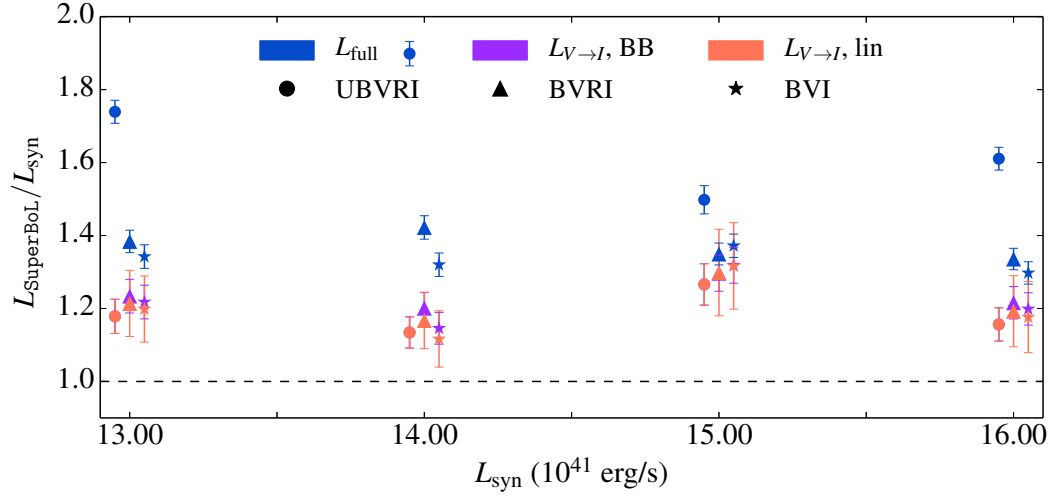


Figure 5.23 Comparison of bolometric luminosities using different subsets of the available synthetic photometry, normalized to the true luminosities of the PHOENIX models similar to SN 2006au 57 days post-explosion. Data from Table 5.18. Each subset of the synthetic photometry is displaced horizontally for clarity.

the bolometric luminosity calculation techniques. Therefore, in the next section, the plateau-phase models of SN 2006au are used to examine the characteristics of the different augmented bolometric luminosity calculation techniques.

5.5.3 SN 2006au, JD 2453850.9

The same subsets of photometric bands used in subsection 5.5.2 are used in Table 5.18 to calculate the bolometric luminosities of SN 2006au-like models 57 days post-explosion, using the synthetic photometry taken from Table 5.10. A plot of the augmented bolometric luminosities, normalized to the true luminosities of the PHOENIX models, appears in Figure 5.23.

The results of calculating the augmented bolometric luminosity of plateau-phase PHOENIX models similar to SN 2006au 57 days post-explosion are quite

Table 5.18. Comparison of **SuperBoL** bolometric luminosities from subsets of the PHOENIX synthetic photometry listed in Table 5.10, assuming a distance of 30.0 ± 0 Mpc and photometric uncertainties of 0.015 mag

Bands	Model L_{bol} 10^{41} erg/s	L_{qbol} 10^{41} erg/s	L_{aug} full SED 10^{41} erg/s	L_{aug} $V \rightarrow I$, BB 10^{41} erg/s	L_{aug} $V \rightarrow I$, lin 10^{41} erg/s
<i>UBVRI</i>	13.00	5.97 ± 0.04	22.6 ± 0.4	15.3 ± 0.6	15.3 ± 0.6
	14.00	6.20 ± 0.05	26.6 ± 0.5	15.9 ± 0.6	15.9 ± 0.6
	15.00	7.61 ± 0.05	22.5 ± 0.6	19.0 ± 0.9	19.0 ± 0.9
	16.00	7.54 ± 0.05	25.8 ± 0.5	18.5 ± 0.7	18.5 ± 0.7
	MRE:	53.0×10^{-2}	69.7×10^{-2}	18.4×10^{-2}	18.4×10^{-2}
<i>BVRI</i>	13.00	5.58 ± 0.04	18.0 ± 0.4	16.0 ± 0.6	15.8 ± 1.2
	14.00	5.87 ± 0.05	19.9 ± 0.5	16.8 ± 0.6	16.3 ± 1.1
	15.00	6.92 ± 0.05	20.2 ± 0.5	19.5 ± 0.7	19.5 ± 1.8
	16.00	7.00 ± 0.05	21.4 ± 0.5	19.5 ± 0.7	19.1 ± 1.6
	MRE:	56.3×10^{-2}	37.3×10^{-2}	23.7×10^{-2}	21.8×10^{-2}
<i>BVI</i>	13.00	5.41 ± 0.05	17.5 ± 0.4	15.8 ± 0.6	15.6 ± 1.2
	14.00	5.45 ± 0.05	18.5 ± 0.5	16.0 ± 0.6	15.6 ± 1.1
	15.00	6.93 ± 0.06	20.6 ± 0.5	19.8 ± 0.7	19.8 ± 1.8
	16.00	6.78 ± 0.06	20.8 ± 0.5	19.2 ± 0.7	18.8 ± 1.6
	MRE:	57.7×10^{-2}	33.2×10^{-2}	22.0×10^{-2}	20.2×10^{-2}

different than those of the early-phase **PHOENIX** models in the previous two sections. All of the augmented bolometric luminosities are higher than the true luminosities, in most cases by $\sim 20\%$. Furthermore, the luminosities calculated using the full SED are now systematically higher than those calculated using the $V - I$ photometry. In the early-phase models, the highest luminosities calculated using the $BVRI$ and BVI subsets were from fitting the blackbody curve to the $V - I$ photometry and performing the UV correction by integrating under the blackbody flux from the effective wavelength of the B -band to $\lambda = 0$. A clear outlier in the dataset is the augmented bolometric luminosity of the $14.0 \times 10^{41} \text{ erg s}^{-1}$ model calculated using the full SED and $UBVRI$ bands.

In order to investigate the cause of these discrepancies between the augmented bolometric luminosities calculated by **SuperBoL** and the true luminosities of the underlying **PHOENIX** models, Figure 5.24 shows a comparison between the spectrum of the $14.0 \times 10^{41} \text{ erg s}^{-1}$ **PHOENIX** model and the SED derived from its synthetic photometry, for the three subsets of photometric bands used in Table 5.18. Also shown are the blackbody fluxes fit to both the full SEDs and the $V - I$ portions of the SEDs.

The top panel of Figure 5.24 makes plain the reason for the enormously high ($L_{\text{aug}}/L_{\text{true}} \sim 1.9$) augmented bolometric luminosity obtained using the blackbody fit to the full $UBVRI$ SED. As in the early-phase models, the inclusion of the U - and B -bands in the blackbody fit causes the temperature and angular radius of the resulting blackbody to be such that the flux at wavelengths longer than the effective wavelength of the I -band over-estimates the true flux of the **PHOENIX**

model by a factor of ~ 2 . When the blackbody fit is restricted to the $V - I$ bands only, the agreement between the Rayleigh-Jeans tail and the PHOENIX model is better, but the blackbody flux is still slightly higher than the model flux.

It is likely that the cause of this disparity lies in the shape of the **SuperBoL** SED. As mentioned in subsection 5.3.1, the peak flux of the SED is now in the R -band. Unlike the early-phase models, where the V , R , and I band fluxes fell neatly along the Rayleigh-Jeans tail of the best-fit blackbody curve, in this plateau-phase model some combination of line blanketing, expansion of the model ejecta, and cooling of the effective temperature of the photosphere seem to have caused the V -band flux to depart from the blackbody curve which would fit the R - and I bands. Like all the other models tested in this chapter, the inclusion of fluxes that fall below the blackbody flux which fits the reddest observed bands in the SED causes the effective temperature of the blackbody to be lower and its angular radius to be larger than the blackbody which more accurately represents the long-wavelength behavior of the PHOENIX model. The fact that the V -band flux of the plateau-phase model seems to be departing from the continuum flux of the PHOENIX model might be the cause of the over-estimation of the bolometric luminosity when using the augmented bolometric luminosity technique.

If this explanation is correct, then the use of only the R - and I -bands in the calculation of the blackbody fit should increase the effective temperature of the blackbody, and decrease the angular radius to better match the long-wavelength model flux. To test this, Figure 5.25 shows the result of fitting the blackbody flux to only the R - and I -bands.

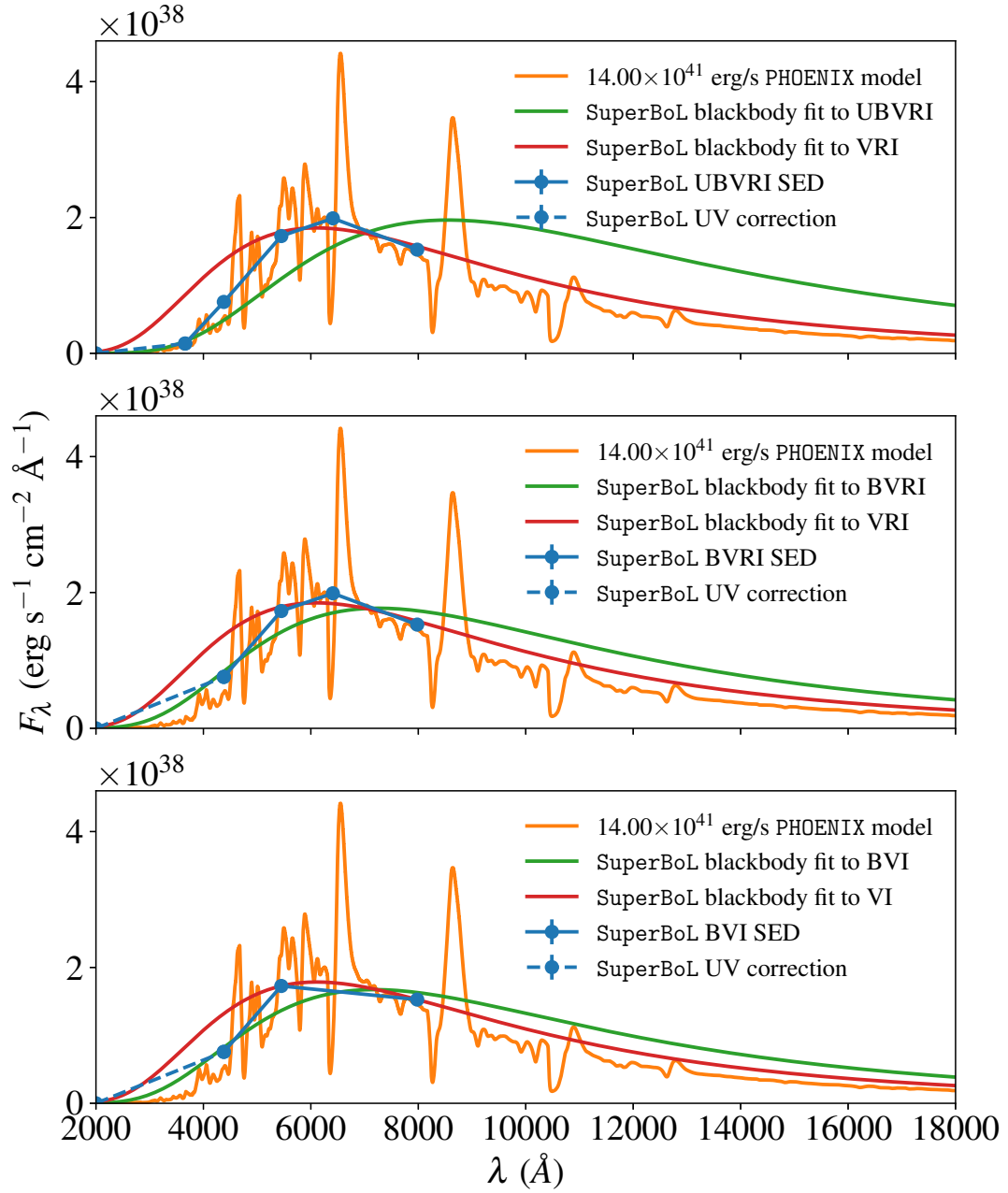


Figure 5.24 Comparison between the spectrum of the $14.00 \times 10^{41} \text{ erg s}^{-1}$ PHOENIX model with the SuperBoL-SED derived from *UBVRI* (top), *BVRI* (middle), and *BVI* (bottom) subsets of its synthetic photometry. Also shown are the blackbody fits to the fluxes of the full SED and to the *VRI* portion of the SED.

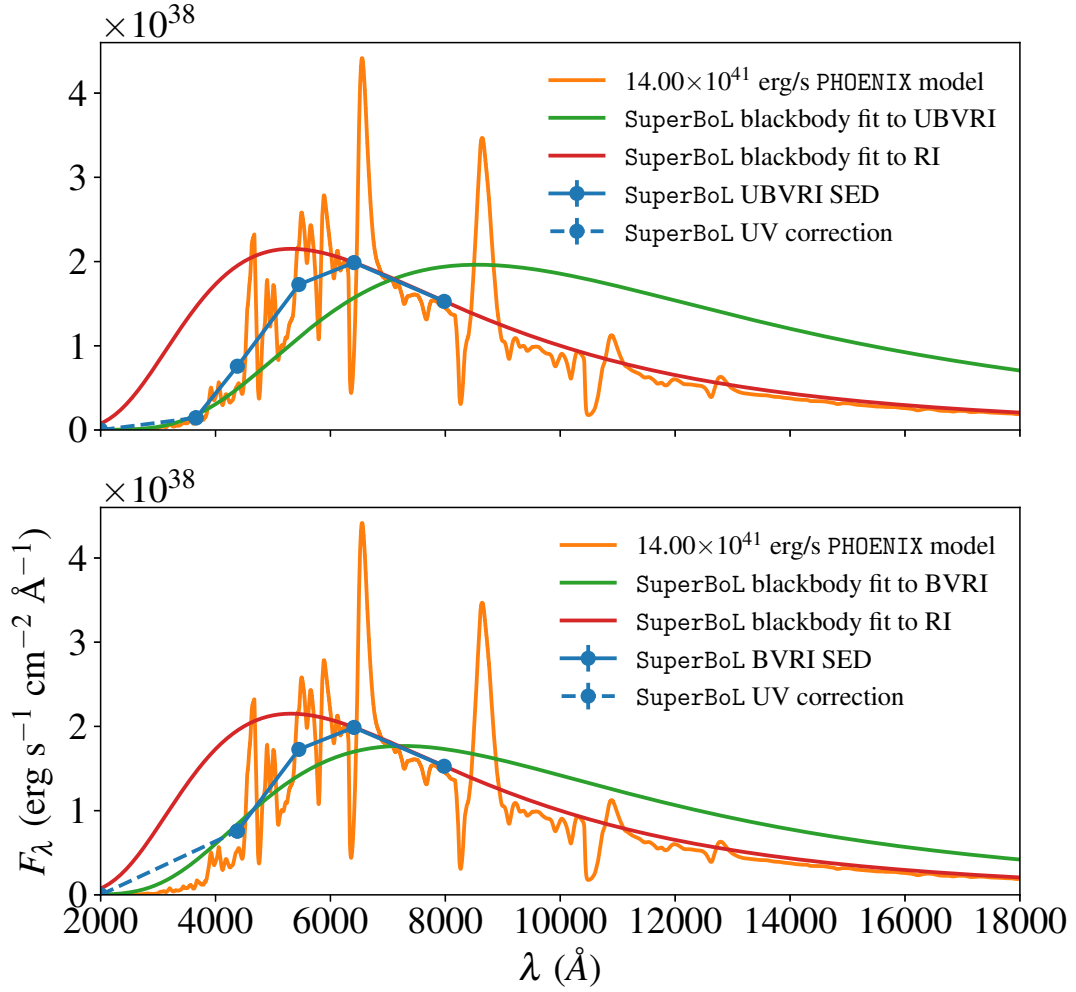


Figure 5.25 Comparison between the spectrum of the $14.00 \times 10^{41} \text{ erg s}^{-1}$ PHOENIX model with the **SuperBoL**-SED derived from *UBVRI* (top) and *BVRI* (bottom) subsets of its synthetic photometry. Also shown are the blackbody fits to the fluxes of the full SED and to the *RI* portion of the SED.

Table 5.19. Comparison of **SuperBoL** bolometric luminosities from subsets of the **PHOENIX** synthetic photometry listed in Table 5.10, assuming a distance of 46.0 ± 0 Mpc and photometric uncertainties of 0.015 mag

Bands	Model L_{bol} 10^{41} erg/s	L_{aug} $V \rightarrow I$, lin	L_{aug} $R \rightarrow I$, lin
		10^{41} erg/s	10^{41} erg/s
<i>UBVRI</i>	13.00	15.3 ± 0.6	15.2 ± 1.0
	14.00	15.9 ± 0.6	14.3 ± 1.0
	15.00	19.0 ± 0.9	20.5 ± 1.4
	16.00	18.5 ± 0.7	18.3 ± 1.2
	MRE:	18.4×10^{-2}	17.3×10^{-2}
<i>BVRI</i>	13.00	15.8 ± 1.2	15.6 ± 1.5
	14.00	16.3 ± 1.1	14.8 ± 1.3
	15.00	19.5 ± 1.8	20.5 ± 1.4
	16.00	19.1 ± 1.6	18.9 ± 1.8
	MRE:	21.8×10^{-2}	20.0×10^{-2}

As predicted, fitting the blackbody flux to the *R*- and *I*-band fluxes raises the temperature of the blackbody. In this case, the *VRI* fit temperature was 4751.9 K, while the *RI* fit temperature was 5449.3 K. The hotter blackbody results in a peak shifted to lower wavelengths and most importantly, a much improved fit to the long-wavelength portions of the **PHOENIX** model spectrum. The angular radius of the best-fit blackbody also decreased as expected, from a *VRI* angular radius of 1.53×10^{-11} to a *RI* angular radius of 1.72×10^{-11} .

The luminosities derived from the augmented bolometric luminosity technique when the blackbody is fit to the *R*- and *I*-band fluxes alone are tabulated in Table 5.19 and plotted in Figure 5.26.

The 14.0×10^{41} erg s $^{-1}$ model benefits the most from fitting the blackbody to the *R*- and *I*-band fluxes, alone. The effects are marginally beneficial for the

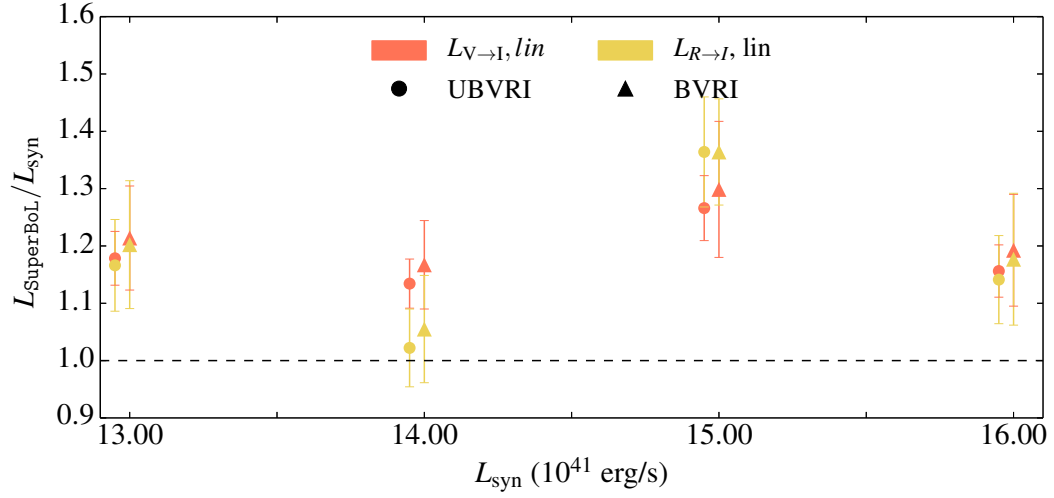


Figure 5.26 Comparison of bolometric luminosities using blackbody fits to the *VRI* and *RI* portions of the SED, for different subsets of the available synthetic photometry, normalized to the true luminosities of the **PHOENIX** models similar to SN 2006au 57 days post-explosion. Data from Table 5.18. Each subset of the synthetic photometry is displaced horizontally for clarity.

$13.0 \times 10^{41} \text{ erg s}^{-1}$ model and the $16.0 \times 10^{41} \text{ erg s}^{-1}$ model, while the augmented luminosity of the $15.0 \times 10^{41} \text{ erg s}^{-1}$ model is actually a worse fit to the true luminosity when the blackbody fit is restricted to only the *R*- and *I*-bands.

Figure 5.27 shows the **PHOENIX** model similar to SN 2006au with a luminosity of $15.0 \times 10^{41} \text{ erg s}^{-1}$, along with the SED derived from its synthetic photometry and two blackbody fits - one to the *VRI* portion of the SED, and the other to only the *RI* portion. Clearly, this model suffers from a similar problem that the plateau-phase models of SN 2000cb suffered from: a large emission feature from Ca II. It is instructive to see how this affects the augmented bolometric luminosity method: the flatter slope of the SED between the *R*- and *I*-bands requires a much lower effective temperature and larger angular radius to fit. The

effective temperature of the blackbody fit to the RI portion of the SED is 4411.5 K, compared to the 5449.3 K fit to the dimmer $14.0 \times 10^{41} \text{ erg}^{-1}$ model in Figure 5.25. This causes the IR correction, obtained from integrating the Rayleigh-Jeans tail of the blackbody flux from the effective wavelength of the I filter to $\lambda = \infty$ to be much higher than the model calls for.

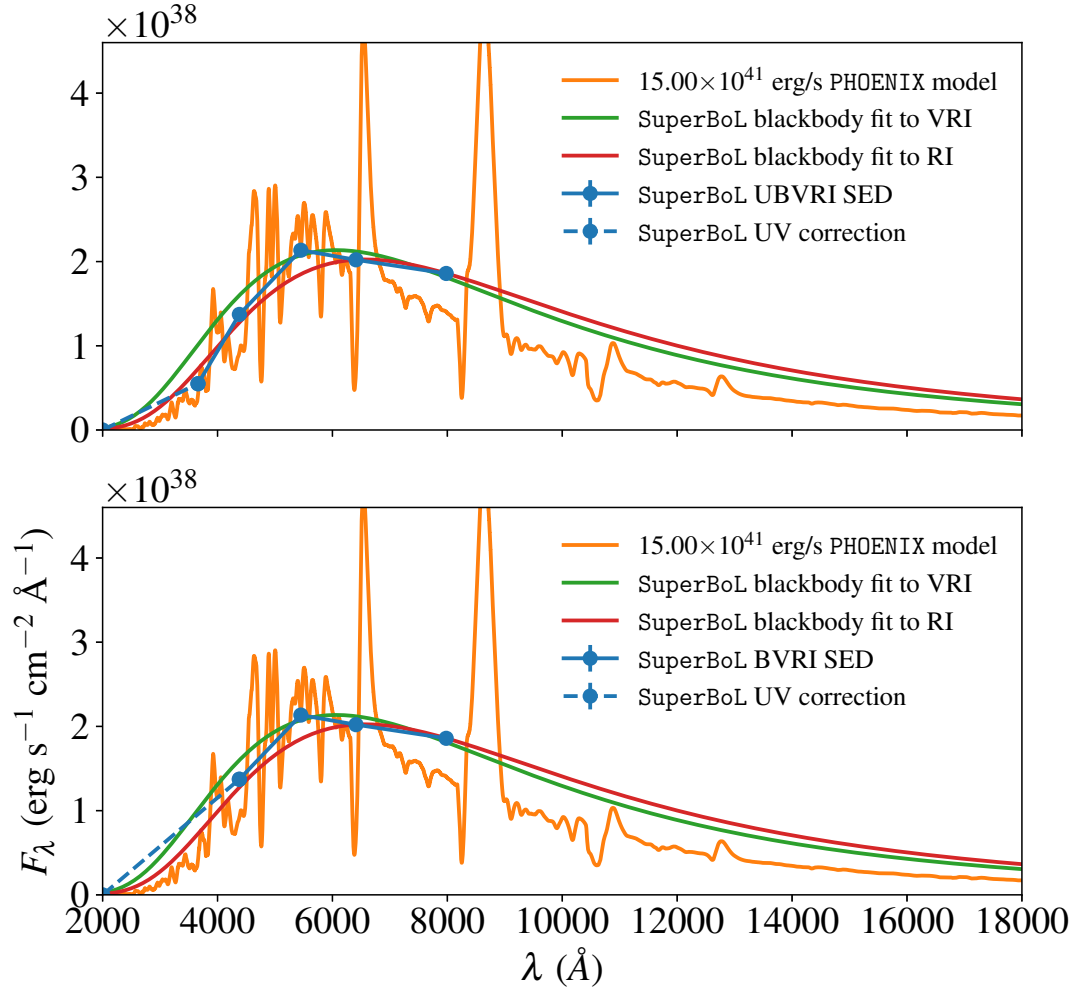


Figure 5.27 Comparison between the spectrum of the $15.00 \times 10^{41} \text{ erg}^{-1}$ PHOENIX model with the SuperBoL-SED derived from *UBVRI* (top) and *BVRI* (bottom) subsets of its synthetic photometry. Also shown are the blackbody fits to the fluxes of the *VRI* and the *RI* portion of the SED.

Chapter 6

Summary

This work has presented an analysis of several different techniques used commonly in the literature to calculate the bolometric lightcurves of supernovae from photometric observations. The focus on peculiar Type II-P supernovae comes from the fact that they are thought to share a common type of progenitor star: compact blue supergiant stars, similar to the progenitor of SN 1987A. Because SN 1987A was used as a template supernovae in the formulation of all the techniques examined in this work, supernovae which belong to the same relatively well-defined sub-class are a natural choice of objects to inter-compare the different bolometric luminosity calculation techniques.

In chapter 1, a taxonomy of different bolometric luminosity calculation techniques is presented. On one branch of this taxonomy lie the “direct integration” techniques, which convert the observed photometry into monochromatic fluxes, using the properties of the photometric bandpasses to convert magnitude to flux, and assign that flux to a wavelength representative of the bandpass. The calculation of the bolometric luminosity is accomplished by integrating between these fluxes to calculate the “quasi-bolometric” flux F_{qbol} . The quasi bolometric technique stops here, making no corrections for flux from the object which fell outside the observable range of the photometric bands used in the observations. The

“augmented” bolometric technique augments the quasi-bolometric flux with UV and IR corrections to form the augmented bolometric flux F_{aug} , typically by using a blackbody function to fit the SED constructed from the converted magnitudes. On the other side of the taxonomy lie the “bolometric correction” techniques, which do not rely on conversions from observed photometry to monochromatic flux. Instead, the bolometric properties of well-observed supernovae are used to find correlations between photometric colors and the bolometric correction required to convert an observed magnitude in a particular photometric band to the bolometric magnitude. Different bolometric correction techniques rely on different polynomial fits to the color-bolometric correction relationship for their template supernovae. To date, the literature lacks a consistent naming scheme for these different techniques.

In chapter 2, the observational data of five different supernovae (SNe 1998A, 2000cb, 2006V, 2006au, and 2009E) are presented, along with previously-published bolometric luminosities from the literature. These five objects represent the best-observed supernovae which are thought to share a common progenitor to SN 1987A. SNe 1998A, 2006V, and 2009E have very similar multi-band lightcurve shapes as the archetypal SN 1987A, though previously published luminosities of the supernovae differ. Even among this relatively small sample, there are clear differences in the photometric properties of the supernovae. SN 2000cb shows a much faster rise to peak luminosity than do the other supernovae in the sample. SN 2006au shares the slow rise to peak luminosity with the other supernovae in the sample, but seems to have shallower slopes in the early phases of its multi-band lightcurves. The

bolometric properties of the supernovae are hard to compare, because four different techniques were used in the literature to calculate the bolometric luminosities of the five different supernovae. It is therefore important to understand the differences inherent in the bolometric luminosity calculation techniques before any conclusions can be made about the true bolometric properties of the supernovae.

To facilitate that comparison, chapter 3 presents a new software package named **SuperBoL**, which was written to implement the bolometric luminosity calculation techniques in chapter 1. This tool has been written with flexibility and extensibility in mind, to maximize its utility to the supernovae research community. With **SuperBoL**, there now exists a well-tested tool to calculate bolometric luminosities in a standardized and reproducible way. In addition to the unit testing in **SuperBoL**, several different steps have been taken to validate the results of the code, by comparing to blackbody models, white dwarf models, and to the bolometric luminosity of SN 1987A, itself. In each of these cases, the true luminosity of the object is well known, and the results of **SuperBoL** can be tested against this true luminosity. Future versions of **SuperBoL** are planned, with added features like streamlined integration with the Open Supernova Catalog (Guillochon et al., 2017) for automatic retrieval of publicly-available supernova data, and additional bolometric luminosity calculation techniques from the literature.

In chapter 4, **SuperBoL** is used to calculate the bolometric luminosities of the supernovae in chapter 2 using the techniques in chapter 1. The results in chapter 4 show that the different methods used in the literature to calculate the bolometric luminosity of a supernova can differ significantly. The quasi-bolometric

technique seems to be useful only in making comparisons between two supernovae with identical wavelength coverage. As shown in the results from SN 2006au in subsection 4.2.3, the inclusion or exclusion of a bandpass can result in large variations in the resulting bolometric luminosity. The quasi-bolometric technique will produce results several times lower than those of the bolometric correction or direct integration methods. The direct integration and bolometric correction schemes were in rough agreement for these five supernovae. It should be noted that the two supernovae with the largest difference between these two methods are SN 2006V and SN 2006au — supernovae for which only the $B - V$ color could be used in the bolometric correction. In the other supernovae, the results from using all available combinations of $B - V$, $V - I$, and $B - I$ were averaged together to produce L_{BC} . It seems possible that this averaging resulted in the closer agreement between the bolometric correction results and the direct integration results.

It is apparent from our calculations that the shape of the bolometric lightcurve of SN 2000cb stands out among this sample of peculiar Type II-P supernovae. The rise time to near-maximum light is faster and the plateau-phase is broader than the other supernovae in the sample. Utrobin and Chugai (2011) hypothesized that this difference may be due to mixing of ^{56}Ni out to ejecta velocities of 8400 km s^{-1} , much farther than the modest mixing out to 3000 km s^{-1} assumed for SN 1987A. Whatever the cause of the relatively fast rise, it is an effect that is clearly not an artifact of the technique used to calculate the bolometric luminosity — the slope of the early lightcurve is steeper than the other supernovae regardless of the method used.

While the results of chapter 4 are interesting, because the true bolometric luminosities of the supernovae in chapter 2 are unknown they cannot be used to answer a fundamental question: which of the bolometric luminosity techniques most closely approximates the true luminosity of the supernova?

In order to explore this question, chapter 5 leverages the capabilities of **PHOENIX**, a powerful NLTE radiative transfer code able to simulate the full spectrum that forms from the complex interaction between radiation and matter in expanding supernova ejecta. Using relatively simple broken power-law hydrodynamic models outlined in appendix A, 26 of these **PHOENIX** spectra were constructed to closely fit 6 of the observed spectra of SN 2000cb and SN 2006au. Using synthetic photometry of the **PHOENIX** spectra, with their known bolometric luminosities, the accuracy of the different bolometric luminosity calculation techniques can be examined. This was done in two ways: first with the full set of *UBVRIJH* synthetic photometry, and secondly with subsets of the synthetic photometry chosen to more accurately represent the bandpasses available on a typical night of observation.

When the full set of synthetic *UBVRIJH* photometry is used in the analysis, the quasi-bolometric technique produces luminosities that under-estimate the true luminosity by 10% – 15%. The augmented bolometric technique performs much better, especially on early-phase models with relatively simple spectral features. The augmented bolometric luminosity reproduces the true luminosity to within 1.4% for the early-phase models of SN 2000cb. The luminosity of the early-phase model of SN 2006au is reproduced within 5%. Near the plateau, the

model of SN 2000cb exhibits an unusually strong Ca II emission feature in the near-IR, which causes the augmented bolometric technique to over-estimate the luminosity by $\approx 16\%$. The plateau-phase model of SN 2006au performs better, with an augmented bolometric luminosity $\approx 7.2\%$ higher than the true value. The bolometric correction technique of Bersten and Hamuy (2009) produces luminosities within 3% - 7% for the early phase models, and actually reproduces the luminosity of the plateau-phase models of SN 2000cb to within 5%. The poor performance of the bolometric correction technique on the plateau-phase models of SN 2006au stem from the extremely red $B - I$ color of the model, which produces an estimated luminosity $\approx 2\times$ higher than the true luminosity of the supernova.

To reflect the fact that few supernovae have extensive IR photometric observations, the bolometric luminosity calculation techniques were tested with subsets of the full synthetic photometry. The performance of the quasi-bolometric technique in these conditions is predictably worse, as more of the flux of the model lies outside the wavelength range covered by the observations. The quasi-bolometric luminosities under these conditions now under-estimate the true luminosities by between $\approx 45\% - 60\%$. Using subsets of the full synthetic photometry also reveal pitfalls in the augmented bolometric luminosity calculations. Without long-wavelength bands like J and H to constrain the blackbody fit, the line blanketing in the UV can cause the blackbody curve to have a lower temperature and larger angular radius than evidenced by the long-wavelength behavior of the PHOENIX spectrum. This causes the IR correction to be too high. This can be remedied by

fitting only the portion of the SED redward of the peak flux. In most cases, that means using the V , R , and I filters, but as the supernova expands and cools, the peak flux moves into the R band, limiting the flux points available for fitting. This produces a blackbody fit which more closely approximates the long-wavelength characteristics of the PHOENIX model. On the UV side, the luminosity calculated by the augmented bolometric technique is sensitive to the conditions imposed on the UV correction. In all cases, the luminosities of the models were reproduced most accurately when the linear extrapolation from the shortest-wavelength flux to zero flux at $\lambda = 2000\text{\AA}$ was used instead of an integration of the Wein tail. The best matches between true and calculated luminosities for the early-phase models had mean relative errors $< 1\%$ when the linear extrapolation was used and the blackbody fit was restricted to the V , R , and I bands. When the R and I bands are used to constrain the blackbody fit for the plateau-phase model of SN 2006au, the bolometric luminosity is reproduced within 20%.

The choice of bolometric luminosity calculation technique depends strongly on which bandpasses are available for analysis. The chart shown in Figure 6.1 provides an overview of which techniques most accurately reproduce the bolometric luminosities of the PHOENIX models in chapter 5.

6.1 Future Work

The future applications of SuperBoL are manifold: thanks to the efforts of the Open Supernova Catalog team (Guillochon et al., 2017) there are over 36,000 supernovae with photometric data in a format that can already be used by SuperBoL. While

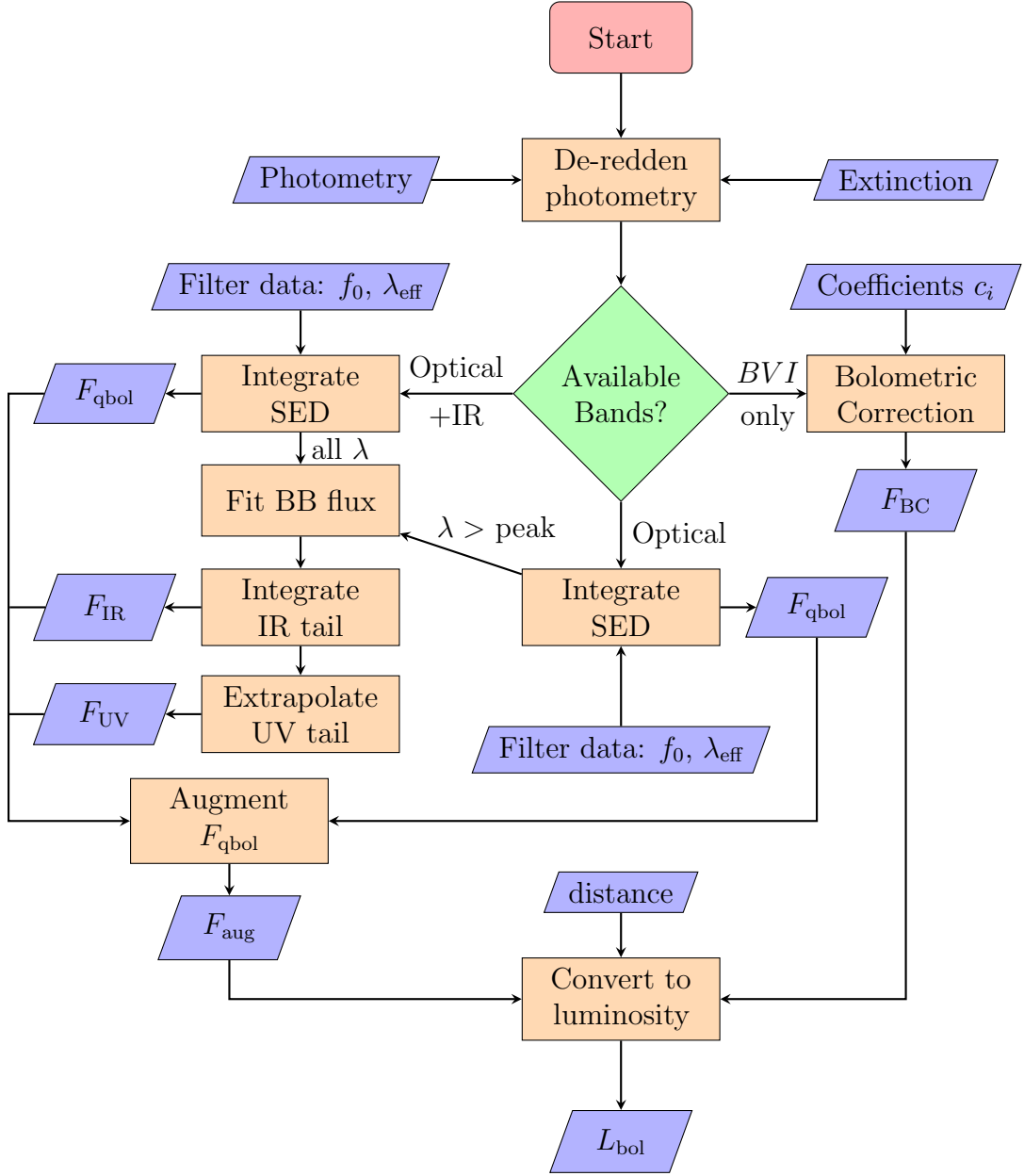


Figure 6.1 Flow chart demonstrating the application of different bolometric luminosity calculation techniques. Which technique most closely re-produces the true bolometric luminosity of a PHOENIX model depends on the available bands, as shown by the results in chapter 5.

this dissertation has focused on supernovae similar to SN 1987A, future work using Open Supernova Catalog data and **SuperBoL** will investigate how the bolometric luminosity calculation techniques examined here perform on a more diverse set of supernovae. It is likely that the quasi-bolometric and augmented bolometric methods are less sensitive to different types of supernovae than the bolometric correction method. The reason for this lies in the assumptions each technique makes about the input data. The bolometric correction methods introduced in chapter 1 are based on correlations between the colors and bolometric luminosities of well-observed template supernovae. If the intrinsic color of a supernova falls outside the pattern established by the templates, the chance of calculating an erroneous bolometric luminosity is enhanced. In the future, **SuperBoL** could provide a standard set of direct integration tools that could be used to establish the bolometric luminosities of a more diverse set of well-observed template supernovae in a reproducible way.

The ability for **SuperBoL** to propagate uncertainties through the many calculations required to output a luminosity should make it easier for hydrodynamic studies of supernova explosions to place meaningful confidence intervals on the masses, explosion energies, initial radii, and nickel masses of their models.

This work also has potential to aid in the construction of spectroscopic models using **PHOENIX**. Because **PHOENIX** uses the bolometric luminosity as an input parameter, **SuperBoL** could be used on the contemporaneous photometry of a supernova in order to estimate the bolometric luminosity, reducing the number of unconstrained parameters in the initial **PHOENIX** model. This has potential to

aid in the use of PHOENIX as a tool to perform the Spectral-Fitting Expanding Atmosphere Method (SEAM) (Mitchell, 2001). SEAM relies on fitting an observed spectrum with a synthetic spectrum generated by PHOENIX to measure the true luminosity of a supernova, and therefore determine the distance modulus to the object by comparing observed apparent magnitudes and synthetic absolute magnitudes. Because the Type II-P supernovae used by SEAM have different astrophysical origins than the Type Ia supernovae currently used for cosmological distance determination, SEAM could allow for distance estimates affected by independent systematics from the standard candle methods currently popular used.

SuperBoL should also be especially useful for exploring not-well characterized supernovae, in particular, extremely luminous supernovae (ELSNe) for both type ELSNe I/II and fast dim objects where the progenitor may or may not be a core collapse. It is our hope that our code will be improved upon in the future through contributions from the supernova community, and we welcome suggestions for improvements or new features.

6.2 Acknowledgments

This work made use of Astropy, a community-developed core Python package for Astronomy (Astropy Collaboration et al., 2013).

The work has been supported in part by support for programs HST-GO-12948.004-A was provided by NASA through a grant from the Space Telescope Science Institute, which is operated by the Association of Universities for Research

in Astronomy, Incorporated, under NASA contract NAS5-26555. This work was also supported in part by NSF grant AST-0707704, by NASA Grant NNX16AB25G and DOE Grant DE-SC0009956.

Some of the computing for this project was performed at the OU Supercomputing Center for Education & Research (OSCER) at the University of Oklahoma (OU). This research also used resources of the National Energy Research Scientific Computing Center (NERSC), which is supported by the Office of Science of the U.S. Department of Energy under Contract No. DE-AC02-05CH11231; and the Höchstleistungs Rechenzentrum Nord (HLRN). We thank both these institutions for a generous allocation of computer time.

Portions of this work have been reproduced by permission of IOP Publishing from the following publication: Lusk, Jeremy A., and E. Baron (2017). “Bolumetric Light Curves of Peculiar Type II-P Supernovae” In: *Publications of the Astronomical Society of the Pacific* 129.974 p. 044202.

Special thanks to Mario Hamuy for providing photometric data of SN 1987A, to Francesco Taddia for providing spectra of SN 2006V and SN 2006au, and to Andrea Pastorello for providing spectra of SN 1998A and SN 2009E.

Bibliography

- Anderson, Johannes (1999). “Chapter VI: Report of Divisions, Commissions, and Working Groups”. en. In: *Transactions of the International Astronomical Union* 23.2, pp. 75–254. ISSN: 0251-107X.
- Arnett, W. D. (1982). “Type I supernovae. I - Analytic solutions for the early part of the light curve”. In: *ApJ* 253, pp. 785–797. ISSN: 0004-637X.
- Arnett, W. D., D. Branch, and J. C. Wheeler (1985). “Hubble’s constant and exploding carbon-oxygen white dwarf models for Type I supernovae”. In: *Nature* 314, p. 337. ISSN: 0028-0836.
- Astropy Collaboration et al. (2013). “Astropy: A community Python package for astronomy”. In: *A&A* 558, A33. ISSN: 0004-6361.
- Baird, D. C. (1995). *Experimentation : an Introduction to Measurement Theory and Experiment Design*. 3rd. Englewood Cliffs, N.J: Prentice-Hall.
- Baron, E. et al. (1996). “Non-local thermodynamic equilibrium effects in modelling of supernovae near maximum light.” In: *MNRAS* 283, pp. 297–315. ISSN: 0035-8711.
- Bergeron, P. et al. (2011). “A Comprehensive Spectroscopic Analysis of DB White Dwarfs”. en. In: *ApJ* 737.1, p. 28. ISSN: 0004-637X.
- Bersten, Melina C. and Mario Hamuy (2009). “Bolometric Light Curves for 33 Type II Plateau Supernovae”. In: *ApJ* 701.1, pp. 200–208. ISSN: 0004-637X.
- Bessell, M. S., F. Castelli, and B. Plez (1998). “Model atmospheres broad-band colors, bolometric corrections and temperature calibrations for O - M stars”. In: *A&A* 333, pp. 231–250. ISSN: 0004-6361.
- Bethe, Hans A., John Von Neumann, and Klaus Fuchs (1947). *Blast Wave*. en. Tech. rep. Los Alamos Scientific Laboratory Report LA-2000. Google-Books-ID: lpFKmwEACAAJ. Los Alamos, NM: Martino Fine Books.
- Boles, T. (2009). “Supernova 2009E in NGC 4141”. In: *CBET* 1648, p. 1.
- Book, D. L. (1994). “The Sedov self-similar point blast solutions in nonuniform media”. en. In: *Shock Waves* 4.1, pp. 1–10. ISSN: 0938-1287, 1432-2153.
- Branch, David (1992). “The Hubble constant from nickel radioactivity in type IA supernovae”. In: *ApJ* 392, pp. 35–40. ISSN: 0004-637X.

- Buckingham, E. (1914). “On Physically Similar Systems; Illustrations of the Use of Dimensional Equations”. In: *Phys. Rev.* 4.4, pp. 345–376.
- Cardelli, Jason A., Geoffrey C. Clayton, and John S. Mathis (1989). “The relationship between infrared, optical, and ultraviolet extinction”. In: *ApJ* 345, pp. 245–256. ISSN: 0004-637X.
- Chen, Y.-T., M. Yang, and C.-S. Lin (2006). “Supernova 2006V in UGC 6510”. In: *CBET* 390, p. 1.
- Chevalier, R. A. (1976). “The hydrodynamics of Type II supernovae”. In: *The Astrophysical Journal* 207, pp. 872–887. ISSN: 0004-637X.
- Chevalier, Roger A. (1992). “Early expansion and luminosity evolution of supernovae”. In: *The Astrophysical Journal* 394, pp. 599–602. ISSN: 0004-637X.
- Chevalier, Roger A. and Claes Fransson (1992). “Pulsar nebulae in supernovae”. In: *The Astrophysical Journal* 395, pp. 540–552. ISSN: 0004-637X.
- (1994). “Emission from circumstellar interaction in normal Type II supernovae”. In: *The Astrophysical Journal* 420, pp. 268–285. ISSN: 0004-637X.
- Chevalier, Roger A. and Noam Soker (1989). “Asymmetric envelope expansion of supernova 1987A”. In: *The Astrophysical Journal* 341, pp. 867–882. ISSN: 0004-637X.
- Clocchiatti, Alejandro et al. (1996). “A Study of SN 1992H in NGC 5377”. In: *AJ* 111, p. 1286. ISSN: 0004-6256.
- Elmhamdi, Abouazza et al. (2003). “Photometry and spectroscopy of the Type IIP SN 1999em from outburst to dust formation”. In: *MNRAS* 338, pp. 939–956. ISSN: 0035-8711.
- Filippenko, Alexei V. (1997). “Optical Spectra of Supernovae”. In: *ARA&A* 35.1, pp. 309–355.
- Fiorucci, M. and U. Munari (2003). “The Asiago Database on Photometric Systems (ADPS). II. Band and reddening parameters”. In: *A&A* 401, pp. 781–796. ISSN: 0004-6361.
- Fitzpatrick, Edward L. (1999). “Correcting for the Effects of Interstellar Extinction”. In: *PASP* 111, pp. 63–75. ISSN: 0004-6280.
- Folatelli, Gastón et al. (2006). “SN 2005bf: A Possible Transition Event between Type Ib/c Supernovae and Gamma-Ray Bursts”. In: *ApJ* 641, pp. 1039–1050. ISSN: 0004-637X.
- Fukugita, M. et al. (1996). “The Sloan Digital Sky Survey Photometric System”. In: *The Astronomical Journal* 111, p. 1748. ISSN: 0004-6256.

- Gratton, Julio (1991). *Similarity and Self Similarity in Fluid Dynamics*. en. Vol. 15. Fundamentals of Cosmic Physics. Google-Books-ID: UL_0HAAACAAJ. Gordon and Breach Science Publishers.
- Guillochon, James et al. (2017). “An Open Catalog for Supernova Data”. en. In: *ApJ* 835.1, p. 64. ISSN: 0004-637X.
- Gutiérrez, Claudia P. et al. (2017). “Type II Supernova Spectral Diversity. I. Observations, Sample Characterization, and Spectral Line Evolution”. en. In: *ApJ* 850.1, p. 89. ISSN: 0004-637X.
- Hamuy, Mario (2003). “Observed and Physical Properties of Core-Collapse Supernovae”. In: *ApJ* 582, pp. 905–914. ISSN: 0004-637X.
- Hamuy, Mario Andres (2001). “Type II supernovae as distance indicators”. PhD thesis. University of Arizona.
- Hamuy, Mario and Nicholas B. Suntzeff (1990). “SN 1987A in the LMC. III - UBVRI photometry at Cerro Tololo”. In: *The Astronomical Journal* 99, pp. 1146–1158. ISSN: 0004-6256.
- Hamuy, Mario et al. (1988). “SN 1987A in the LMC - UBVRI photometry at Cerro Tololo”. In: *AJ* 95, pp. 63–83. ISSN: 0004-6256.
- Hamuy, Mario et al. (2001). “The Distance to SN 1999em from the Expanding Photosphere Method”. In: *ApJ* 558, pp. 615–642. ISSN: 0004-637X.
- Hauschildt, P. H. and E. Baron (1999). “Numerical solution of the expanding stellar atmosphere problem.” In: *JCAM* 109, pp. 41–63. ISSN: 0377-0427.
- Holberg, J. B. and Pierre Bergeron (2006). “Calibration of Synthetic Photometry Using DA White Dwarfs”. In: *AJ* 132, pp. 1221–1233. ISSN: 0004-6256.
- Imshennik, V. S. and D. V. Popov (1992). “Construction of analytical light curves of SN 1987A, taking the cooling and recombination wave into account”. In: *AZh* 69, pp. 497–515. ISSN: 0004-6299.
- Jones, Eric, Travis Oliphant, and Pearu Peterson (2001). *SciPy: Open Source Scientific Tools for Python*.
- Kamm, James R. (2000). *Evaluation of the Sedov-von Neumann-Taylor Blast Wave Solution*. English. Tech. rep. LA-UR-00-6055. Los Alamos, NM 87545 USA: Los Alamos National Laboratory, p. 42.
- Kasen, Daniel (2010). “Seeing the Collision of a Supernova with Its Companion Star”. In: *The Astrophysical Journal* 708, pp. 1025–1031. ISSN: 0004-637X.

- Kasen, Daniel et al. (2017). “Origin of the heavy elements in binary neutron-star mergers from a gravitational wave event”. In: *Nature*. arXiv: 1710.05463. ISSN: 0028-0836, 1476-4687.
- Kleiser, Io K. W. et al. (2011). “Peculiar Type II supernovae from blue supergiants”. In: *MNRAS* 415, pp. 372–382. ISSN: 0035-8711.
- Kowalski, P. M. and D. Saumon (2006). “Found: The Missing Blue Opacity in Atmosphere Models of Cool Hydrogen White Dwarfs”. In: *ApJL* 651, pp. L137–L140. ISSN: 0004-637X.
- Kynch, G. J. (1942). *The blast wave due to an intense explosion*. Tech. rep. MS No. 69. Birmingham, U.K.: Ministry of Supply.
- Landau, L. D. and E. M. Lifshitz (1987). *Fluid Mechanics*. English. 2nd edition. Vol. 6. Course of Theoretical Physics. New York: Butterworth-Heinemann. ISBN: 978-0-7506-2767-2.
- Leonard, Douglas C. and Alexei V. Filippenko (2001). “Spectropolarimetry of the Type II Supernovae 1997ds, 1998A, and 1999gi”. In: *PASP* 113.786. arXiv: astro-ph/0105295, pp. 920–936. ISSN: 0004-6280, 1538-3873.
- Lusk, Jeremy A. and E. Baron (2017). “Bolometric Light Curves of Peculiar Type II-P Supernovae”. en. In: *PASP* 129.974, p. 044202. ISSN: 1538-3873.
- Lyman, J. D., D. Bersier, and P. A. James (2014). “Bolometric corrections for optical light curves of core-collapse supernovae”. en. In: *MNRAS* 437.4, pp. 3848–3862. ISSN: 0035-8711, 1365-2966.
- Makarov, Dmitry et al. (2014). “HyperLEDA. III. The catalogue of extragalactic distances”. In: *A&A* 570, A13. ISSN: 0004-6361.
- Mamajek, E. E. et al. (2015). “IAU 2015 Resolution B2 on Recommended Zero Points for the Absolute and Apparent Bolometric Magnitude Scales”. In: *arXiv:1510.06262 [astro-ph]*. arXiv: 1510.06262.
- Michels, Thomas E (1968). *Planck functions and integrals; methods of computation*. English. NASA Technical Notes D-4446. Washington, D.C.: National Aeronautics and Space Administration.
- Mitchell, Robert Carl (2001). “Determining the distance of SN 1987A with SEAM”. en. In: *Thesis (PhD). THE UNIVERSITY OF OKLAHOMA, Source DAI-B 62/09, p. 4051, Mar 2002, 61 pages*.
- Moro, D. and U. Munari (2000). “The Asiago Database on Photometric Systems (ADPS). I. Census parameters for 167 photometric systems”. In: *A&AS* 147, pp. 361–628. ISSN: 0365-0138.

- Morozova, V. et al. (2015). “Light Curves of Core-Collapse Supernovae with Substantial Mass Loss using the New Open-Source SuperNova Explosion Code (SNEC)”. In: *ArXiv e-prints* 1505, p. 6746.
- Navasardyan, H. et al. (2009). “Supernova 2009E in NGC 4141”. In: *CBET* 1738, p. 1.
- Nitschelm, C. (1988). “Theoretical transmittance in the near UV, visible and near IR through the earth atmosphere for several observatories”. In: *A&AS* 74, pp. 67–72. ISSN: 0365-0138.
- Papenkova, M. and W. D. Li (2000). “Supernova 2000cb in IC 1158”. In: *IAUC* 7410, p. 1. ISSN: 0081-0304.
- Pastorello, A. et al. (2005). “SN 1998A: explosion of a blue supergiant”. In: *MNRAS* 360, pp. 950–962. ISSN: 0035-8711.
- Pastorello, A. et al. (2012). “SN 2009E: a faint clone of SN 1987A”. In: *A&A* 537, A141. ISSN: 0004-6361.
- Patat, Ferdinando et al. (2001). “The Metamorphosis of SN 1998bw”. In: *ApJ* 555, pp. 900–917. ISSN: 0004-637X.
- Pejcha, Ondřej and Jose L. Prieto (2015). “A Global Model of The Light Curves and Expansion Velocities of Type II-plateau Supernovae”. In: *ApJ* 799, p. 215. ISSN: 0004-637X.
- Piro, Anthony L. and Viktoriya S. Morozova (2014). “Transparent Helium in Stripped Envelope Supernovae”. In: *ApJL* 792, p. L11. ISSN: 0004-637X.
- Pritchard, T. A. et al. (2014). “Bolometric and UV Light Curves of Core-collapse Supernovae”. In: *ApJ* 787, p. 157. ISSN: 0004-637X.
- Prosperi, E. and G. M. Hurst (2009). “Supernova 2009E in NGC 4141”. In: *CBET* 1734, p. 1.
- Pumo, M. L. and L. Zampieri (2011). “Radiation-hydrodynamical Modeling of Core-collapse Supernovae: Light Curves and the Evolution of Photospheric Velocity and Temperature”. In: *ApJ* 741, p. 41. ISSN: 0004-637X.
- Pumo, M. L., L. Zampieri, and M. Turatto (2010). “Numerical calculation of sub-luminous Type II-plateau supernova events”. In: *MSAIS* 14, p. 123. ISSN: 0037-8720.
- Riess, Adam G. et al. (2011). “A 3% Solution: Determination of the Hubble Constant with the Hubble Space Telescope and Wide Field Camera 3”. In: *ApJ* 730, p. 119. ISSN: 0004-637X.

- Rogers, M. H. (1957). “Analytic Solutions for the Blast-Wave Problem with an Atmosphere of Varying Density.” In: *The Astrophysical Journal* 125, p. 478. ISSN: 0004-637X.
- Roming, Peter W. A. et al. (2005). “The Swift Ultra-Violet/Optical Telescope”. en. In: *SSRv* 120.3-4, pp. 95–142. ISSN: 0038-6308, 1572-9672.
- Sakurai, Akira (1960). “On the problem of a shock wave arriving at the edge of a gas”. en. In: *Comm. Pure Appl. Math.* 13.3, pp. 353–370. ISSN: 1097-0312.
- Schlafly, Edward F. and Douglas P. Finkbeiner (2011). “Measuring Reddening with Sloan Digital Sky Survey Stellar Spectra and Recalibrating SFD”. In: *ApJ* 737, p. 103. ISSN: 0004-637X.
- Schlegel, David J., Douglas P. Finkbeiner, and Marc Davis (1998). “Maps of Dust Infrared Emission for Use in Estimation of Reddening and Cosmic Microwave Background Radiation Foregrounds”. In: *ApJ* 500, pp. 525–553. ISSN: 0004-637X.
- Schmidt, Brian P. et al. (1993). “Photometric and spectroscopic observations of SN 1990E in NGC 1035 - Observational constraints for models of type II supernovae”. In: *AJ* 105, pp. 2236–2250. ISSN: 0004-6256.
- Sedov, L. I. (1959). *Similarity and dimensional methods in mechanics*. English. OCLC: 1188072. New York: Academic Press.
- Spiro, S. et al. (2014). “Low luminosity Type II supernovae - II. Pointing towards moderate mass precursors”. In: *MNRAS* 439, pp. 2873–2892. ISSN: 0035-8711.
- Springob, Christopher M. et al. (2009). “Erratum: ”SFI++ II: A New I-Band Tully-Fisher Catalog, Derivation of Peculiar Velocities and Data Set Properties” (2007, ApJS, 172, 599)”. In: *ApJS* 182, pp. 474–475. ISSN: 0067-0049.
- Stritzinger, Maximilian D. et al. (2011). “The Carnegie Supernova Project: Second Photometry Data Release of Low-redshift Type Ia Supernovae”. In: *AJ* 142, p. 156. ISSN: 0004-6256.
- Stritzinger, Maximilian et al. (2002). “Optical Photometry of the Type Ia Supernova 1999ee and the Type Ib/c Supernova 1999ex in IC 5179”. In: *AJ* 124, pp. 2100–2117. ISSN: 0004-6256.
- Suntzeff, Nicholas B. and Patrice Bouchet (1990). “The bolometric light curve of SN 1987A. I - Results from ESO and CTIO U to Q0 photometry”. English. In: *AJ* 99, pp. 650–663. ISSN: 0004-6256.
- Sutherland, P. G. and J. C. Wheeler (1984). “Models for Type I supernovae - Partially incinerated white dwarfs”. In: *ApJ* 280, pp. 282–297. ISSN: 0004-637X.

- Taddia, F. et al. (2012). “The Type II supernovae 2006V and 2006au: two SN 1987A-like events”. In: *A&A* 537, A140. ISSN: 0004-6361.
- Taylor, Geoffrey (1950). “The Formation of a Blast Wave by a Very Intense Explosion. II. The Atomic Explosion of 1945”. en. In: *Proceedings of the Royal Society of London A: Mathematical, Physical and Engineering Sciences* 201.1065, pp. 175–186. ISSN: 1364-5021, 1471-2946.
- Taylor, John Robert (1997). *An Introduction to Error Analysis: The Study of Uncertainties in Physical Measurements*. en. University Science Books. ISBN: 978-0-935702-75-0.
- Tremblay, P.-E., P. Bergeron, and A. Gianninas (2011). “An Improved Spectroscopic Analysis of DA White Dwarfs from the Sloan Digital Sky Survey Data Release 4”. en. In: *ApJ* 730.2, p. 128. ISSN: 0004-637X.
- Trondal, O., P. Luckas, and M. Schwartz (2006). “Supernova 2006au in UGC 11057”. In: *CBET* 426, p. 1.
- Turatto, M., S. Benetti, and E. Cappellaro (2003). en. In: *From Twilight to Highlight: The Physics of Supernovae: Proceedings of the ESO/MPA/MPE Workshop Held at Garching, Germany, 29-31 July 2002*. Ed. by Bruno Leibundgut and Wolfgang Hillebrandt. Berlin: Springer Science & Business Media, p. 200. ISBN: 978-3-540-00483-7.
- Utrobin, V. P. and N. N. Chugai (2011). “Supernova 2000cb: high-energy version of SN 1987A”. In: *A&A* 532, A100. ISSN: 0004-6361.
- van Marle, Allard Jan et al. (2010). “Numerical models of collisions between core-collapse supernovae and circumstellar shells”. In: *Monthly Notices of the Royal Astronomical Society* 407, pp. 2305–2327. ISSN: 0035-8711.
- Widger, W. K. and M. P. Woodall (1976). “Integration of the Planck Blackbody Radiation Function”. In: *BAMS* 57.10, pp. 1217–1219. ISSN: 0003-0007.
- Williams, A. et al. (1998). “Supernova 1998A in IC 2627”. In: *IAUC* 6805, p. 2. ISSN: 0081-0304.
- Woodings, Simon J. et al. (1998). “Light curves of SN 1998A and comparison with similar unusual SNe”. In: *MNRAS* 301, pp. L5–L9. ISSN: 0035-8711.
- Woosley, S. E. (1988). “SN 1987A - After the peak”. In: *The Astrophysical Journal* 330, pp. 218–253. ISSN: 0004-637X.
- Young, Timothy R. (2004). “A Parameter Study of Type II Supernova Light Curves Using 6 Msolar He Cores”. In: *ApJ* 617, pp. 1233–1250. ISSN: 0004-637X.

- Zampieri, L. et al. (2003). “Peculiar, low-luminosity Type II supernovae: low-energy explosions in massive progenitors?” In: *MNRAS* 338, pp. 711–716. ISSN: 0035-8711.
- Zel’dovich, Ya B. and Yu P. Raizer (1968). *Physics of Shock Waves and High-Temperature Hydrodynamic Phenomena*. English. Ed. by Wallace D. Hayes and Ronald F. Probstein. 1st edition. Vol. 2. New York: Academic Press.

Appendix A

Hydrodynamic Models of Type II Supernovae

In this appendix, the broken power-law hydrodynamic models first published by Chevalier and Soker (1989) and used as a basis for the PHOENIX models in chapter 5 are presented from first principles.

A.1 The Sedov-Taylor-von Neumann Blast Wave Solution

Using dimensional analysis and the concept of self-similarity, it is possible to arrive at an analytic solution to describe the problem of a finite amount of energy E_0 being released at the origin $r = 0$ of a compressible medium in spherical symmetry, with initial power-law relationship between density and radius $\rho_0 = Ar^{-\omega}$. This solution is attributed to the work of Sedov (1959), Taylor (1950), and Bethe et al. (1947), but the specific case discussed here, with a power-law density profile, is fully treated in Sedov (1959).

The density of the medium surrounding the explosion is given by

$$\rho_0 = Ar^{-\omega} \tag{A.1}$$

The gas is assumed to be an ideal, compressible fluid. The explosion is assumed to release energy E_0 instantaneously at the origin of the 1D, spherically symmetric

medium. The physical quantities of the problem are

$$r, t, p_0, E_0, A, \gamma, \omega, \quad (\text{A.2})$$

where p_0 is the initial pressure of the surrounding medium and γ is the adiabatic exponent (equal to the ratio of specific heats of the surrounding medium.)

The dimensional quantities in the problem have dimensions

$$[r] = L \quad (\text{A.3})$$

$$[t] = T \quad (\text{A.4})$$

$$[p_0] = ML^{-1}T^{-2} \quad (\text{A.5})$$

$$[E_0] = ML^2T^{-2} \quad (\text{A.6})$$

$$[A] = ML^{\omega-3} \quad (\text{A.7})$$

since γ and ω are dimensionless.

Using the Π -theorem outlined in Buckingham (1914) it should be possible to form four dimensionless combinations of the seven physical quantities listed above. Two of those dimensionless quantities are already apparent - γ and ω . The other two can be formed using the dimensionally independent quantities remaining in the list.

Taking the dimensionally independent quantities as E_0 , A and t , the following dimensionless parameters can be formed:

$$\Pi_1 = \frac{r}{E_0^{m_1} A^{m_2} t^{m_3}} \quad (\text{A.8})$$

$$\Pi_2 = \frac{p_o}{E_0^{n_1} A^{n_2} t^{n_3}} \quad (\text{A.9})$$

$$(\text{A.10})$$

Requiring that the parameters be dimensionless dictates the exponents m_1, m_2, m_3 and n_1, n_2, n_3 through the formulas

$$M^{m_1+m_2} L^{2m_1+(\omega-3)m_2} T^{m_3-2m_1} = L \quad (\text{A.11})$$

$$M^{n_1+n_2} L^{2n_1+(\omega-3)n_2} T^{n_3-2n_1} = \frac{M}{LT^2} \quad (\text{A.12})$$

$$(\text{A.13})$$

Solving the resulting systems of linear equations leads to the following exponents:

$$m_1 = \frac{1}{5 - \omega} \quad (\text{A.14})$$

$$m_2 = \frac{-1}{5 - \omega} \quad (\text{A.15})$$

$$m_3 = \frac{2}{5 - \omega} \quad (\text{A.16})$$

$$n_1 = \frac{2 - \omega}{5 - \omega} \quad (\text{A.17})$$

$$n_2 = \frac{3}{5 - \omega} \quad (\text{A.18})$$

$$n_3 = \frac{-6}{5 - \omega} \quad (\text{A.19})$$

Finally, the set of dimensionless parameters which describe the problem are given by:

$$\gamma \quad (\text{A.20})$$

$$\omega \quad (\text{A.21})$$

$$\Pi_1 = r \left(\frac{A}{E_0 t^2} \right)^{\frac{1}{5-\omega}} \quad (\text{A.22})$$

$$\Pi_2 = p_0 \left(\frac{t^6}{E_0^{2-\omega} A^3} \right)^{\frac{1}{5-\omega}} \quad (\text{A.23})$$

A.1.1 Governing Equations

The equations governing the motion of a compressible fluid in spherical symmetry, undergoing an adiabatic process with viscosity and heat conduction assumed to be negligible are the conservation equations of mass and momentum, as well as

the polytropic equation of state $P = K\rho^\gamma$, where K is a constant¹ Together, the conservation laws and the fact that K is a constant yield the set of equations

$$\frac{\partial \rho}{\partial t} + \frac{\partial(\rho v)}{\partial r} + 2\frac{\rho v}{r} = 0 \quad (\text{A.24})$$

$$\frac{\partial v}{\partial t} + v\frac{\partial v}{\partial r} + \frac{1}{\rho}\frac{\partial p}{\partial r} = 0 \quad (\text{A.25})$$

$$\frac{\partial}{\partial t} \left(\frac{p}{\rho^\gamma} \right) + v\frac{\partial}{\partial r} \left(\frac{p}{\rho^\gamma} \right) = 0., \quad (\text{A.26})$$

where Equation A.24 is the equation of continuity, Equation A.25 is the equation of motion (from momentum conservation) and Equation A.26 is the equation of constant specific entropy. The physical quantities which enter into these governing equations are the velocity v , the density ρ , and the pressure p .

A.1.2 Scale Invariants

From the set of physical quantities which enter into the governing equations, the following scale invariants can be formed.

$$V = \frac{v}{r/t} \quad (\text{A.27})$$

$$R = \frac{\rho}{A/r^\omega} \quad (\text{A.28})$$

$$P = \frac{p}{A/(r^{\omega-2}t^2)} \quad (\text{A.29})$$

¹The polytropic equation of state is a re-statement of the adiabatic equation of state $PV^\gamma = \text{constant}$, where V is the specific volume $V \equiv 1/\rho$.

A.1.3 Shock Conditions

The point explosion will introduce a discontinuity in the fluid pressure and density that propagates outward at speed c — a shock². The Rankine-Hugoniot conditions follow from conservation of mass, momentum, and energy across the discontinuity of the shock front, where ρ_0 , p_0 and v_0 represent the density, pressure, and velocity of the unshocked fluid and ρ_1 , p_1 and v_1 represent the same quantities for the fluid after the shock wave has passed. The conditions are given by

$$\rho_0(v_0 - c) = \rho_1(v_1 - c) \quad (\text{A.30})$$

$$\rho_0(v_0 - c)^2 + p_0 = \rho_1(v_1 - c)^2 + p_1 \quad (\text{A.31})$$

$$\frac{1}{2}(v_0 - c)^2 + \frac{\gamma}{\gamma - 1} \frac{p_0}{\rho_0} = \frac{1}{2}(v_1 - c)^2 + \frac{\gamma}{\gamma - 1} \frac{p_1}{\rho_1}. \quad (\text{A.32})$$

Assuming that the fluid ahead of the shock front is in hydrostatic equilibrium simplifies the shock conditions by setting $v_0 = 0$. The sound speed in the unshocked fluid is $a_0^2 = \gamma p_0 / \rho_0$. Using this, the shock conditions can be re-written as

$$-\rho_0 c = \rho_1(v_1 - c) \quad (\text{A.33})$$

$$\rho_0 \left(c^2 + \frac{a_0^2}{\gamma} \right) = \rho_1(v_1 - c)^2 + p_1 \quad (\text{A.34})$$

$$\frac{1}{2}c^2 + \frac{a_0^2}{\gamma - 1} = \frac{1}{2}(v_1 - c)^2 + \frac{\gamma}{\gamma - 1} \frac{p_1}{\rho_1}. \quad (\text{A.35})$$

²In the notation of Sedov (1959), c is the shock speed, not the speed of sound in the gas

The post-shock fluid can be characterized by v_1 , ρ_1 , and p_1 as functions of the initial density ρ_0 , the shock speed c and the sound speed in the unshocked fluid a_0 . This leads to the quadratic equation

$$\left(\frac{1}{2}c^2 + \frac{a_0^2}{\gamma-1}\right)\rho_1^2 - \left[\frac{\gamma}{\gamma-1}\left(c^2 + \frac{a_0^2}{\gamma}\right)\rho_0\right]\rho_1 + \left(\frac{\gamma}{\gamma-1} - \frac{1}{2}\right)\rho_0^2c^2 = 0. \quad (\text{A.36})$$

The roots of the quadratic equation are

$$\rho_1 = \begin{cases} \rho_0 \\ \frac{\gamma+1}{\gamma-1}\rho_0 \left(1 + \frac{2}{\gamma-1}\frac{a_0^2}{c^2}\right)^{-1} \end{cases}. \quad (\text{A.37})$$

The first root is the case in which there is no shock: the fluid density is continuous across the transition. The first root also leads to $p_0 = p_1$ and $v_0 = v_1$ when substituted into Equation A.35. The appropriate solution in the case of a supernova is the second root. When this solution is substituted into Equation A.35, the post-shock fluid velocity, density, and pressure are given by

$$\begin{aligned} v_1 &= \frac{2}{\gamma+1}c \left(1 - \frac{a_0^2}{c^2}\right) \\ \rho_1 &= \frac{\gamma+1}{\gamma-1}\rho_0 \left(1 + \frac{2}{\gamma-1}\frac{a_0^2}{c^2}\right)^{-1} \\ p_1 &= \frac{2}{\gamma+1}\rho_0c^2 \left(1 - \frac{\gamma-1}{2\gamma}\frac{a_0^2}{c^2}\right). \end{aligned} \quad (\text{A.38})$$

As the shock strength increases, terms involving the ratio a_0/c become smaller. Sedov (1959, Chapter 4, §11.1) shows that the terms in parentheses in Equation A.38 differ from 1 by less than 5 percent when $a_0/c < 0.1$. For a strong shock,

$a_0/c \ll 1$. Taking $a_0/c = 0$ in Equation A.38 is equivalent to setting $p_0 = 0$ and is the limit of a strong shock. This leads to the simplified equations

$$\begin{aligned} v_1 &= \frac{2}{\gamma + 1}c \\ \rho_1 &= \frac{\gamma + 1}{\gamma - 1}\rho_0 \\ p_1 &= \frac{2}{\gamma + 1}\rho_0 c^2. \end{aligned} \tag{A.39}$$

A.1.4 Shock Radius and Velocity

The assumption of a strong shock reduces the number of dimensionless parameters which describe the problem by one in Equation A.23. Because the outer pressure is assumed to be zero in a strong shock, the parameter Π_2 must be zero:

$$\Pi_2 = p_0 \left(\frac{t^6}{E_0^{2-\omega} A^3} \right)^{\frac{1}{5-\omega}} = 0 \tag{A.40}$$

The remaining dimensionless parameters are (where Π_1 has been renamed ξ as in Zel'dovich and Raizer (1968) to avoid confusion later with the discarded parameter Π_2 .)

$$\gamma \tag{A.41}$$

$$\omega \tag{A.42}$$

$$\xi = r \left(\frac{A}{E_0 t^2} \right)^{\frac{1}{5-\omega}}. \tag{A.43}$$

ξ is the only nondimensional variable parameter in the problem (because the ratio of specific heats γ is assumed to be fixed,) so the scale invariants V , R , and P of equations A.27 – A.29 must be functions of ξ , only.

At the position of the shock r_1 , ξ takes on the value ξ_1 . The radius of the shock at time t can be written as

$$r_1 = \xi_1 \left(\frac{E_0}{A} \right)^{\frac{1}{5-\omega}} t^{\frac{2}{5-\omega}}. \quad (\text{A.44})$$

The shock velocity c which appears in Equation A.39 is then given by the time derivative of the shock radius

$$c = \frac{dr_1}{dt} = \frac{2}{5-\omega} \frac{r_1}{t} = \frac{2}{5-\omega} \xi_1 \left(\frac{E_0}{A} \right)^{\frac{1}{5-\omega}} t^{\frac{\omega-3}{5-\omega}}. \quad (\text{A.45})$$

A.1.5 Ordinary Differential Equations

Substituting the scale invariants in equations A.27 – A.29 into the governing equations A.24 – A.26 and using Equation A.43 to transform derivatives with respect to r and t into derivatives with respect to ξ , a set of three ordinary first-order differential equations is obtained for the three unknown functions $V(\xi)$, $R(\xi)$, and $P(\xi)$ Sedov (1959).

$$\xi \left[-\frac{dV}{d\xi} + \left(\frac{2}{5-\omega} - V \right) \frac{1}{R} \frac{dR}{d\xi} \right] = -(\omega - 3)V \quad (\text{A.46})$$

$$\xi \left[\left(\frac{2}{5-\omega} - V \right) \frac{dV}{d\xi} - \frac{1}{R} \frac{dP}{d\xi} \right] = V^2 - V - (\omega - 2) \frac{P}{R} \quad (\text{A.47})$$

$$\xi \left(\frac{2}{5-\omega} - V \right) \left[\frac{1}{P} \frac{dP}{d\xi} - \frac{\gamma}{R} \frac{dR}{d\xi} \right] = -2 - [(\omega - 3)(1 - \gamma) + 1 - 3\gamma]V \quad (\text{A.48})$$

A.1.6 Boundary Conditions

The three unknown functions $V(\xi)$, $R(\xi)$, and $P(\xi)$ must satisfy the boundary conditions at the shock front $\xi = \xi_1$. At the shock, the velocity, density, and pressure are given by Equation A.39.

The scale invariant velocity at the position of the shock $V(\xi_1)$ is found by substituting the boundary condition for v_1 in Equation A.39 and the shock speed c given in Equation A.45 into the definition of the scale invariant velocity in Equation A.27

$$V(\xi_1) = \frac{4}{(\gamma + 1)(5 - \omega)} \quad (\text{A.49})$$

Similarly, the scale invariant density at the position of the shock $R(\xi_1)$ is found by combining the boundary condition for ρ_1 in Equation A.39 with the expression for the ambient density ρ_0 from Equation A.1:

$$R(\xi_1) = \frac{\gamma + 1}{\gamma - 1}. \quad (\text{A.50})$$

Lastly, the scale invariant pressure at the position of the shock $P(\xi_1)$ is given

by combining the boundary condition for p_1 in Equation A.39 with the expression for the ambient density ρ_0 from Equation A.1 and the shock speed c given in Equation A.45

$$P(\xi_1) = \frac{8}{(\gamma + 1)(5 - \omega)^2}. \quad (\text{A.51})$$

A.1.7 Energy Integral

In order to determine the state of the gas (v, ρ, p) in the post-shock flow, the system of ordinary differential equations A.48 must be integrated subject to the boundary conditions A.1.6. One integral of the system of ordinary differential equations can be found relatively easily, by making use of the fact that the energy behind the shock can be assumed to remain constant. The argument below follows the one from Landau and Lifshitz (1987, §106) and is equivalent to the energy integral formulation given in Sedov (1959, Ch. 4 §3).

The assumption of a strong shock made in subsection A.1.3 means that the energy released in the explosion E_0 is much larger than the initial internal energy of the gas. The influence of gravitational forces acting on the gas can be ignored in the case of an infinitely strong shock Sedov (1959, Ch. 5 §6), which is why the gravitational force was safely excluded from the governing equations A.24 – A.26. The consequence of these two assumptions is that the energy contained in the gas bounded by the shock is equal to the energy released in the initial explosion E_0 , and that this quantity stays constant as the shock expands.

Likewise, any sphere centered on the origin and which expands in time such

that $\xi = \xi_{\text{sp}}$ (where ξ_{sp} is some constant) at the surface of the sphere should contain within it an energy that remains constant as the sphere expands. This is because of the self-similar nature of the flow behind the shock: the distribution of velocity, density and pressure at different times will be similar, only differing by a scale factor in the radial direction. At a fixed value of $\xi = \xi_{\text{sp}}$, then, a constant fraction of the total energy E_0 will be contained in the region $0 < \xi \leq \xi_{\text{sp}}$. This sphere will expand with velocity

$$v_{\text{sp}} = \frac{2}{5 - \omega} \frac{r_{\text{sp}}}{t} \quad (\text{A.52})$$

As the sphere expands, it will lose an amount of energy equal to

$$dE_{\text{out}} = 4\pi r_{\text{sp}}^2 \rho v \left(\epsilon + \frac{p}{\rho} + \frac{1}{2} v^2 \right) dt \quad (\text{A.53})$$

in time dt . Here, ϵ represents the internal energy per unit mass of the gas.

Simultaneously, the volume of the sphere will have expanded by an amount

$$d\text{Vol} = 4\pi r_{\text{sp}}^2 v_{\text{sp}} dt. \quad (\text{A.54})$$

The energy of the additional gas contained within this volume is

$$dE_{\text{in}} = 4\pi r_{\text{sp}}^2 \rho v_{\text{sp}} \left(\epsilon + \frac{1}{2} v^2 \right) dt. \quad (\text{A.55})$$

To maintain the required constancy of the energy contained within the moving sphere, the energy lost by the gas in the sphere must be exactly balanced by the

energy gained. Equating Equation A.53 and Equation A.55, and making use of $\epsilon = \frac{1}{\gamma-1} \frac{p}{\rho}$ for a polytropic gas leads to

$$v \left(\frac{\gamma}{\gamma-1} \frac{p}{\rho} + \frac{1}{2} v^2 \right) = v_{\text{sp}} \left(\frac{1}{\gamma-1} \frac{p}{\rho} + \frac{1}{2} v^2 \right). \quad (\text{A.56})$$

In terms of the scale invariants in equations A.27 – A.29, this relation can be written

$$V \left(\frac{\gamma}{\gamma-1} \frac{P}{R} + \frac{1}{2} V^2 \right) = \frac{2}{5-\omega} \left(\frac{1}{\gamma-1} \frac{P}{R} + \frac{1}{2} V^2 \right). \quad (\text{A.57})$$

This relationship is further simplified by the introduction (following Sedov (1959, Ch. 4 §2)) of the new scale invariant

$$z = \gamma \frac{P}{R} \quad (\text{A.58})$$

related to the speed of sound in the gas. Rearranging this equation to solve for z as a function of V , produces the integral of the ordinary differential equations

$$z = \frac{1}{2} \frac{(\gamma-1)V^2 \left(\frac{2}{5-\omega} - V \right)}{V - \frac{2}{\gamma(5-\omega)}}. \quad (\text{A.59})$$

A.1.8 Phase Plane Formalism

The introduction of the function $z(V)$ in Equation A.59 allows the ordinary differential equations A.48 to be re-written in terms of the functions $z(V)$ and $V(\xi)$ as in Sedov (1959, Ch. IV §5)

$$\frac{dz}{dV} = \frac{z[2(V-1) + 3(\gamma-1)V] \left(V - \frac{2}{5-\omega}\right)}{V(V-1) \left(V - \frac{2}{5-\omega}\right) + 3 \left(\frac{2}{\gamma(5-\omega)} - V\right) z} \quad (\text{A.60})$$

$$- \frac{z \left\{ (\gamma-1)V(V-1) \left(V - \frac{2}{5-\omega}\right) + \left[2(V-1) + \frac{6}{\gamma(5-\omega)}(\gamma-1)\right] z \right\}}{\left(V - \frac{2}{5-\omega}\right) \left[V(V-1) \left(V - \frac{2}{5-\omega}\right) + 3 \left(\frac{2}{\gamma(5-\omega)} - V\right) z \right]}$$

$$\frac{d \ln \xi}{dV} = \frac{z - \left(V - \frac{2}{5-\omega}\right)^2}{V(V-1) \left(V - \frac{2}{5-\omega}\right) + 3 \left(\frac{2}{\gamma(5-\omega)} - V\right) z} \quad (\text{A.61})$$

$$\frac{d \ln R}{d \ln \xi} = \frac{1}{V - \frac{2}{5-\omega}} \left[(\omega-3)V - \frac{V(V-1) \left(V - \frac{2}{5-\omega}\right) + 3 \left(\frac{2}{\gamma(5-\omega)} - V\right) z}{z - \left(V - \frac{2}{5-\omega}\right)^2} \right] \quad (\text{A.62})$$

The full phase plane formalism of Sedov (1959) is applicable to many problems, not just the strong explosion in an environment with power-law density. In general, the system of equations A.60-A.62 is reduced by finding algebraic integrals of the system such as the energy integral Equation A.59, or integrals that come about for the mass, entropy, and momentum. Sedov (1959, Ch. IV §3) derives the forms of the analytic integrals in a general case, where the system includes the influence of gravitational forces.

Gratton (1991, §5) presents a succinct summary of the phase plane formalism. The solution to the transformed differential equations A.60-A.62 takes the form of an integral curve in the z, V plane described by an equation $z(V)$. The different solution curves represent different self-similar motions (a number of which are examined in both Sedov (1959) and Gratton (1991).)

A.1.9 Singular Point

The solution curve corresponding to the problem at hand – a strong explosion in a power-law atmosphere – is given by the energy integral in Equation A.59. When this integral is substituted into Equation A.60 subject to the boundary conditions in subsection A.1.6 the other two differential equations can be integrated by quadrature.

The differential equation A.60 has singularities given by

$$V(V-1) \left(V - \frac{2}{5-\omega} \right) + 3 \left(\frac{2}{\gamma(5-\omega)} - V \right) z = 0 \quad (\text{A.63})$$

$$\left(V - \frac{2}{5-\omega} \right) = 0. \quad (\text{A.64})$$

Replacing z in Equation A.63 with the energy integral in Equation A.59 and solving produces the coordinates of the singular point (V^*, z^*) :

$$V^* = \frac{2}{3\gamma - 1} \quad (\text{A.65})$$

$$z^* = \frac{2\gamma(\gamma-1)(3\gamma-6+\omega)}{(1+2\gamma-\omega\gamma)(3\gamma-1)^2} \quad (\text{A.66})$$

The value of ω changes the location of the singular point (V^*, z^*) along the solution curve $z(V)$ given by Equation A.59. Because the scale invariant z is related to the sound speed in the gas, it must be positive (see Equation A.58.) This restricts the solution curve to the upper half-plane $z(V) \geq 0$, and therefore

restricts values of V :

$$\frac{2}{\gamma(5-\omega)} \leq V \leq \frac{2}{5-\omega} \quad (\text{A.67})$$

The upper bound of the range is further restricted by the additional requirement that the solution curve obey the boundary conditions given in subsection A.1.6. The value of the scale invariant velocity at the location of the shock $V(\xi_1)$ is the upper bound of the solution, and lies within the range given in Equation A.67 so long as $\gamma > 1$. At the lower bound of the range given in Equation A.67, $z(V_{\min}) = \infty$. This corresponds to the origin of the spherically symmetric coordinate system ($\xi = 0$). The range of values of V for the problem at hand is then

$$\frac{2}{\gamma(5-\omega)} \leq V \leq \frac{4}{(\gamma+1)(5-\omega)}. \quad (\text{A.68})$$

The location of the singular point (V^*, z^*) changes the nature of the solutions. Kamm (2000) summarizes the three possibilities succinctly: The *standard* case, when $V(\xi_1) < V^*$, the *singular* case, when $V^* = V(\xi_1)$, and the *vacuum* case, when $V^* < V(\xi_1)$.

In the standard case, a nonzero solution exists from the shock front at $\xi = \xi_1$ to the origin of the coordinate system at $\xi = 0$, at which the pressure p is finite. The condition that $V(\xi_1) < V^*$ can be solved for a condition on the initial density power-law exponent ω , assuming the adiabatic exponent γ is constant:

$$\omega < \frac{7-\gamma}{\gamma+1}. \quad (\text{A.69})$$

In the singular case, a nonzero solution exists from the shock front to the origin of the coordinate system, but the pressure goes to zero at the origin. This corresponds to the condition that

$$\omega = \frac{7 - \gamma}{\gamma + 1}. \quad (\text{A.70})$$

In the vacuum case, an empty cavity is formed around the origin, with a nonzero solution extending from the shock front to the boundary of the empty cavity. This corresponds to the condition that

$$\frac{7 - \gamma}{\gamma + 1} < \omega. \quad (\text{A.71})$$

The solution to the differential equation A.60 is found after substituting the energy integral in Equation A.59 and applying the boundary conditions in subsection A.1.6. The relations $\xi(V)$ and $R(V)$ can then be found by quadrature, which leads to a complete solution of the problem for the original dimensional variables r , v , ρ , and p . Such analytic solutions appeared in the literature in Sedov (1959, Ch. IV §14) as well as Rogers (1957) and Kynch (1942, using Lagrangian coordinates).

A.1.10 Singular Case Solution

In the singular case, the self-similar solution is particularly simple. It was also the basis of the broken power-law model developed for the analysis of Type II-P supernova hydrodynamics in Chevalier (1976). In the case of a radiation-dominated

$\gamma = 4/3$ gas, the value of ω in the singular case takes on the value $\omega = 17/7$. This was found to be a good fit to the outer density distribution of the hydrogen-helium envelope of the progenitor to SN 1987A (Woosley, 1988, Figure 3).

The singular point (V^*, z^*) coincides with the location of the shock $(V(\xi_1), z(\xi_1))$. Because the location of the shock is a constant in the dimensionless variable ξ , the solution to the differential equation A.60 is given by the constants

$$V(\xi) = \frac{2}{3\gamma - 1} \quad (\text{A.72})$$

$$z(\xi) = \frac{2\gamma(\gamma - 1)}{(3\gamma - 1)^2}. \quad (\text{A.73})$$

Substituting the two constants (Equation A.72 and Equation A.73) as well as the singular-case definition of ω given in Equation A.70 into the differential equation A.62 yields the greatly simplified differential equation

$$\frac{d \ln R}{d \ln \xi} = \frac{8}{\gamma + 1}; \quad (\text{A.74})$$

which when solved subject to the boundary condition given in Equation A.50 gives the equation for the scale invariant density

$$R(\xi) = \frac{\gamma + 1}{\gamma - 1} \xi^{\frac{8}{\gamma + 1}}. \quad (\text{A.75})$$

The scale invariant pressure $P(\xi)$ follows immediately from the definition of $z(\xi) = \gamma P/R$:

$$P(\xi) = \frac{2(\gamma + 1)}{(3\gamma - 1)^2} \xi^{\frac{8}{\gamma+1}}. \quad (\text{A.76})$$

The solution in terms of the original dimensional variables according to the scale invariants in equations A.27 – A.29 is given by

$$v = \frac{2}{3\gamma - 1} \frac{r}{t} \quad (\text{A.77})$$

$$\rho = \frac{\gamma + 1}{\gamma - 1} A r^{-\frac{7-\gamma}{\gamma+1}} \xi^{\frac{8}{\gamma+1}}. \quad (\text{A.78})$$

$$p = \frac{2(\gamma + 1)}{(3\gamma - 1)^2} \frac{A}{t^2} r^{-\frac{5-3\gamma}{\gamma+1}} \xi^{\frac{8}{\gamma+1}}. \quad (\text{A.79})$$

A more compact solution can be written in terms of the boundary conditions Equation A.39.

$$\frac{v}{v_1} = \frac{\xi}{\xi_1} \quad (\text{A.80})$$

$$\frac{\rho}{\rho_1} = \frac{\xi}{\xi_1} \quad (\text{A.81})$$

$$\frac{p}{p_1} = \left(\frac{\xi}{\xi_1} \right)^3 \quad (\text{A.82})$$

A.1.11 Determining ξ_1

The value of the dimensionless variable parameter at the location of the shock was called ξ_1 in subsection A.1.4. The numerical value of this dimensionless variable parameter is found by enforcing energy conservation behind the shock.

As in subsection A.1.7, the energy released in the explosion E_0 is assumed to be much larger than the initial internal energy of the gas. Ignoring the influence of gravitational forces for an infinitely strong shock means that the energy contained in the gas behind the shock is constant and equal to the energy released in the explosion E_0 .

The energy contained in the gas behind the shock is given by the sum of the kinetic and internal energies of the gas.

$$E_0 = \int_0^{r_1} \frac{\rho v^2}{2} 4\pi r^2 dr + \int_0^{r_1} \frac{p}{\gamma - 1} 4\pi r^2 dr \quad (\text{A.83})$$

For the standard and singular cases, the solution is nonzero all the way to the origin of the coordinate system. For the vacuum case, the lower bound of the integral in Equation A.83 can be changed to the radius of the “hole” in the gas centered around the origin. In order to determine the numerical quantity of ξ_1 required to satisfy the conservation of energy, the integral in Equation A.83 needs to be transformed into the dimensionless variable parameter ξ using the definition of ξ given in Equation A.43 along with the solutions in equations A.77 – A.79. The upper limit of the integral will now be ξ_1 .

In the singular case, the dimensionless form of Equation A.83 becomes

$$E_0 = 8\pi \frac{\gamma + 1}{\gamma - 1} \frac{E_0}{(3\gamma - 1)^2} \int_0^{\xi_1} \xi^5 d\xi + 8\pi \frac{\gamma + 1}{\gamma - 1} \frac{E_0}{(3\gamma - 1)^2} \int_0^{\xi_1} \xi^5 d\xi, \quad (\text{A.84})$$

which reduces to the relation

$$\xi_1 = \left[\frac{3}{8\pi} \frac{\gamma - 1}{\gamma + 1} (3\gamma - 1)^2 \right]^{1/6}. \quad (\text{A.85})$$

It is common in the literature (Taylor, 1950; Sedov, 1959; Chevalier, 1976; Chevalier and Soker, 1989; Gratton, 1991; Book, 1994) to define $\xi_1 = 1$. This necessitates the introduction of an additional dimensionless constant α which is defined by $\alpha = E_0/E$. The definition of E_0 is as above – the total energy released in the explosion, but it is the constant E which appears in the definitions of the dimensionless parameters given in Equation A.10. In this formulation of the problem, it is the parameter α which must be determined by the integral in Equation A.83 (though Chevalier and Soker (1989) use $\beta = 1/\alpha$.) In the singular case, the parameters α and ξ_1 in the two formulations are related by

$$\xi_1 = \left(\frac{1}{\alpha} \right)^{1/6}. \quad (\text{A.86})$$

A.2 Broken Power-Law Ejecta

In section A.1, the theory of a blastwave expanding outward in an optically-thick power-law atmosphere is developed. This theory was used by Chevalier (1976) as the basis for a numerical exploration of hydrodynamic models of supernova explosions and the evolution of supernova lightcurves. Later work by (Chevalier and Soker, 1989) examined what happens to the Sedov-Taylor-von Neumann blast wave as it transitions from the optically-thick power-law envelope to the

optically-thin atmosphere. They find that in the limit of large time and distance from the origin, the density distribution of the ejecta should resemble a “broken” power-law: a shallow power-law at low velocity joined at a transitional velocity to a steeper power-law at higher velocities.

A.2.1 Propagation through the atmosphere

Chevalier and Soker (1989) consider two example structures for the thin atmosphere in the outer portion of the presupernova star – an exponential density distribution and a power-law of the form $\rho = k_1 x^\beta$, where $x = r - r_*$ is the distance measured inward from the outer edge of the star r_* , and k_1 and β are constants. Both of these structures are considered to be plane-parallel, a reasonable assumption given the small extent of the atmosphere compared to the radius of a typical presupernova star. Previous work has examined the self-similar motions of shock waves through plane-parallel atmosphere with both exponential (see, e.g. Zel’dovich and Raizer, 1968, Part XII §25) and power-law (Sakurai, 1960; Zel’dovich and Raizer, 1968, Part XII §11) density distributions. Chevalier and Soker (1989) find that self-similar solutions in both structures tend toward free expansion in the limit of large time and distance from the origin.

Most importantly for the analysis to follow, Chevalier and Soker (1989) find that self-similar solutions in both cases tend toward steep power-law forms in the limit of large time and distance from the origin.

A.2.2 Rarefaction wave

The arrival of the blast wave at the surface of the star, and the subsequent expansion of the envelope into a vacuum launches a rarefaction wave into the expanding envelope gas at the sound speed c_s :

$$c_s^2 = \gamma \frac{p}{\rho}. \quad (\text{A.87})$$

Chevalier and Soker (1989) describe how this rarefaction wave affects the density distribution of the expanding envelope gas: The radius of the rarefaction wave will evolve in time according to

$$\frac{dr_r}{dt} = v - c_s, \quad (\text{A.88})$$

where r_r is the position of the rarefaction wave. For $r < r_r$, the blast wave is unaffected by the rarefaction wave, and is still described by the original dimensional variables given in equations A.77 – A.79. Therefore, by substituting the pressure p from Equation A.79 and density ρ from Equation A.78 into Equation A.87, the local sound speed can be written in terms of the envelope gas velocity v by the simple relation:

$$c_s = \frac{\sqrt{2}}{3} v. \quad (\text{A.89})$$

Substituting this expression into Equation A.88 gives the differential equation

$$\frac{dr_r}{dt} = \left(\frac{2}{3} - \frac{2\sqrt{2}}{9} \right) \frac{r}{t}. \quad (\text{A.90})$$

Integrating from $r = r_*$ at time t_* to $r = r_r$ at time t yields

$$r_r = r_* \left(\frac{t}{t_*} \right)^{2/3 - 2\sqrt{2}/9} \quad (\text{A.91})$$

To avoid detailed numerical computations of the ejecta, Chevalier and Soker (1989) model the passage of the expanding envelope gas through the rarefaction wave as an analytic enthalpy-preserving process. Since the internal energy of the expanding envelope gas will be converted to kinetic energy by passing through the rarefaction wave, the final internal energy of the gas on the left-hand side (proportional to p_f/ρ_f) is small enough to be ignored:

$$\frac{1}{2}v_f^2 = \frac{1}{2}v_r^2 + \frac{\gamma}{\gamma - 1} \frac{p_r}{\rho_r}. \quad (\text{A.92})$$

Chevalier and Soker (1989) write the final velocity of a parcel of envelope gas after passing through the rarefaction wave for a $\gamma = 4/3$ gas:

$$v_f^2 = v_r^2 + \frac{2}{\gamma - 1} \left(\gamma \frac{p_r}{\rho_r} \right). \quad (\text{A.93})$$

The term in parentheses in Equation A.93 is the sound speed at the rarefaction wave, which by a relation analogous to Equation A.89 can be written in terms of v_r :

$$v_f^2 = v_r^2 + \frac{2}{\gamma - 1} \frac{2}{9} v_r^2 = \frac{7}{3} v_r^2. \quad (\text{A.94})$$

Making use of Equation A.77, the final velocity of a parcel of envelope gas after passing through the rarefaction wave becomes

$$v_f^2 = \frac{28}{27} \frac{r_r^2}{t^2}. \quad (\text{A.95})$$

The maximum velocity attainable by the envelope gas is related to the radius of the star r_* . The outermost envelope gas sits at $r = r_*$, and will be the gas with the highest velocity in the freely expanding ejecta. The blast wave reaches the edge of the envelope at time $t = t_*$. The maximum velocity is therefore

$$v_{\text{max}}^2 = \frac{28}{27} \frac{r_*^2}{t_*^2}. \quad (\text{A.96})$$

Chevalier and Soker (1989) write this expression in a simpler form that relates the maximum velocity of the ejecta to the total mass of the ejecta (M) and the energy of the explosion E_0 . The total mass of the ejecta is related to the radius r_* by the initial density profile $\rho_0 = Ar^{-\omega}$, where $\omega = 17/7$ in the singular case:

$$M = 4\pi \int_0^{r_*} \rho_0 r^2 dr = 4\pi \int_0^{r_*} Ar^{-17/7} r^2 dr = 7\pi Ar_*^{4/7}. \quad (\text{A.97})$$

The total energy E_0 is related to the position of the shock by Equation A.44.

The flow of material through the rarefaction wave must also conserve mass, leading to the relation

$$\frac{dm_r}{dt} = 4\pi r_r^2 \rho_r \left(v_r - \frac{dr_r}{dt} \right). \quad (\text{A.98})$$

As material passes through the rarefaction wave, it is added to the mass of the freely-expanding ejecta:

$$dm_r = -dm_f = -4\pi r_f^2 \rho_f dr_f. \quad (\text{A.99})$$

Because the ejecta is in free expansion, $v_f = r_f/t_f$, and Equation A.99 can be re-written as

$$dm_r = -4\pi v_f^2 t_f^3 dv_f. \quad (\text{A.100})$$

Substituting Equation A.91 into Equation A.96 and solving for dv_f makes it possible to change the integration variable on the right hand side of Equation A.100 to dt . The two sides of Equation A.100 are now

$$4\pi r_r^2 \rho_r \left(v_r - \frac{dr_r}{dt} \right) = -4\pi v^2 t^3 \rho \left[\frac{2}{3} \sqrt{\frac{7}{3}} \left(-\frac{1}{3} - \frac{2\sqrt{2}}{9} \right) \frac{r_*}{t_*^2} \left(\frac{t}{t_*} \right)^{-4/3-2\sqrt{2}/9} \right]. \quad (\text{A.101})$$

After significant algebraic manipulations, Chevalier and Soker (1989) arrive at the following expression for the density profile of the envelope gas after being ejected:

$$\rho = \frac{8}{7\pi\sqrt{7}(3+2\sqrt{2})} t^{-3} E^{-3/2} M^{5/2} (v/v_{\max})^{-35+24\sqrt{2}}. \quad (\text{A.102})$$

The velocity exponent simplifies to $-35 + 24\sqrt{2} \approx -1.06$. This is why 1.06 was chosen as the inner power-law exponent in the PHOENIX models of chapter 5. Most importantly, this results shows that the density distribution of the envelope gas after being ejected is a shallow power-law in velocity.

A.2.3 Final ejecta structure

The results of subsection A.2.2 and subsection A.2.1 show that a blast wave moving through a stellar envelope with a power-law density profile similar to the progenitor of SN 1987A will produce ejecta partitioned into two power-laws: the ejected envelope gas will have a shallow power-law profile of $\delta \approx -1.06$ as shown in subsection A.2.2, while the ejected atmosphere will have a steep power-law density profile, as shown in subsection A.2.1.

This relatively simple broken power-law model of Type II-P supernova ejecta has been used to investigate the early bolometric lightcurve of SN 1987A (Chevalier, 1992), interactions between pulsar winds and supernova ejecta (Chevalier and Fransson, 1992), the collision of supernova ejecta with circumstellar gas (Chevalier and Fransson, 1994; van Marle et al., 2010) and with a companion star (Kasen, 2010), and has even been used in radiative transfer modeling of the kilonova accompanying the gravitational-wave source GW170817 (Kasen et al., 2017).

The shallow inner power-law solution and the steeper outer power-law solution have the form (Chevalier and Soker, 1989; Chevalier and Fransson, 1992)

$$\rho_i = Ar^{-m}t^{m-3} \quad (\text{A.103})$$

$$\rho_o = Br^{-n}t^{n-3}. \quad (\text{A.104})$$

In order for the solution to be continuous, there exists a transition radius r_t at which the two power law solutions are equal: $\rho_i(r_t) = \rho_o(r_t)$. The location of the transition radius is found by setting the total mass equal to M and the total kinetic energy equal to E :

$$M = \int_0^{r_{max}} dm = 4\pi \left(\int_0^{r_t} \rho_i r^2 dr + \int_{r_t}^{r_{max}} \rho_o r^2 dr \right) \quad (\text{A.105})$$

$$E = \int_0^{r_{max}} de = 4\pi \left(\int_0^{r_t} \frac{1}{2} \rho_i v^2 r^2 dr + \int_{r_t}^{r_{max}} \frac{1}{2} \rho_o v^2 r^2 dr \right). \quad (\text{A.106})$$

With the assumption of homologous expansion $r(t) = vt$, the integrals become

$$M = 4\pi \left(\int_0^{v_t} Av^{2-m} dv + \int_{v_t}^{v_{max}} Bv^{2-n} dv \right) \quad (\text{A.107})$$

$$E = 2\pi \left(\int_0^{v_t} Av^{4-m} dv + \int_{v_t}^{v_{max}} Bv^{4-n} dv \right). \quad (\text{A.108})$$

To avoid a singularity at the origin, the inner density power law must be $m > 3$. The solution is simplified if the upper limit of integration can be extended to large v_{max} , in which case the integral evaluated at the upper limit vanishes for

$n > 5$ and the solution takes the form

$$M = 4\pi \left(\frac{Av_t^{3-m}}{3-m} - \frac{Bv_t^{3-n}}{3-n} \right) \quad (\text{A.109})$$

$$E = 2\pi \left(\frac{Av_t^{5-m}}{5-m} - \frac{Bv_t^{5-n}}{5-n} \right). \quad (\text{A.110})$$

The constants A , B and the transition velocity v_t can be written in terms of the parameters E , M , m , and n after requiring that the density be continuous across the transition velocity:

$$B = Av_t^{n-m}. \quad (\text{A.111})$$

This leads to the transition velocity

$$v_t = \left[\frac{2(5-m)(5-n)}{(3-m)(3-n)} \frac{E}{M} \right]^{1/2} \quad (\text{A.112})$$

and the density profile constant

$$A = \frac{1}{4\pi} \frac{(n-3)(3-m)}{n-m} \frac{M}{v_t^{3-m}} \quad (\text{A.113})$$